Propagation of Engineered Beams through Photorefractive Materials

A Thesis

submitted for the Award of Ph.D. degree of

MOHANLAL SUKHADIA UNIVERSITY

in the

Faculty of Science

By

Vaity Pravin Prabhakar

Under the Supervision of

Dr. R. P. Singh

Scientist-SF
Theoretical Physics Division
Physical Research Laboratory, Ahmedabad, India.

DEPARTMENT OF PHYSICS
FACULTY OF SCIENCE
MOHANLAL SUKHADIA UNIVERSITY
UDAIPUR (RAJ)

Year of submission: 2012

To

my parents & grandparents

DECLARATION

I, **Mr. Vaity Pravin Prabhakar**, S/o Mr. Vaity Prabhakar Nathuram, resident of F-205, PRL residences, Navrangpura, Ahmedabad 380009, hereby declare that the research work incorporated in the present thesis entitled, **"Propagation of Engineered Beams through Photorefractive Materials"** is my own work and is original. This work (in part or in full) has not been submitted to any University for the award of a Degree or a Diploma. I have properly acknowledged the material collected from secondary sources wherever required. I solely own the responsibility for the originality of the entire content.

Date:

Vaity Pravin Prabhakar

Signature of the candidate

CERTIFICATE

I feel great pleasure in certifying that the thesis entitled, **"Propagation of Engineered Beams through Photorefractive Materials"** by Mr. Vaity Pravin Prabhakar is under my guidance. He has completed the following requirements as per Ph.D regulations of the University.

(a) Course work as per the university rules.

(b) Residential requirements of the university

(c) Regularly submitted six monthly progress reports

(d) Presented his work in the departmental committee

(e) Published/accepted minimum of one research paper in a referred research journal,

I recommend the submission of thesis.

Date:

Dr. R. P. Singh
(Thesis Supervisor)
Scientist-SF, THEPH,
Physical Research Laboratory,
Ahmedabad - 380 009.

Countersigned by

Head of the Department

Acknowledgements

It is too difficult to spend five years away from parents, relatives, and friends for a person like me. After two days of joining in PRL, I started feeling home-sick. But, thanks to my lab environment, it made my life cool and accelerated my scientific career with the full speed. I would like to express my gratitude to my supervisor Dr. R. P. Singh for creating such an environment. Because of his friendly nature and calm behavior, I have been able to put my views and ideas freely in front of him. He has provided full freedom to implement my ideas in the lab. I have gained not only scientific knowledge but also moral values while working with him.

I would like to acknowledge Prof. J. N. Goswami, the Director, Prof. Anjan Joshipura, the Dean, Prof. Utpal Sarkar and Prof. A. K. Singhvi, former Deans, Dr. Bhushit Vaishnav, Head, Academic Services, Dr. P. Sharma, former Head, Academic Services and Mr. Y. M. Trivedi, the Registrar, Physical Research Laboratory for providing me the necessary facilities to carry out my thesis work. I am grateful to the chairman and members of the academic committee for their criticism and comments during the reviews.

I sincerely thank to Prof. N. M. Ashok, Prof. R. Sekar, Prof. S. Mohanty, Prof. Panigrahi, Dr. R. Rangarajan, Dr. Angom, Dr. K. K. Marhas, Dr. K. P. Subramanian for teaching useful courses during the course work. My special thanks to Dr. K. P. Subramanian and Dr. Bhas Bapat for conducting case study during the course work and for the SERC school. The discussion with Prof. J. Banerji was quite useful. His critical comments were a great help to me in improving my experimental results. I would like to express my gratitude to area chairman and faculties of theoretical physics division for their cooperation and encouragement.

I am grateful to my lab mates both past and present which include V. K. Jaiswal, Ashok, Jitendra, Sunita, Shashi, Gangi, Aadhi and Chithra. The discussion with them helped me immensely in my work. My special thanks to Dr. Goutam Samanta for keeping sportsman alive in me and other students. His knowledge of technical intricacies involved in the experiments is also appre-

ciable. It is great to have a labmate like Ashok who have provided all kinds of help. It is a pleasure to work with him. I have shared ups and downs in the experiments with him. Our academic and non-academic discussion, jokes and mimicry made my stay enjoyable in the lab. I am also thankful to Aadhi for his help in lab during my experiments especially for providing apertures to me. I have learned a lot from Aadhi's doubts and confusions. Special thanks to Adahi and Chithra for carefully reading my thesis. I would like to thank visitors to the lab which include summer and engineer trainees, particularly to Yedhu Krishna, Vishal, Kinchit and Binal.

I must acknowledge all staff members of library, computer center, workshop, glass blowing, dispensary, canteen and administration for rendering their help and cooperation at all stages. Special thanks to Uma madam for her help in library related matters. I am also grateful to Tejas for taking course on C and C++ programming.

I would like to express my gratitude to my PRL friends Morthekai, Ritesh bhai, Rohit, Subimalda, Shreyash, Santosh, Sanatda, Umaji, Alok, Bhavik bhai (rocking), Gyana, Kirpa Ram, Mani sahab, Naveen (gandhi), Rahman, Sumanto, Vishal bhai, Amzad, Anand, Arvind, Bhaswar (chat), Naveen, Pankaj, Rabiul, Rohit, Sandeep, Soumya, Sreekanth, Suman, Vimal (captain boss), Vineet, Vivek, Arun, Amrendra, Chinmay, Koushik, Sidharth, Sunil, Yogita, Fazlul, Avdhesh (gul gul), Damu, Gulab, Gaurav (both), Girish, Nigam, Guru, Manu, Sanjay, Anjishnu, Jayant, Joydeep, Linto, Sharmaji, and Shinde.

I am grateful to my batch mates Ashish, Arvind, Iman, Jayati, Ketan, Moumita, Nishant, Neeraj (motu), Prashant, Sanat, Satinder, Subrata, Sudhanva, Suruchi, Srinivas and Tapas. I am glad to thank Jayati (mummy), Srinivas (gunddu), and Tapas for tolerating my childish behavior. My special thanks to Bhaswar, Ketan, and Moumita for their presence during Ph.D. registration in MLSU and helping me for all along in completing official formalities at MLSU. The very special thanks to Ketan for making format of semester and annual reports. I would like to appreciate my hostel's friends, mainly Bhaswar, Lokesh and Srinivas for tolerating my blaring of songs every morning.

I would like to express my huge thanks to my friends from Mumbai which include my MSc batchmates and colony friends, mainly to Manish, Mahesh, Prabi, Shashi, Vijay and Vikrant those who came for the treks and trips with me. Our treks and tours have left a mark in the form of good memory in my mind. These guys have made my stay pleasant in Mumbai. Their love and support are really helpful to me. I also like to thank Jyotsna and Varun for their support during my initial PhD days. I would like to expand my thanks to my friends from Ahmedabad, outside the PRL, Jasraj, Jitu bhai, Nihar, and Vishwas for their company.

There are no words to express the love and support I got from my parents and relatives. Their love, blessing and faith help me to survive during the critical time in Ahmedabad. The telephonic conversations with them, mainly with my cousins have remained a great source of joy. Our get together in "Holi", "Gokul Astami", and "Ganesh Chaturthi" brought a happiness in my life. I am grateful to my cousin Bharati tai and her family to encourage me for education since my childhood.

Pravin

ABSTRACT

The photorefractive (PR) materials, which show nonlinear response to an incident light, have already proved their importance in various applications. These applications include two wave mixing, four wave mixing, phase conjugation and optical data storage. The advantage of these materials is that they show nonlinearity at very low laser powers (μW) unlike Kerr materials which require very high power. In this thesis, we have found experimentally and numerically, new solutions for the nonlinear paraxial wave equation (PWE) with the PR nonlinearity for beams engineered in our laboratory using computer-generated holography. These beams include dipole & quadrupole vortices, Hermite-Gaussian (HG) beams, Laguerre-Gaussian (LG) beams, Bessel beams, Airy beams and superposed LG beams. We have studied their dynamics in free space to make a comparison with the nonlinear dynamics. It also helps us to characterize these beams.

In this thesis work, we have studied both linear and nonlinear dynamics of dipole and quadrupole vortices. The linear dynamics of these beams is found to be unstable which is verified with exact analytical expression. However, in presence of nonlinearity they form stable structures while propagating through a photovoltaic PR medium.

We have formed dark ring beams using LG modes and studied their propagation through PR medium. It is found that the dark ring beam breaks to form quadrupole vortex in the presence of defocusing nonlinearity, instead of forming dark ring soliton. These results suggest that dipole and quadrupole vortices may be the solutions of nonlinear PWE with the PR nonlinearity.

We have studied propagation dynamics of non-diffracting, self-accelerated Airy beams through the PR medium with self-focusing nonlinearity. We observe interaction amongst their lobes as they propagate in the PR medium. The result shows that self-trapped, self-accelerated beam can not exist in the PR medium. We have also examined propagation dynamics of HG beams, superposed LG beams and Bessel beams in the PR medium.

Keywords: photorefractive, nonlinear, singular optics; computer holography

LIST OF PUBLICATIONS

A. Publications in Journals

1. Ashok Kumar, Pravin Vaity, Yedhu Krishna, and R. P. Singh, *Engineering the size of dark core of an optical vortex*, Opt. Laser Eng. 48, 276-281 (2010).

2. Ashok Kumar, Pravin Vaity, and R. P. Singh, *Diffraction characteristics of an optical vortex passing through an aperture-iris diaphragm*, Opt. Commun. 28, 4141-4145, (2010).

3. Ashok Kumar, Pravin Vaity, and R. P. Singh, *Crafting the core asymmetry to lift the degeneracy of optical vortices*, Opt. Express 19, 6182-6190, (2011).

4. Ashok Kumar, Shashi Prabhakar, Pravin Vaity and R. P. Singh, *Information content of optical vortex field*, Opt. Lett. 36, 7-9, (2011).

5. Pravin Vaity and R. P. Singh, *Self-healing property of optical ring lattice*, Opt. Lett. 36, 2994-2996 (2011).

6. Ashok Kumar, Pravin Vaity, J. Banerji, and R. P. Singh, *Making copies of optical vortices*, Phys. Lett. A 375, 3634-3640 (2011).

7. Pravin Vaity and R. P. Singh, *Topological charge dependent propagation of optical vortices under quadratic phase transformation*, Opt. Lett. 37 1301-1303 (2012).

8. Pravin Vaity and R. P. Singh, *Generation of quadrupoles through instability of dark rings in photorefractive media*, J. Opt. Soc. Am. B (to be published).

9. Pravin Vaity and R. P. Singh, *Measuring orbital angular momentum of light using simple convex lens*, Submitted to Opt. Lett.

10. Pravin Vaity and R. P. Singh, *Structurally stable dipole and quadrupole vortex in photorefractive media*, Submitted to Phys. Rev. A.

B. Full Length Conference Papers

1. Pravin Vaity, Ashok Kumar, and R. P. Singh, *Experimental study of power decay of optical vortices in photorefractive material* National Laser Symposium-09, 75, Jan 13-16, 2010 at BARC Mumbai, India.

2. Ashok Kumar, Pravin Vaity, and R. P. Singh, *Decay of high order elliptical optical vortices* National Laser Symposium-19, 3153, Dec 1-4, 2010 at RRCAT Indore, India.

3. Pravin Vaity, Ashok Kumar, Shashi Prabhakar, and R. P. Singh, *2-D Airy beam propagation through photorefractive materials* Photonics-2010, Proc. SPIE 8173, 81730N-81730N-6, (2010).

4. Ashok Kumar, Shashi Prabhakar, Pravin Vaity, and R. P. Singh, *Two point correlation function for optical vortices* Photonics-2010, 556, Dec 12-15, 2010, at IIT Guwahati, India.

5. Ashok Kumar, Pravin Vaity, and R. P. Singh, *Degeneracy of optical vortices and the core asymmetry* XXXV OSI Symposium- International Conference on Contemporary Trends in Optics and Optoelectronics, 342, Jan 17-19, 2011 at IIST Thiruvananthapuram, India.

6. R. P. Singh, Ashok Kumar, Pravin Vaity, and Shashi Prabhakar, *Dynamic light scattering of optical vortices* XXXV OSI Symposium- International Conference on Contemporary Trends in Optics and Optoelectronics, 37, Jan 17-19, 2011 at IIST Thiruvananthapuram, India.

7. R. P. Singh, Pravin Vaity, Ashok Kumar, S. G. Reddy, and A. Aadhi *Dynamics of Fractional Charge Optical Vortices,* International Conference on Trends in Optics and Photonics (IConTOP), 217, Dec 7-9, 2011 at SINP, Kolkata, India.

8. Pravin Vaity and R. P. Singh *Measurement of Topological Charge of Optical Vortex Using Airy Function,* International Conference on Trends in Optics and Photonics (IConTOP), 221, Dec 7-9, 2011 at SINP, Kolkata, India.

Contents

List of Figures

Chapter 1

Introduction

The laser cavity with rectangular symmetry supports the Hermite-Gaussian (HG) modes whereas Laguerre-Gaussian (LG) modes are formed in the cylindrically symmetric cavity. The commercially available lasers have typically a Gaussian beam profile. The Gaussian beam is a fundamental mode of any laser cavity, it is also called as TEM_{00} mode. For higher order modes, special cavity design is needed [1–3].

In this thesis, we have generated different kinds of beams by engineering phase of an input laser beam, therefore, we call these beams as the engineered beams. We convert a Gaussian laser beam into these beams by imprinting corresponding phase through a spatial light modulator (SLM). Apart from HG and LG beams, there are other beams like Airy beams [4] and Bessel beams [5] which can be produced using this technique.

The above mentioned beams are the solutions of paraxial wave equation (PWE) [6]. The propagation dynamics of these beams are well studied in a linear regime through the PWE. In linear regime, the refractive index of medium is unaffected by an incident light field. However, there are some materials which respond to the incident light field nonlinearly. When a light beam propagates through such a material, it modifies the index of refraction, which affects propagation of the same beam. This complex dynamics can be calculated with nonlinear PWE. In this thesis, we have studied the propagation of various engineered beams through linear and nonlinear media. We have used photorefractive (PR) material [7] as our nonlinear system. In this work our aim is to find out new solutions for nonlinear PWE with the PR nonlinearity.

The PR materials have already proved their importance in various nonlinear phenomena which include two wave mixing, four wave mixing, and phase conjugation [7]. The research on formation of spatial solitons and the light induced photonic lattice in the PR media are demanding a great deal of attention [8–13]. These effects follow the changes in refractive index in the PR medium that can be controlled by an applied field, and the ratio of input intensity of beam to background light. Unlike other nonlinear materials, in the PR materials a strong nonlinearity is observed at milliwatts of laser power itself.

We start this chapter with Maxwell's equations which are the fundamental equations of Electromagnetic theory. We show how wave equation can be obtained from Maxwell's equations in Section 2. In Section 3, the nonlinear PWE for inhomogeneous media is derived from the wave equation. Different nonlinearities are discussed in Section 4. Section 5 is devoted to the solutions of PWE for free space or homogeneous media. The aim of the thesis is summarized in section 6. And finally, Section 7 gives an overview on chapters of the thesis.

1.1 Maxwell's Equations

In Nineteenth century, Maxwell unified electricity, magnetism and light into one theory. The theory contains four equations, now called as Maxwell's equations [6, 7, 15]. These equations couple the electric field vector E and the magnetic field vector H in following way,

$$\begin{aligned} \nabla \times E + \frac{\partial(\mu H)}{\partial t} &= 0, \\ \nabla \times H - \frac{\partial(\epsilon E)}{\partial t} &= J, \\ \nabla \cdot (\epsilon E) &= \rho, \\ \nabla \cdot (\mu H) &= 0, \end{aligned} \tag{1.1}$$

where J is the current density and ρ is the charge density. μ and ϵ are the magnetic permeability and the electric permittivity or dielectric constant of medium, which are related to the magnetic susceptibility χ_m and the electric susceptibility χ_e of medium, respectively. Their relations are written as follows.

$$\epsilon = \epsilon_0(1+\chi_e); \quad \mu = \mu_0(1+\chi_m), \tag{1.2}$$

where μ_0 and ϵ_0 are the permeability and the permittivity of vacuum. The index of refraction of media relates to these two constants through following relation.

$$n = \sqrt{\frac{\epsilon\mu}{\epsilon_0\mu_0}}. \tag{1.3}$$

Note that for an anisotropic medium ϵ become a tensor of rank 2. Most of the PR media are anisotropic in nature (e.g. lithium niobate, strontium barium niobate, barium titanate). More details on anisotropic nature of the PR media are discussed in Chapter 3.

1.2 Wave Equation

Consider a pure dielectric inhomogeneous media ($\mu = \mu_0$ and $\epsilon = \epsilon(x, y, z)$). For such a medium Maxwell's equations take the form,

$$\begin{aligned} \nabla \times E + \mu_0 \frac{\partial H}{\partial t} &= 0, \\ \nabla \times H - \epsilon \frac{\partial E}{\partial t} &= 0, \\ \nabla \cdot \epsilon E &= 0, \\ \nabla \cdot H &= 0. \end{aligned} \tag{1.4}$$

These equations can be decoupled separately into following two equations for E and H as

$$\begin{aligned} \nabla^2 E - \mu_0\epsilon \frac{\partial^2 E}{\partial t^2} &= \nabla(E \cdot \frac{\nabla\epsilon}{\epsilon}), \\ \nabla^2 H - \mu_0\epsilon \frac{\partial^2 H}{\partial t^2} &= \nabla \times H \times \frac{\nabla\epsilon}{\epsilon}. \end{aligned} \tag{1.5}$$

If change in refractive index is small over the distance of one wavelength, then the quantity $\frac{\nabla\epsilon}{\epsilon}$ can be negligible. And the Eqs. (1.5) become,

$$\nabla^2 E - \mu_0\epsilon\frac{\partial^2 E}{\partial t^2} = 0,$$
$$\nabla^2 H - \mu_0\epsilon\frac{\partial^2 H}{\partial t^2} = 0. \tag{1.6}$$

In general form, above equations are written as,

$$\nabla^2 u - \mu_0\epsilon\frac{\partial^2 u}{\partial t^2} = 0, \tag{1.7}$$

where u can be any component of the electric field vector E or the magnetic field vector H. The above equation is called as a wave equation which governs propagation of electromagnetic waves in inhomogeneous media.

1.3 Paraxial Wave Equation

We often consider light in the form of beam (e.g. laser beam) which is monochromatic and highly directional. One can write this beam as the superposition of plane waves,

$$u(x, y, z, t) = A(x, y, z)\exp[i(kz - \omega_0 t)], \tag{1.8}$$

where $A(x, y, z)$ is the complex field amplitude, ω_0 is the frequency of light and k is the wave number in medium. After substituting Eq. (1.8), the wave equation becomes,

$$\nabla_t^2 A + \frac{\partial^2 A}{\partial z^2} + 2ik\frac{\partial A}{\partial z} - (k^2 - \mu_0\epsilon\omega_0)A = 0, \tag{1.9}$$

where,

$$\nabla_t^2 = \frac{\partial^2}{\partial x^2} + \frac{\partial^2}{\partial y^2}, \tag{1.10}$$

Physically, the change in A within a wavelength along the z direction is smaller than the A itself. The slow dependence of A can be represented by the paraxial approximation which is mathematically written as,

$$\frac{\partial A}{\partial z} \ll kA \Rightarrow \frac{\partial^2 A}{\partial z^2} \ll k\frac{\partial A}{\partial z}. \tag{1.11}$$

With this paraxial approximation, Eq. (1.10) becomes

$$\nabla_t^2 A + 2ik\frac{\partial A}{\partial z} - (k^2 - \mu_0\epsilon\omega_0)A = 0. \tag{1.12}$$

The refractive index of inhomogeneous media can be written as,

$$n(x, y, z) = \sqrt{\frac{\epsilon(x, y, z)}{\epsilon_0}}. \tag{1.13}$$

Also,

$$\begin{aligned} &n(x, y, z) = n_0 + \Delta n(x, y, z), \\ &n^2 = (n_0 + \Delta n)^2 = n_0^2 + 2n_0\Delta n + \Delta n^2, \\ &n^2 \approx n_0^2 + 2n_0\Delta n. \end{aligned} \tag{1.14}$$

In above equations, n_0 is the linear refractive index while Δn is the change in index of refraction. Now, consider the last term of Eq. (1.12) and substituting value of ϵ in it.

$$k^2 - \mu_0\epsilon\omega_0 = k_0^2 n_0^2 - \mu_0\epsilon_0 n^2\omega_0 = k_0^2(n_0^2 - n^2), \tag{1.15}$$

where, k_0 is the wave number in free space. Substituting from Eq. (1.14) in Eq. (1.15), we get

$$k^2 - \mu_0\epsilon\omega_0 = -\frac{2k\Delta n}{n_0}. \tag{1.16}$$

After substituting above equation in Eq. (1.12) and rearranging the terms, we obtain

$$\frac{\partial A}{\partial z} = \frac{i}{2k}\nabla_t^2 A + \frac{ik\Delta n}{n_0}A. \tag{1.17}$$

The above equation is PWE which can calculate the propagation of any beam having complex field amplitude $A(x, y)$ throughout the inhomogeneous media, therefore, this equation is also called as paraxial beam propagation equation. In general, this equation is difficult to solve analytically due to complex form of Δn, however, one can solve it numerically. Finite Difference, Finite Element and Split-Step Fourier Transform are different numerical beam propagation methods which can be used to solve this equation [14–16]. We have used Split-Step Fourier Transform method to solve this equation. The details of this method are discussed in Appendix A.

There are some nonlinear processes which modify the index of refraction and make the medium inhomogeneous. These nonlinearities exist according to their dependence on intensity (Kerr nonlinearity, saturable nonlinearity), space charge field (PR nonlinearity), temperature (thermal nonlinearity) and molecular orientation (reorientation nonlinearity) [17]. We will discuss these in the next section.

1.4 Nonlinear Process

The process is called nonlinear, when the response of a material system to an applied light field depends nonlinearly upon the strength of the light field [17]. There are different media which show different nonlinear response that may be local or nonlocal. When change in index of refraction at a particular point relies on the intensity or the field value at the same point, then the response is local otherwise it is nonlocal. Kerr nonlinearity has local response whereas thermal, photorefractive and reorientation nonlinearities have nonlocal response.

1.4.1 Kerr Nonlinearity

In Kerr nonlinearity, the change in index of refraction Δn is proportional to the light intensity I. Mathematically, it is written as,

$$\Delta n = n_2 I. \tag{1.18}$$

Here, n_2 is the nonlinear coefficient or the Kerr coefficient. After substituting value of Δn in Eq. (1.17), the equation becomes well known nonlinear Schrödinger equation. This equation satisfies soliton solution. At present, the Kerr nonlinearity is used for generation of spatial solitons [14,15,18]. It is also used for self-phase modulation [19] and Kerr-lens modelocking [20].

1.4.2 Thermal Nonlinearity

Some part of light energy is absorbed by a material, when the laser beam incidents on the material. This changes temperature of the material. The change in temperature leads to the change in index of refraction, written as

$$\Delta n = \frac{dn}{dT} T_1, \tag{1.19}$$

where dn/dT is the constant which represents temperature dependence of the index of refraction. For fused silica, its value is 1.2 x 10^{-5}. T_1 is the laser induced change in temperature. One can measure T_1 for a given input intensity profile $I(x, y)$ through following heat transport equation under steady state,

$$-\kappa \nabla^2 T_1 = \alpha I(x, y), \tag{1.20}$$

where κ and α are the thermal conductivity and the linear absorption coefficient of material. The spatial solitons and their interaction can be studied by employing thermal nonlinearity in a lead glass [21]. The same nonlinearity has been used as the basis for the construction of temperature and chemical sensors.

1.4.3 Photorefractive Nonlinearity

When photorefractive material is illuminated by a light beam, free charge carriers are generated at the rate proportional to the input optical power [7,17]. These charges diffuse away from the high intensity region, leaving behind the fixed charges of opposite sign. The free charge carriers are trapped by ionized impurities at other locations where intensity is low or zero, depositing their charge as they recombine. The result is the formation of space charge field E_{sc} which modulates local refractive index via electro-optic effect or Pockel's effect.

The change in index of refraction is given by

$$\Delta n = -\frac{1}{2} n_0^3 r_{eff} E_{sc}, \tag{1.21}$$

where r_{eff} is the effective electro-optic coefficient or Pockels coefficient of medium. This nonlinearity have been employed for many interesting effects which include generation of spatial solitons, both coherent and incoherent [18, 22], beam coupling, phase conjugation and dynamic holography [7]. The spatial soliton is one of the solutions of nonlinear PWE with PR nonlinearity. We have used PR nonlinearity for our study of nonlinear propagation of engineered beams. We will discuss this nonlinearity in more detail in Chapter 3.

1.5 Solutions of nonlinear PWE with PR nonlinearity

Self-focusing and self-defocusing of an input beam in a nonlinear medium is decided by the sign of Δn. These effects balance the diffraction to form bright and dark spatial solitons respectively [18]. These solitons can be the solutions of nonlinear PWE with PR nonlinearity. The advantage of the PR nonlinearity is its ability to exhibit either self-focusing or self-defocusing in the same crystal by a reversal of external field. Therefore, same crystal can be used for generation of both bright and dark solitons [18, 22].

When light beam propagates through a PR medium, the space charge field is formed due to redistribution of charges. This field can be screened out by an externally applied DC field or a photovoltaic field. The effective field can modify the index of refraction to form a spatial soliton. Mainly two types of spatial solitons can exist in a PR medium- screening solitons [23] and photovoltaic solitons [24–26]. The screening solitons are formed by the external DC field while photovoltaic solitons are generated by the photovoltaic field. These solitons have application in optical communication [27–29].

1.5.1 Bright Spatial Solitons

The light beams have intrinsic property of diffraction while propagating through a homogeneous medium. If this diffraction is exactly compensated by change in the index of refraction of the medium due to nonlinear effect, then a shape preserving beam is formed, which is called as bright spatial soliton.

Figure 1.1 shows the formation of bright spatial soliton in a cerium doped strontium barium niobate (SBN) crystal. In the absence of nonlinearity, the beam is diffracted naturally. When this natural diffraction is exactly compensated by the self-focusing PR nonlinearity, bright spatial soliton is formed as shown in Fig. 1.1. Due to the anisotropy of the PR crystal, the soliton has an elliptical shape. It should be noted that the soliton solution exist for particular values of three parameters, 1) ratio of peak input intensity to background illumination, 2) applied electric field and 3) input beam radius.

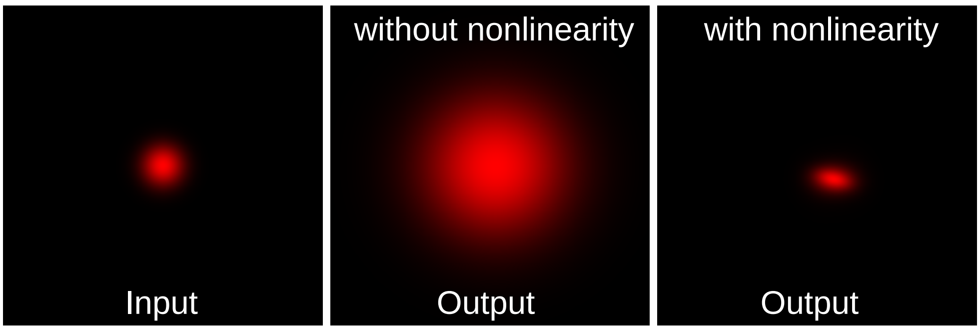

Figure 1.1: Formation of bright spatial soliton.

1.5.2 Dark Spatial Solitons

The dark soliton is a shape preserving hole or stripe in a uniform background of light. When diffraction of hole or stripe is exactly canceled by the defocusing effect, then only dark soliton is formed. The stripe forms one dimensional (1D) soliton whereas hole gets self-trapped and generates two dimensional (2D) dark soliton. If the self-trapped hole is associated with a phase singularity, then it is called a vortex dark soliton or simply a vortex soliton [24, 30, 31].

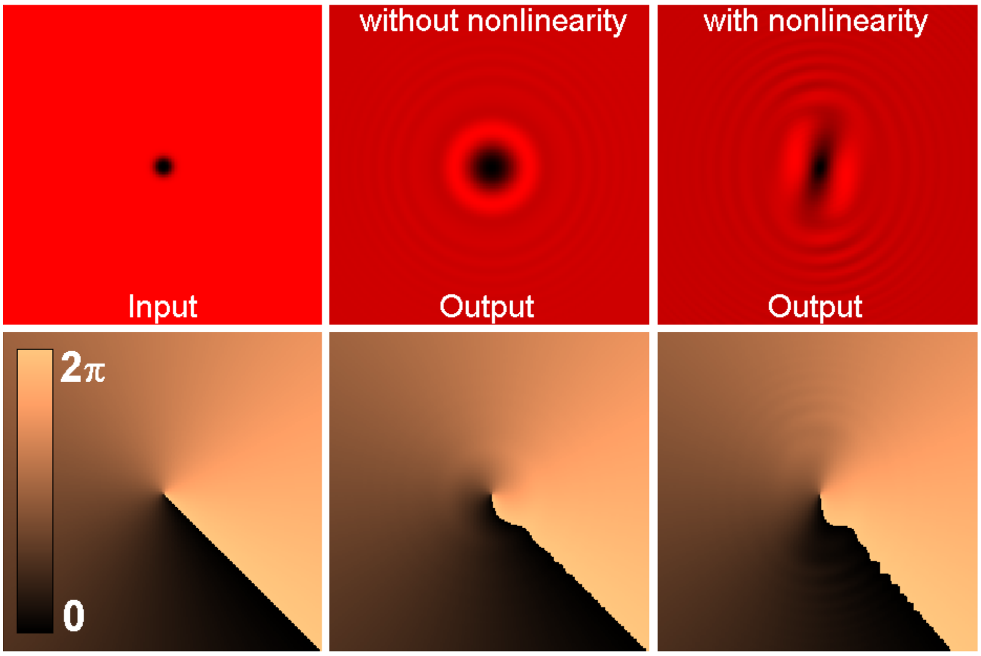

Figure 1.2: Formation of dark vortex spatial soliton (first row) along with phase profiles (second row).

Figure 1.2 illustrates the formation of vortex soliton in an iron doped lithium niobate. The core of vortex is diffracted in the absence of nonlinearity. As the diffraction is balanced by the defocusing nonlinearity of the PR medium, the dark soliton is formed as shown in Fig. 1.2. Again due to the anisotropy of the crystal, the shape of the dark hole is elliptical.

1.6 Solutions of Linear Paraxial Equation

When $\Delta n = 0$, Eq. (1.17) reduces to

$$\frac{\partial A}{\partial z} = \frac{i}{2k} \nabla_t^2 A. \tag{1.22}$$

This is PWE for homogeneous media. The above equation looks like a quantum mechanical Schrödinger equation with zero potential. The Gaussian beam is the most interesting and useful solution of the PWE. Apart from that HG beams, LG beams, Bessel beams and Airy Beams also satisfy above equation.

1.6.1 Gaussian Beam

The fundamental mode also termed as TEM_{00} mode for any laser cavity can be approximated by a Gaussian function. Therefore, this mode is called as a Gaussian beam. Most of the commercial lasers are available with Gaussian beam as the output. The power of Gaussian beam is concentrated in the center and it decreases exponentially as one moves away from the center. The wavefront of this beam is plane at $z = 0$ or at the waist and becomes spherical as the beam propagates. The complex field amplitude of a Gaussian beam is written as,

$$A(x, y, z) \quad = A_0 \exp[-\frac{x^2+y^2}{w^2}]\exp[ikz + \frac{ik(x^2+y^2)}{2R}]\exp[-i\psi], \tag{1.23}$$

where k is the wave number and A_0 is the amplitude of beam at $x, y, z = 0$. w is the beam radius at z, R is the radius of curvature and ψ is the Guoy phase shift of the Gaussian envelope. w, R, and ψ are the beam parameters which

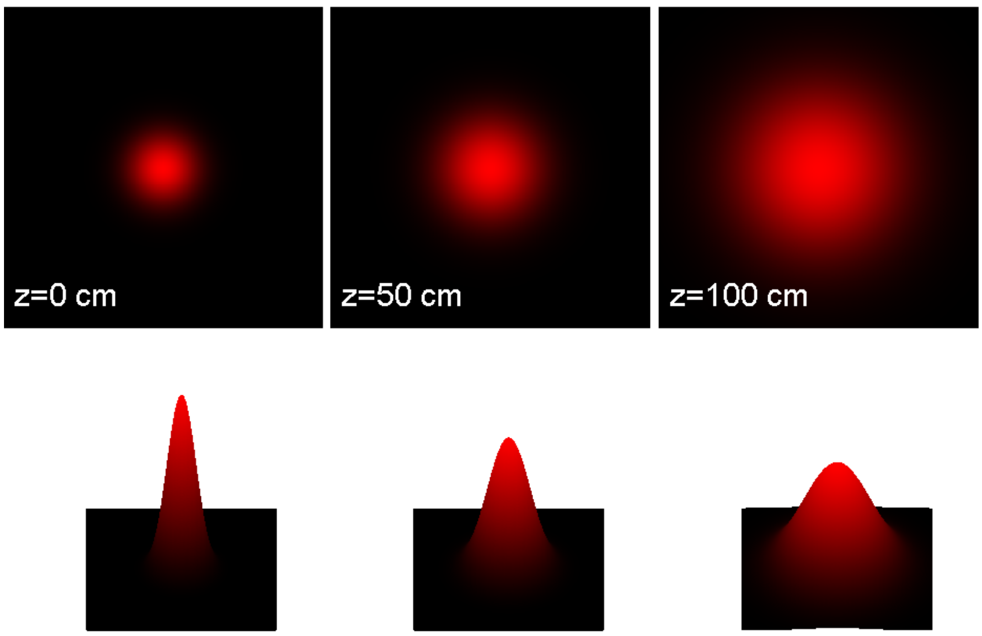

Figure 1.3: Intensity distribution of Gaussian beam at different propagation distances z.

are related to the waist spot size w_0 and the Rayleigh range $z_r = kw_0^2/2$,

$$w = w_0\sqrt{1+(\frac{z}{z_r})^2}, R = z + \frac{z_r^2}{z}, \psi = \arctan(\frac{z}{z_r}). \tag{1.24}$$

At the plane $z = z_r$, beam have following properties.

1) The beam radius increases by $\sqrt{2}$ and beam cross section by 2.

2) The intensity at beam axis becomes half from its value at $z = 0$.

3) The Guoy phase shift becomes $\pi/4$.

4) The radius of curvature has smallest value ($R = 2z_r$).

The intensity distribution of Gaussian beam at different propagation distances are shown in Fig. 1.3. The peak intensity of the beam decreases with propagation distance z. Figure 1.3 also indicates that the beam radius increases gradually with distance z.

1.6.2 Vortex Beam

Optical vortices, often encountered in nature by scattering of light through the rough surfaces, are the phase singularities in optical field [32, 33]. In contrast to the well known wavefronts like plane and spherical, the optical vortex has a helical wavefront. The helical wavefront causes an orbital angular momentum (OAM) of $l\hbar$ per photon in such beams (l being order or topological charge of the vortex) [33]. The vortex beams have found a variety of applications in the fields of optical tweezing and optical spanning [34], optical communication [35], as well as in quantum information [36].

The complex field distribution of an optical vortex of charge l embedded in a Gaussian beam can be written as [37]

$$\begin{aligned} A(x,y,z) &= (x + \mathrm{sgn}\, iy)^l \frac{w_0}{w^{l+1}} \exp[-\frac{(x^2+y^2)}{w^2}] \\ &\quad \exp[ik\frac{(x^2+y^2)}{2R}]\exp[ikz - i(l+1)\psi], \end{aligned} \tag{1.25}$$

sgn denotes the sign of topological charge which is +1 for positive and -1 for negative. The intensity profiles, interference of vortex with a plane wave and phase profiles for different values of l are shown in Fig. 1.4. The fork pattern

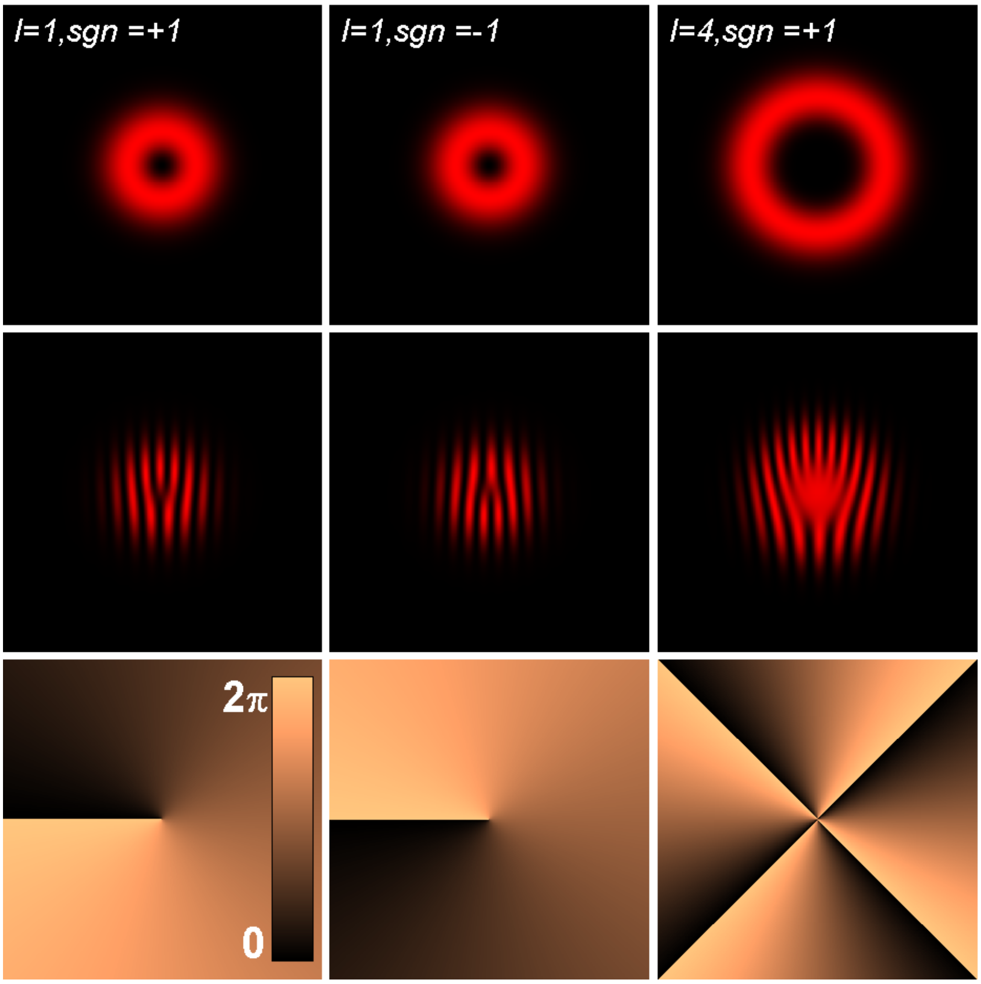

Figure 1.4: Intensity profiles (first row), interferogram (second row), and phase profiles (third row) for vortex of order l.

in interferograms shows the presence of vortex or singularity. The direction of fork also provides the sign of topological charge. The phase variation is from 0 to $2\pi l$ for the vortices of order l around the singularity as shown in Fig. 1.4.

1.6.3 Hermite-Gaussian Beams

The HG beams are the eigen modes of stable laser resonator with rectangular symmetry. These solutions are complete and form orthogonal set. The complex field distribution of HG beams for homogeneous media is given by [33, 38],

$$\begin{aligned} A_{mn}(x,y,z) &= \frac{1}{w}\sqrt{\frac{2}{\pi m!n!}}\exp[-\frac{x^2+y^2}{w^2}]H_m(\frac{\sqrt{2}x}{w})H_n(\frac{\sqrt{2}y}{w}) \\ & \exp[ikz+\frac{ik(x^2+y^2)}{2R}]\exp[-i(n+m+1)\psi], \end{aligned} \tag{1.26}$$

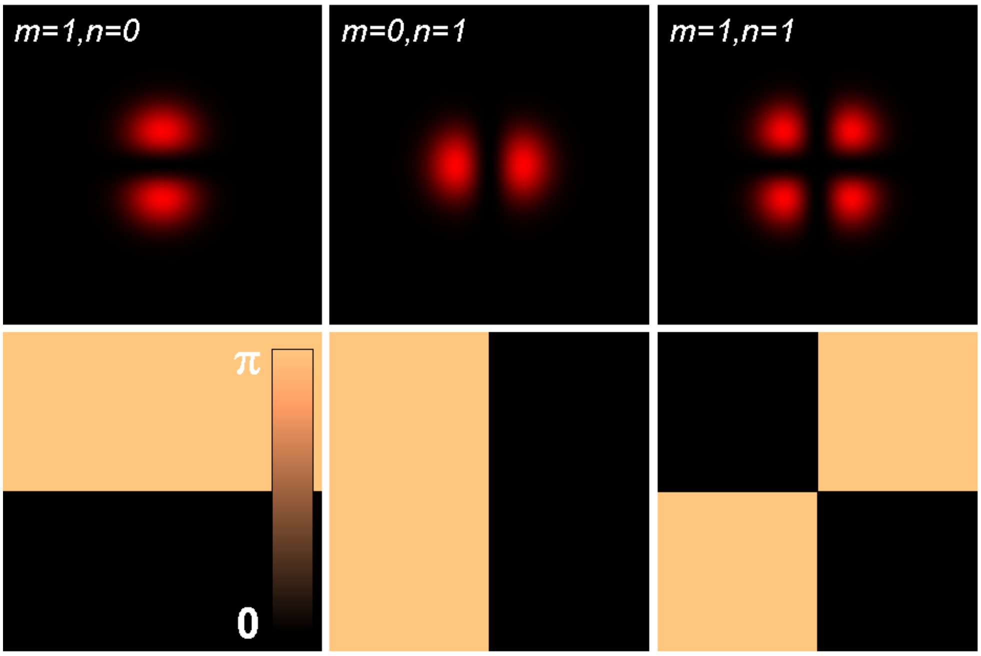

Figure 1.5: Intensity profile (first row) of HG beam for different value of indices along with phase profile (second row).

where m and n are the indices which represents the order of Hermite polynomial H. The intensity profiles and the phase profiles for different m and n indices are shown in Fig. 1.5. The phase profiles show that there is a sharp phase jump of π between two intensity lobes. This forms edge dislocations in HG Beams.

For $m = 0$ and $n = 0$, we will get same expression as a Gaussian beam. The HG modes can be converted into LG modes by using cylindrical lens mode converter and vice versa [33, 38].

1.6.4 Laguerre-Gaussian Beams

The LG beams are the eigen modes of stable laser resonator with cylindrical symmetry. Like HG modes, they also form complete and orthogonal set of solution. If the Laplacian in Eq. (1.22) is defined in the cylindrical coordinate system, then we get paraxial equation in cylindrical coordinate. The LG beams are solution of this equation. The complex field distribution of LG beams are written as [33, 38],

$$A_p^l(r,\phi,z) = \frac{1}{w}\sqrt{\frac{2p!}{\pi(p+|l|)!}}(\frac{r\sqrt{2}}{w})^{|l|}\exp[-\frac{r^2}{w^2}]L_p^l(\frac{2r^2}{w^2})$$
$$\exp[ikz+\frac{ikr^2}{2R}]\exp[il\phi]\exp[-i(2p+l+1)\psi], \quad (1.27)$$

where p and l are the radial and the azimuthal indices which represent orders of associated Laguerre polynomial L_p^l. The intensity profiles and the phase profiles for different indices p and l are shown in Fig. 1.6. These beams contain p dark rings in their intensity profile with a π phase jump. Due to azimuthal phase term $\exp(il\phi)$, they have a twist of $2\pi l$ in their wavefront which acts as a screw dislocation. This generates phase singularity in the wavefront which leads to darkness in intensity. Due to the same twist, these beams carry an OAM of $l\hbar$ per photon [33]. This OAM can be transfered to micron size particle placed along the propagation axis. This property of Laguerre-Gaussian beams have practical interest in the field of optical trapping and micromachining. It is noted that the OAM of LG beams are different from the angular momentum

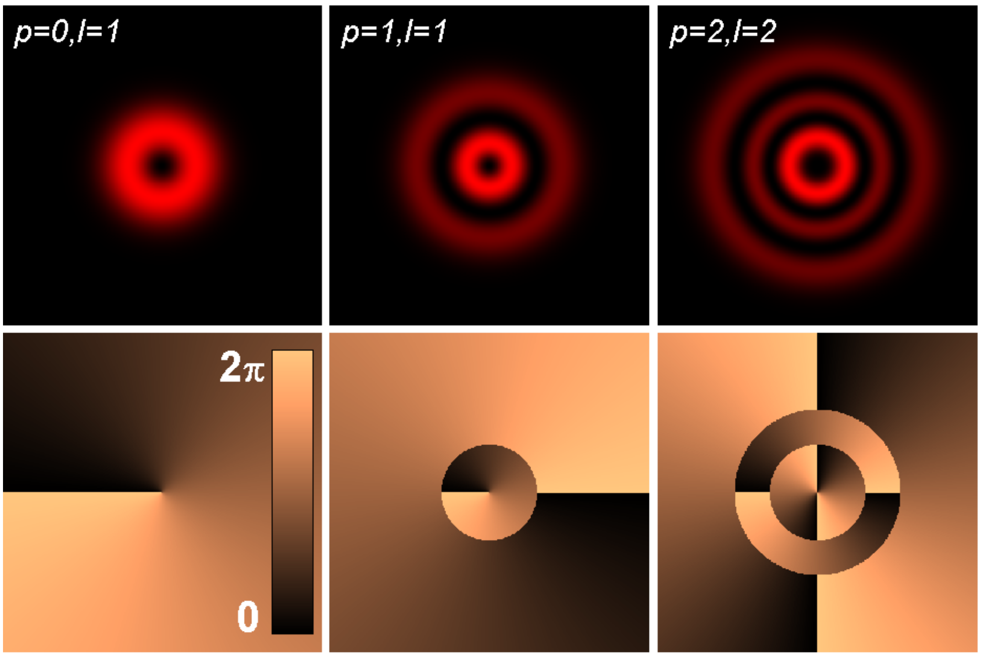

Figure 1.6: Intensity profile (first row) of LG beam for different value of indices along with phase profile (second row).

due to the polarization of light.

Equation (1.26) reduces to the Gaussian beam expression for $p = 0$ and $l = 0$. If only $p = 0$, then the above solution reduces to a vortex beam solution.

1.6.5 Bessel Beams

All the beams mentioned above show diffraction i.e. they spread while propagating in free space. The reason behind it is confinement of their energy in finite region. This spreading is noticeable after the Rayleigh range. However, there exist non-diffracting solutions for the PWE, first predicted by Durnin et al. [39]. These solutions form a class of beams called as Bessel beams [5]. Apart from non-diffracting nature, they also show self-reconstruction property [40].

The field distribution of Bessel beams can be written as

$$A(r, \phi, z) = \exp[ik_z z]J_n[k_r r]\exp[\mathrm{sgn}\, in\phi], \tag{1.28}$$

where J_n is an n^{th} order Bessel function of first kind, k_z and k_r the longitudinal and radial wave vectors, with $k = \sqrt{k_z^2 + k_r^2}$. As seen from the above solution,

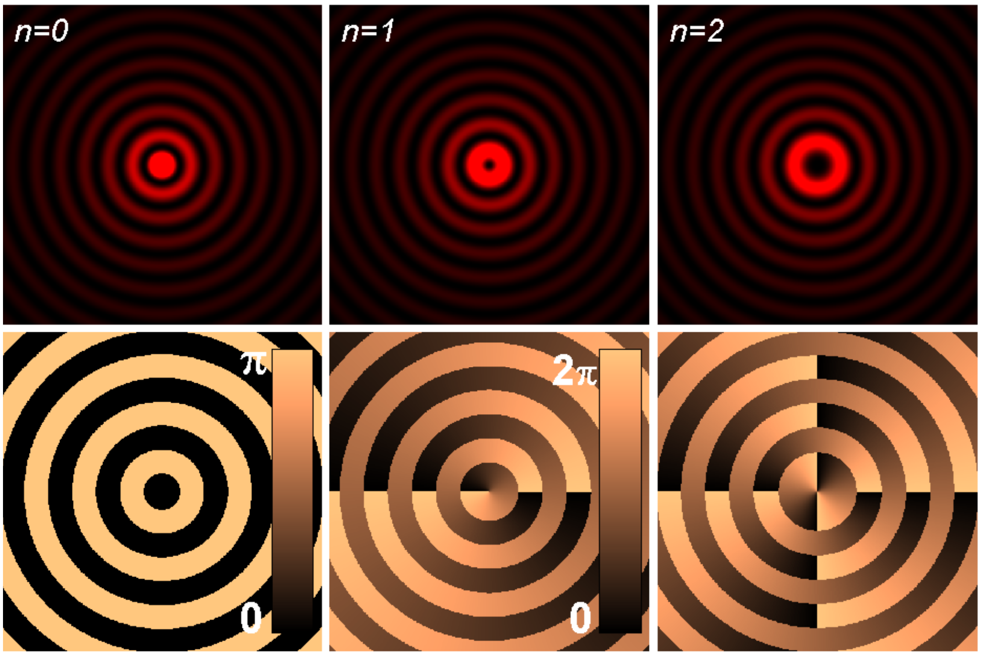

Figure 1.7: Intensity profile (first row) of Bessel beam for different index n along with phase profile (second row).

the higher order Bessel beams have phase singularity due to the phase term exp[sgn $in\phi$]. This phase singularity gives same properties to the beam as mentioned in previous sections. Figure 1.7 shows the intensity distribution and the phase profile for different orders of Bessel beams. It is observed that there is a phase shift of π between adjacent rings of Bessel beams. The above solution of Bessel beam is ideal, it has infinite rings in its intensity profile. However, these infinite power beams can not be realized practically, therefore, one forms truncated Bessel beams using Axicon, computer-generated holography or by Fourier transformation of bright ring [5, 41].

The non-diffracting nature of Bessel beams leads to a wide range of their applications in various fields which include atom optics, nonlinear optics [42], and optical manipulation [5, 43].

1.6.6 Airy Beams

In 1979, Berry and Balazs observed non spreading Airy wave packet as the solution of the Schrödinger equation [44]. This Airy packet has remarkable features: non-dispersive nature and ability to accelerate in absence of any external potential. Due to analogy between the quantum mechanical Schrödinger equation and the paraxial diffraction equation, optics provides an experimental way to realize such wave packets called Airy beams. But in practice, one can not realize this infinite power Airy beams. Hence, one has to truncate it to keep the energy finite. In 2007, Siviloglou et al [4] demonstrated the finite energy optical Airy beams experimentally. The Airy beams were observed to follow a parabolic path similar to the projectile motion in gravitational field. The ballistic dynamics of Airy beams was found to depend on the position of the Fourier lens, the phase mask and the Gaussian beam illuminating the mask [45,46]. Like other diffraction-free beams, the Airy beams also exhibit self healing property [47], for example while propagating through turbulent media, the Airy beams reform themselves and maintain their nature. The Airy beams have found applications in optical trapping [48], and plasma wave-guiding [49].

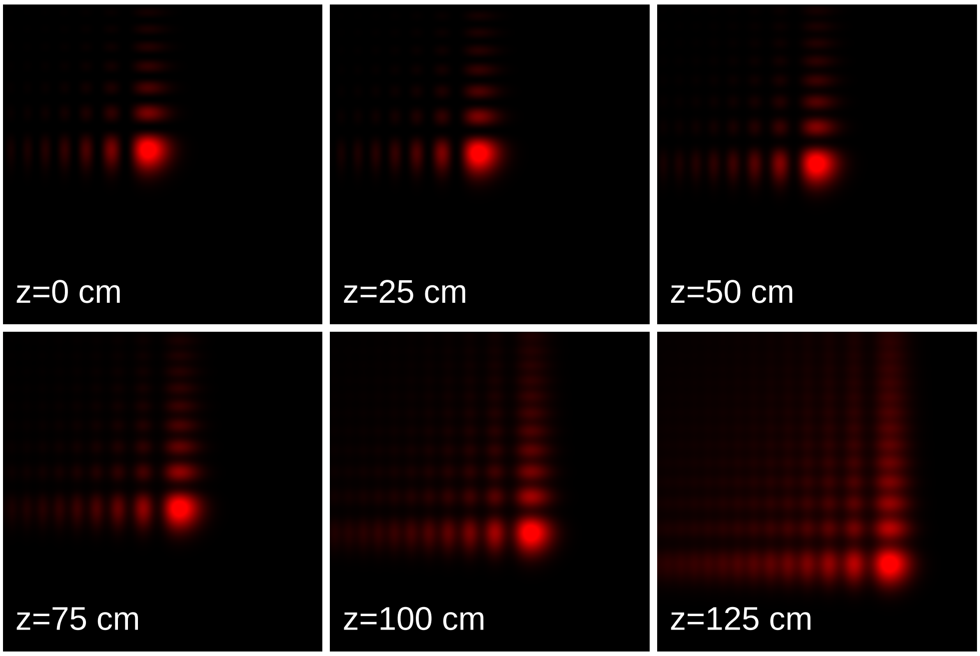

Figure 1.8: Intensity distribution of Airy beams at different propagation distances z.

The field amplitude of Airy beams can be written as,

$$A(x, y, z) = A_x(x, z)A_y(y, z), \tag{1.29}$$

where

$$\begin{aligned} A_x(x, z) &= Ai\left(\frac{x}{x_0} - (\frac{z}{2kx_0^2})^2 + \frac{iaz}{kx_0^2}\right) \\ &\quad \exp[\frac{ax}{x_0} - \frac{a}{2}(\frac{z}{kx_0^2})^2 - \frac{i}{12}(\frac{z}{kx_0^2})^3 + \frac{ia^2}{2}\frac{z}{kx_0^2} + \frac{ix}{2x_0}\frac{z}{kx_0^2}], \\ A_y(y, z) &= Ai(\frac{y}{y_0} - (\frac{z}{2ky_0^2})^2 + \frac{iaz}{ky_0^2}) \\ &\quad \exp[\frac{ay}{y_0} - \frac{a}{2}(\frac{z}{ky_0^2})^2 - \frac{i}{12}(\frac{z}{ky_0^2})^3 + \frac{ia^2}{2}\frac{z}{ky_0^2} + \frac{iy}{2y_0}\frac{z}{ky_0^2}]. \end{aligned} \tag{1.30}$$

In above equations, Ai is the Airy function, a is the aperture parameter and k is the wave number. x_0 and y_0 are the width of main lobe of Airy beams along x-axis and y-axis respectively. The propagation dynamics of Airy beams is shown in Fig. 1.8.

1.7 Fresnel Diffraction Integral

Fresnel diffraction integral is the another way to calculate the propagation of complex field amplitude through homogeneous media. Using Huygens' principle one can derive this formula. The Huygens' principle states that *if an incident field distribution $A_0(x_1, y_1, z_1)$ is present over some closed surface Σ, then each point on that surface acts as the source of a uniform spherical wave or "Huygens' wavelet" which radiates from that point on the surface as shown in Fig. 1.9. At a point P away from the surface, the field is the summation of the fields due to all these Huygens' wavelets coming from all the points on the surface* Σ [1, 2, 6, 50].

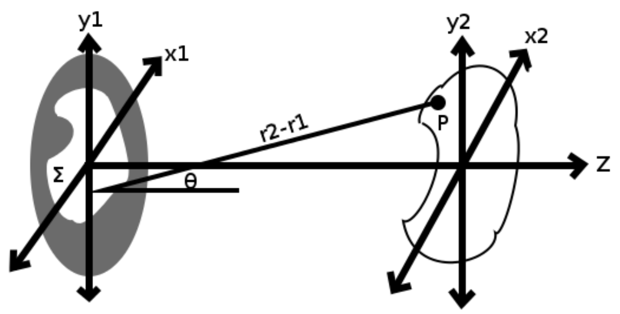

Figure 1.9: Geometry for calculation of Fresnel integral.

Mathematically, one can write this principle as,

$$A(x_2, y_2) = \frac{k}{2\pi i} \iint_{\Sigma} A_0(x_1, y_1) \frac{\exp[ik(r_2 - r_1)]}{r_2 - r_1} \cos\theta ds. \tag{1.31}$$

where ds represents the infinitesimal element of area Σ and $r_2 - r_1$ denotes the distance between an observation point to the source point,

$$r_2 - r_1 = \sqrt{(x_2 - x_1)^2 + (y_2 - y_1)^2 + (z_2 - z_1)^2}. \tag{1.32}$$

In power series, one can expand the above equation as,

$$r_2 - r_1 = z_2 - z_1 + \frac{(x_2 - x_1)^2 + (y_2 - y_1)^2}{2(z_2 - z_1)} + ... \tag{1.33}$$

After dropping higher order terms other than quadratic in the above expression and substituting in Eq. (1.30) with $L = z_2 - z_1$, we get

$$A(x_2, y_2) = \frac{k}{i2\pi L} \iint A_0(x_1, y_1) \exp[\frac{ik}{2L}(2L^2 + (x_1 - x_2)^2 + (y_1 - y_2)^2)] dx_1 dy_1. \tag{1.34}$$

After simplification,

$$\begin{aligned} A(x_2, y_2) &= \frac{k}{i2\pi L} \exp[\frac{ik}{2L}(2L^2 + x_2^2 + y_2^2)] \iint A_0(x_1, y_1) \\ &\quad \exp[\frac{ik}{2L}((x_1^2 + y_1^2) - 2(x_1 x_2 + y_1 y_2))] dx_1 dy_1. \end{aligned} \tag{1.35}$$

The Eq. (1.35) is called as Fresnel diffraction integral. In this thesis work, we have used this integral to calculate beam propagation in free space.

1.8 Aim of the Thesis

Since different beams discussed above have importance in various applications which include optical tweezing, optical communication, and quantum optics, therefore, the study of their dynamics both through linear as well as nonlinear media becomes necessary. In this thesis work we have tried to find out their dynamics in the PR nonlinear media along with free space. One can think this exercise as finding new solutions for PWE with PR nonlinearity.

We consider PR media for following reasons- 1) It requires a beam power of μW only for PR media to show a nonlinear change in index of refraction Δn. 2) This change depends on space charge field which one can control through an external field in the PR media. 3) Also one can do fine tuning of Δn by controlling the ratio of input peak intensity to background illumination.

1.9 Thesis Overview

Chapter 1 contains the basic mathematical expressions and review of the background material. The expressions of PWE for inhomogeneous media and Fresnel integral formula are derived in this chapter. The solutions of PWE for both, the linear and the nonlinear cases are discussed. Chapter 2 is devoted for the generation and characterization of engineered beams. It describes the computer-generated holography technique for generation of these beams. The new methods for the characterization of OAM state of light, proposed by us, are explained over here. Chapter 3 focuses on physics of the PR nonlinearity. The expression for the change in index of refraction in the PR media is derived from the material equations.

Chapter 4 and 5 discuss our observations on propagation of engineered beams through the PR media. We have divided engineered beams into two categories- diffraction broadened and diffraction-free beams. Chapter 4 covers the propagation dynamics of diffraction broadened beams. We consider dipole and quadrupole vortex beams, HG beams, LG beams, and ring lattice beams. The nonlinear dynamics of diffraction-free beams are explained in Chapter 5. Under this category, the propagation of Airy beams and Bessel beams are examined in the PR media. The last chapter gives the summary and scope for future work.

Chapter 2

Generation and Characterization of Engineered Beams

We have seen in the first chapter that the PWE supports different beam solutions like optical vortices, LG, HG, Bessel and Airy beams. Amongst these beams, HG and LG beams can be generated using laser cavity, however, they can not be controlled and modified in real time. The laser cavity can generate only one beam profile at a time. To change the laser mode or beam profile, one has to modify the cavity. To overcome these problems, we have used computer-generated holography technique for generation of these beams. This technique involves phase engineering, therefore, we called these beams as the engineered beams. The computer generated hologram (CGH) modifies the phase of input Gaussian beam in such a way that the diffracted beam from hologram acquires the desired beam profile. The technique incorporates spatial light modulator (SLM) to do phase modulation in real time. It allows to change the beam profile along with the topological charge carried by the beam, number of edge dislocations and screw dislocations in real time. There are some beams like Airy beams, Bessel beams, dipole and quadrupole vortex beams which can not be generated using laser cavity, however, these beams can be produced using computer-generated holography.

In this chapter, we study the method for generation of engineered beams along with their characterization. Section 1 starts with the basic principle of conventional holography. The computer generated holography technique is introduced in Section 2. The detailed discussion on generation of engineered beams is in Section 3. In Section 4, we describe the characterization of engineered beams that includes two new methods for measurement of topological charge or OAM state of singular beams.

2.1 Holography

Gabor proposed a lensless imaging technique now called as holography [3,6,50]. This technique stores both the amplitude and phase of scattered light coming from an object unlike photography. It involves two steps - construction of hologram and reconstruction of image of the object. The hologram can be formed by recording interference pattern generated with scattered light from object and reference wave. An illumination of hologram with reference wave reconstructs the object's image.

2.1.1 Construction of hologram

Figure 2.1 shows the setup for construction of hologram. The light beam from the laser is divided into two parts. First part illuminates the object to be recorded, which scatters the light to form object wave. Second part acts as

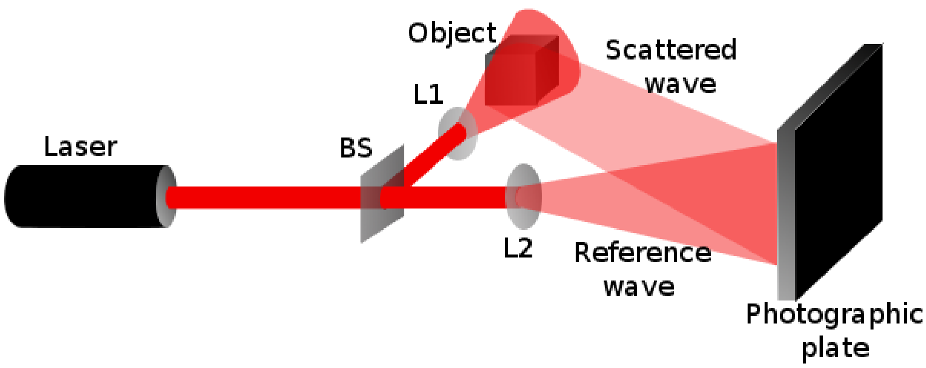

Figure 2.1: Construction of hologram. BS, beam splitter; L1,L2, lens.

a reference wave, which interferes with the object wave. This interference pattern is recorded on some recording material (e.g. photographic plate, PR material). If this pattern is recorded on the photographic plate, then hologram is formed after development of the plate.

Let us consider field distribution for object wave as,

$$A_o(x, y) = a_o(x, y)\mathrm{exp}[-i\phi_o(x, y)], \tag{2.1}$$

where a_o and ϕ_o are the amplitude and the phase of the object wave respectively. In the same way, a_r and ϕ_r are the amplitude and the phase of the reference wave. The field distribution for reference wave is written as,

$$A_r(x, y) = a_r(x, y)\mathrm{exp}[-i\phi_r(x, y)]. \tag{2.2}$$

The interference of object and reference wave is,

$$\begin{aligned} I(x, y) &= |A_o + A_r|^2, \\ &= a_o^2 + a_r^2 + a_o a_r \mathrm{exp}[-i(\phi_o - \phi_r)] + a_o a_r \mathrm{exp}[i(\phi_o - \phi_r)], \quad (2.3) \\ &= a_o^2 + a_r^2 + 2a_o a_r \cos[\phi_o - \phi_r]. \quad (2.4) \end{aligned}$$

The above equation indicates that both the amplitude and the phase are presented in the interference pattern. The different types of hologram can be made depending on the development technique. They are mainly two types- 1) amplitude hologram and 2) phase hologram.

In amplitude hologram, the amplitude of diffracted light from hologram is proportional to the intensity of the recorded light. However, phase hologram just modulates the phase of input beam. The phase hologram can be produced by changing the refractive index or thickness of material in proportion to the intensity of the interference pattern.

The general transmittance function for hologram is written as [51],

$$\begin{aligned} T(x, y) &= \sum_{q=-\infty}^{\infty} t_q \mathrm{exp}[-iq(\phi_o - \phi_r)], \\ &= t_o + \sum_{q=1}^{\infty} t_q \mathrm{exp}[-iq(\phi_o - \phi_r)] + \sum_{q=1}^{\infty} t_{-q} \mathrm{exp}[iq(\phi_o - \phi_r)]. \quad (2.5) \end{aligned}$$

The transmittance coefficient t_q depends on the type of hologram. For an amplitude hologram, q varies from -1 to +1, therefore, Eq. (2.5) becomes,

$$T(x, y) = t_0 + t_1 \exp[-i(\phi_o - \phi_r)] + t_{-1} \exp[i(\phi_o - \phi_r)]. \tag{2.6}$$

where $t_0 = a_o^2 + a_r^2$, and $t_1 = t_{-1} = a_o a_r$. So it is clear from above equation that the transmittance of hologram is proportional to the intensity of interference pattern for amplitude hologram. For a phase hologram, $t_q = J_q(M)$ where J_q is the q^{th} order Bessel function of first kind. M represents the amplitude of phase modulation.

2.1.2 Reconstruction of Object

The setup for reconstruction of object's image is shown in Fig. 2.2. Here, the hologram is illuminated by the wave which is identical to the reference wave previously used for the construction of hologram. In case of amplitude hologram, two images are formed. One is a virtual image and other is a real image of the object. The virtual image has all the features of the object which includes parallax and depth. By using CCD camera, one can capture real image without lens.

Let us first consider amplitude hologram and field distribution for transmitted wave that is written as,

$$\begin{aligned} E_t(x, y) &= T(x, y) E_r(x, y), && (2.7) \\ &= (a_o^2 + a_r^2) a_r \exp[-i\phi_r] + a_o a_r^2 \exp[-i\phi_o], \\ &\quad + a_o a_r^2 \exp[i(\phi_o - 2\phi_r)]. && (2.8) \end{aligned}$$

The first term represents the incident reference wave with amplitude modulation due to a_o^2. The second term represents object wave which forms virtual image of an object. The last term has phase which is complex conjugate of object wave with extra phase modulation of $\exp[-i2\phi_r]$. This term forms the real image.

In case of phase hologram field distribution for transmitted wave is written

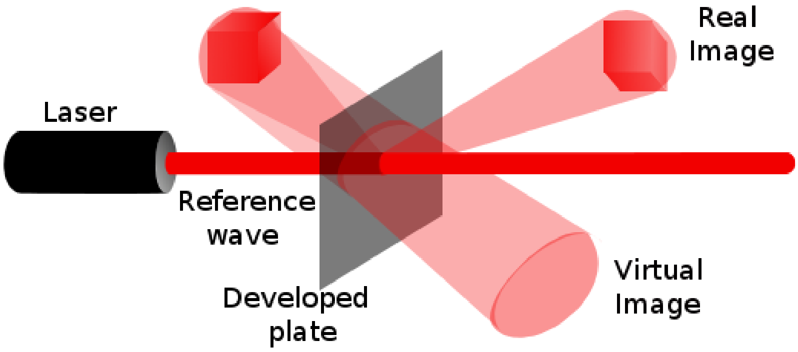

Figure 2.2: Reconstruction of object's image.

as,

$$\begin{aligned} E_t(x,y) &= \sum_{q=-\infty}^{\infty} t_q \exp[-iq(\phi_o-\phi_r)]a_r\exp[-i\phi_r], \\ &= J_0(M)a_r\exp[-i\phi_r] + \sum_{q=1}^{\infty} J_q(M)a_r\exp[-iq(\phi_o)] \\ &\quad + \sum_{q=1}^{\infty} J_{-q}(M)a_r\exp[iq(\phi_o-2\phi_r)]. \end{aligned} \tag{2.9}$$

The first term represents the incident reference wave without any modulation unlike amplitude hologram. The second term has q orders with each order forming a virtual image. The real images are represented by the last term. As one moves from first to higher order, the intensity of both virtual and real images are diminished.

2.2 Computer-Generated Holography

The computer-generated holography is the method in which construction of hologram can be done without optics [50]. The hologram is constructed using a computer program or an algorithm. Therefore, the generated hologram is called as a computer-generated hologram (CGH). The technique involves the generation of object wave for a desired object. One can take objects that have no existence in real world. The CGH formation can be done in three steps. These are as follows:

1) Calculation of Scattered Field of Object

First step involves computation of object wave and its propagation towards hologram plane. The propagation of object wave can be calculated by Fourier transform or Fresnel Transform. Using these two transforms, one can form two holograms called Fourier hologram and Fresnel hologram.

2) Encoding of Field into a Hologram Transmittance

Once the complex field of object at hologram plane is computed, next step involves its representation in hologram. There are different methods to form different types of CGH for example detour-phase hologram, kinoform, and phase contour interferogram.

The kinoform is a hologram which is created by considering phase of the Fourier transform field of object. The encoding of this kind of hologram should be made in the phase range of $(0, 2\pi)$. As the kinoform is pure phase hologram, its diffraction efficiency is very high. The disadvantage of this hologram is its formation of bright spot due to phase mismatching. Phase contour interferogram is formed by interfering object and reference wave digitally. The efficiency of this hologram can be increased by making it blazed. In this thesis work, we have produced this kind of CGH for generation of engineered beams excluding Airy beams.

3) Fabrication of CGH

The third step consists of plotting or transferring of above encoded representation to a holographic sheet or a SLM. The transmittance of these CGHs depends on the plotting devices and the way they are encoded. The process of object reconstruction is same as the conventional holography.

2.3 Generation of Engineered Beams

To generate engineered beams we have used computer-generated holography technique. Since the information about an object wave is needed to form a hologram in both conventional as well as computer-generated holography, we have taken an equation of complex field amplitude for engineered beams as the object wave to form a CGH. And the tilted plane wave is used as our reference wave. By interfering engineered beam with tilted plane wave, we have created interferogram using a LabView program. This interferogram acts as the CGH.

The CGH formation for optical vortex beams using LabView is shown in Fig. 2.3. There are two holograms in the Figure. First hologram is formed by just interfering vortex beam with the tilted plane wave. To avoid extra phase shift due to curvature and Guoy phase, we have chosen interference plane at $z = 0$. Also, amplitude of both the beams are taken as unity for good visibility of interference pattern. The complex field amplitude of vortex beam at $z = 0$,

$$\begin{aligned} A(x,y) &= \left(\frac{x + \text{sgn}\, iy}{w_0}\right)^l \exp[-\frac{(x^2+y^2)}{w_0^2}], \\ &= (\frac{r}{w_0})^l \exp[\text{sgn}\, il\phi] \exp[-(\frac{r}{w_0})^2]. \end{aligned} \tag{2.10}$$

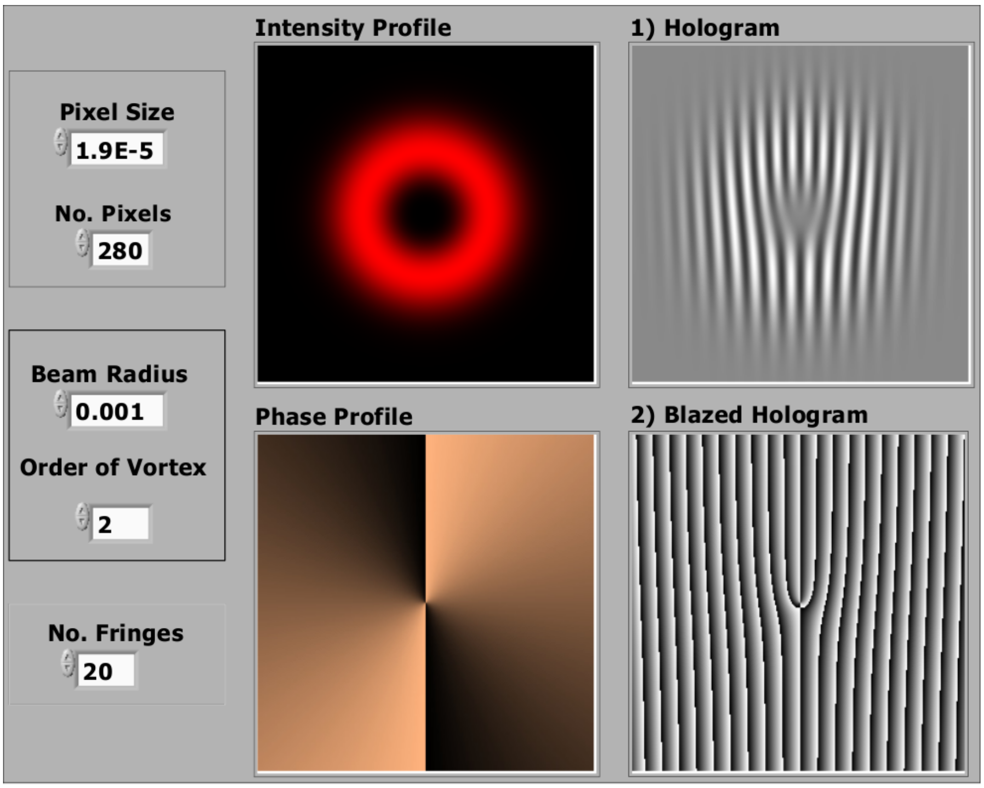

Figure 2.3: CGH for second order optical vortex beam.

The field for tilted plane wave is written as,

$$A_p = \exp[ikx\cos(\theta)] = \exp[i\frac{2\pi nx}{Np}], \tag{2.11}$$

where θ is the tilted angle from the optical axis i.e. z axis and n is the number of fringes. N and p are the total number of pixels and pixel size of the CGH respectively. Now we interfere these two fields,

$$\begin{aligned} I(x,y) &= |A + A_p|^2, \\ &= 1 + (\frac{r}{w_0})^{2l}\exp[-2(\frac{r}{w_0})^2] \\ &\quad +(\frac{r}{w_0})^l\exp[-(\frac{r}{w_0})^2]\exp[i(\frac{2\pi nx}{L} + \mathrm{sgn}\, il\phi)] \\ &\quad +(\frac{r}{w_0})^l\exp[-(\frac{r}{w_0})^2]\exp[-i(\frac{2\pi nx}{L} + \mathrm{sgn}\, il\phi)], \end{aligned} \tag{2.12}$$

where L (=Np) be the length of hologram. It is clear from the above equation that the present hologram not only modulates phase but also intensity of the input light beam due to presence of Gaussian terms in diffracted order.

The second hologram is a blazed hologram which has ideally 100% efficiency. The blazed hologram can be formed by considering phases of engineered beam and tilted plane wave. The equation of blazed hologram for case of a vortex beam is written as

$$I(x,y)_{blazed} = Mod[\frac{2\pi nx}{L} + \mathrm{sgn}\, l\phi, 2\pi]. \tag{2.13}$$

The blazed hologram is pure phase hologram. Their transmittance function is represented by Eq. (2.9). To form optical vortex, one can take print out of the CGH shown in Fig. 2.3 on a holographic sheet. However, we have used SLM in this thesis work.

2.3.1 Spatial Light Modulator

As its name, SLM modulates light field spatially [50]. There are two types of SLM- 1) Electrically addressed SLM and 2) Optically addressed SLM. The electrically addressed SLM is a device with an array of pixels which modulate light spatially according to value of the voltage applied on it. Each pixel

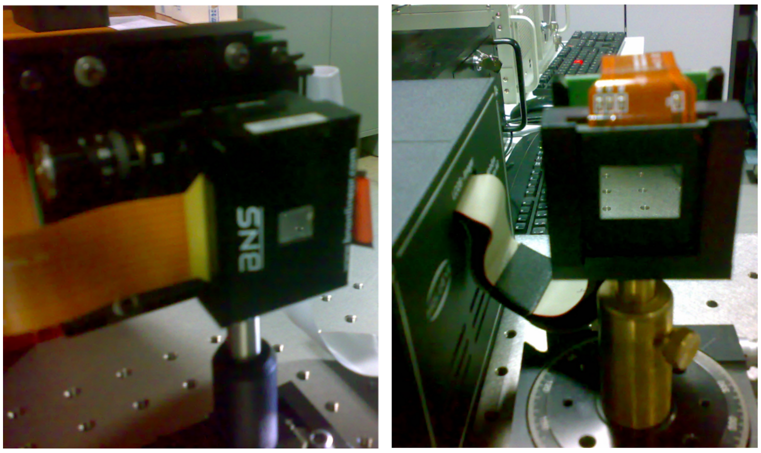

Figure 2.4: a) P512-0532 Spatial Light Modulator (left side) b) LC-R2500 Spatial Light Modulator (right side).

consists of liquid crystal cell sandwiched between two electrodes. The SLM is further divided into two types- A) Reflective type SLM and B) Transmissive type SLM. We have two SLMs both electrically addressed reflective types- I) LC-R2500 Spatial Light Modulator from Holoeye, Germany and II) P512-0532 Spatial Light Modulator from Boulder Nonlinear Systems, USA. The images of these SLMs are shown in Fig. 2.4. The SLM is a versatile device which has uses in beam shaping, data processing, creation of spatial filter and holographic optical tweezer. We have used SLM for generation of engineered beams in this thesis work. One can send the image of CGH directly to the SLM using same computer which generates the CGH. In the SLM, phase range $(0, 2\pi)$ of the CGH converts into voltage range. It has maximum voltage for zero phase, whereas zero voltage for 2π phase. When maximum voltage is applied to a pixel, there is no phase delay for an incident light, however, it experiences 2π phase shift in the absence of voltage in case of P512-0532 SLM.

2.3.2 Experimental Setup for Generation of Engineered Beams

Figure 2.5 shows typical experimental setup for generation of engineered beams. The laser beam having Gaussian distribution is illuminated on SLM. The CGH, like the vortex's CGH shown in Fig 2.3, is sent to the SLM using computer.

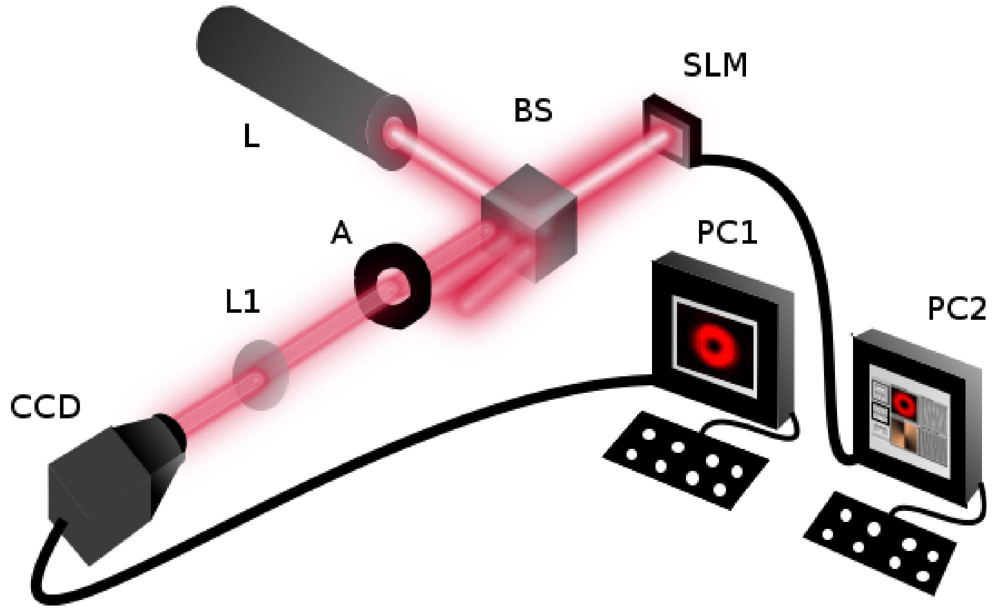

Figure 2.5: Experimental Setup. L, laser; BS, beam-splitter; SLM, spatial light modulator; L1, lens; CCD, camera; PC1, PC2, Computer.

As the CGH is for second order optical vortex beam, this beam is generated in the first diffracted order, that is selected by an aperture. A lens is used to form beam waist at the focus, so that one can study the propagation dynamics of beam from focus. The images of beam can be taken by a CCD camera.

2.4 Characterization of Engineered Beams

It is necessary to confirm that the generated beam is our desired beam. By recording the intensity profile, one can identify the HG beams, Airy beams, and zeroth order Bessel beam. However, it is difficult to recognize the topological charge or OAM for the beams with phase singularity. In recent years, a lot of attention is being given to the measurement of OAM states of light field due to their application in communication and quantum cryptography [35, 36]. Recently, the triangular aperture, annular aperture, and axicon have been used to identify the topological charge of the vortex [52–56]. Apart from these techniques, the spatial light modulator (SLM) has been utilized for discriminating the charge of the vortex [57–59]. Our group has shown that the Fourier transform of the intensity distribution of the vortex, its spatial correlation function, and the Wigner distribution function can also provide information about the topological charge of the vortex [60, 61].

In this thesis work we have proposed two new techniques to calculate the OAM of light field. We have applied these techniques to optical vortices only, however, one can use it for LG beams and higher order Bessel beams which also contain singularities.

2.4.1 Measurement of the Orbital Angular Momentum using Quadratic Phase Mask

In this technique we construct a quadratic phase mask (QPM) using the same SLM which is used to generate optical vortices [62]. A vortex diffracted through this mask shows very interesting dynamics that is found to be different in positive (+) and negative (-) first order diffraction. In (-) diffracted order, the optical vortex beam with topological charge l transforms into $l + 1$ intensity components. Therefore, by measuring the number of intensity components, one can determine the topological charge of vortex while the orientation of these components can provide us with the sign of vortex. This kind of transformation is not observed in (+) diffraction for the same distance of propagation. The above method of charge determination does not require optical elements and their alignment unlike interferometry. which has been the technique in vogue for finding the charge of vortices.

Theory

The optical vortex has complex field amplitude

$$A(x_1, y_1) = \left(\frac{x_1 + \text{sgn}\, iy_1}{w_0}\right)^l \exp[-\frac{(x_1^2 + y_1^2)}{w_0^2}], \tag{2.14}$$

where w_0 is the beam radius at $z = 0$ and sgn denotes the sign of topological charge which is +1 for positive and -1 for negative. By using Binomial expansion, Eq. (2.14) becomes,

$$A(x_1, y_1) = \sum_{n=0}^{l} \frac{l!}{w_0^l(n!(l-n)!)} x_1^{l-n} (\text{sgn}\, iy_1)^n \exp[-\frac{(x_1^2 + y_1^2)}{w_0^2}]. \tag{2.15}$$

The transmittance function of QPM is given by

$$t(y_1) = \exp\left[\frac{iM}{2}\cos\left[\frac{4\pi}{3w_f^2}(y_1 - y_0)^2\right]\right], \tag{2.16}$$

where y_0 is the shift from center maxima. w_f is the full width at half maxima of argument of the above function. M is the peak to peak excursion of the phase delay. Using Jacobi-Anger expansion [63], one can write Eq. (2.16) as,

$$t(y_1) = \sum_{q=-\infty}^{\infty} i^q J_q[M/2]\exp\left[\frac{iq}{f^2}(y_1 - y_0)^2\right], \tag{2.17}$$

where $f = \sqrt{3w_f^2/4\pi}$. The field at QPM ($z = 0$)

$$A_t(x_1, y_1) = t(y_1)A(x_1, y_1). \tag{2.18}$$

After substituting value of $t(y_1)$ and $A(x_1, y_1)$ in the above equation, we get

$$\begin{aligned} A_t(x_1, y_1) &= \sum_{q=-\infty}^{\infty} i^q J_q[M/2]\exp\left[\frac{iq}{f^2}(y_1 - y_0)^2\right] \\ &\times \sum_{n=0}^{l} \frac{l!}{w_0^l(n!(l-n)!)} x_1^{l-n}(\mathrm{sgn}\, iy_1)^n \exp[-\frac{(x_1^2 + y_1^2)}{w_0^2}]. \end{aligned} \tag{2.19}$$

The field distribution at a distance $z = L$ from the SLM can be calculated using Fresnel diffraction integral (Eq. (1.35)),

$$\begin{aligned} A(x_2, y_2) &= \frac{k}{i2\pi L}\exp[\frac{ik}{2L}(2L^2 + x_2^2 + y_2^2)] \iint A_t(x_1, y_1) \\ &\times \exp[\frac{ik}{2L}((x_1^2 + y_1^2) - 2(x_1x_2 + y_1y_2))]dx_1dy_1. \end{aligned} \tag{2.20}$$

Putting Eq. (2.19) in Eq. (2.20), we obtain

$$\begin{aligned} A(x_2, y_2) &= \frac{k}{i2\pi L}\exp[\frac{ik}{2L}(2L^2 + x_2^2 + y_2^2)] \sum_{q=-\infty}^{\infty} i^q J_q[M/2]\exp[\frac{iqy_0^2}{f^2}] \\ &\times \sum_{n=0}^{l} \frac{i^n \mathrm{sgn}^n l!}{w_0^l(n!(l-n)!)} \iint y_1^n x_1^{l-n} \exp[-\frac{(x_1^2 + y_1^2)}{w_0^2}]\exp[\frac{ik}{2L}(x_1^2 + y_1^2)] \\ &\times \exp[\frac{-ik}{L}(x_1x_2 + y_1y_2)]\exp\left[\frac{iq}{f^2}(y_1^2 - 2y_0y_1)\right] dx_1dy_1. \end{aligned} \tag{2.21}$$

Let us first consider an integration with respect to x,

$$I_x = \int x_1^{l-n} \exp[-(\frac{x_1^2}{d_x^2} - \frac{2kx_1x_2}{i2L})]dx_1, \tag{2.22}$$

where

$$\frac{1}{d_x^2} = \frac{1}{w_0^2} - \frac{ik}{2L}. \tag{2.23}$$

To solve the above integral we have used the following standard integral [64],

$$\int x^n \exp[-(x^2 - 2xB)]dx = \frac{\sqrt{\pi}}{(2i)^n} H_n[iB]\exp[B^2]. \tag{2.24}$$

Using above standard integral, we get

$$I_x = \frac{d_x^{l-n+1}\sqrt{\pi}}{(2i)^{l-n}} H_{l-n}[\frac{kd_xx_2}{2L}]\exp[-(\frac{kd_xx_2}{2L})^2]. \tag{2.25}$$

Now, consider an integration with respect to y,

$$I_y = \int y_1^n \exp[-(\frac{y_1^2}{d_y^2} - \frac{2ky_1y_s}{i2L})]dy_1, \tag{2.26}$$

where

$$\frac{1}{d_y^2} = \frac{1}{w_0^2} - \frac{ik}{2L} - \frac{iq}{f^2}, y_s = y_2 + \frac{2Lqy_0}{kf^2}. \tag{2.27}$$

Again using standard integral (Eq. (2.24)), we get

$$I_y = \frac{d_y^{n+1}\sqrt{\pi}}{(2i)^n} H_n[\frac{kd_yy_s}{2L}]\exp[-(\frac{kd_yy_s}{2L})^2]. \tag{2.28}$$

After Substituting Eqs. (2.25) and (2.28) in Eq. (2.21), we obtain

$$\begin{aligned} A(x_2, y_2) = & \frac{k}{2L(2w_0)^l} \sum_{q=-\infty}^{\infty} i^q J_q(M/2)\exp[\frac{i4\pi qy_0^2}{3w_f^2}]\exp[-(\frac{x_2^2}{w_x^2} + \frac{(y_2+by_0)^2}{w_y^2})] \\ & \times \exp[\frac{ik}{2}(2L + \frac{x_2^2}{R_x} + \frac{y_2^2}{L} - \frac{(y_2+by_0)^2}{R_y})] \sum_{n=0}^{l} \frac{l!\mathrm{sgn}^n(-i)^{l-n+1}}{n!(l-n)!} \\ & \times d_x^{l-n+1} d_y^{n+1} H_{l-n}[\frac{kd_xx_2}{2L}] H_n[\frac{kd_y(y_2+by_0)}{2L}], \end{aligned} \tag{2.29}$$

where

$$z_r = \frac{kw_0^2}{2}, b = \frac{8\pi Lq}{3kw_f^2}, R_x = L + \frac{z_r^2}{L}, R_y = \frac{L}{(1+b)}[(1+b)^2 + (\frac{L}{z_r})^2], \tag{2.30}$$

$$w_x = w_0\sqrt{1+(\frac{L}{z_r})^2}, w_y = w_0\sqrt{(1+b)^2+(\frac{L}{z_r})^2}, \tag{2.31}$$

$$d_x = \frac{w_0}{\sqrt{1-i\frac{z_r}{L}}}, d_y = \frac{w_0}{\sqrt{1-i(1+b)\frac{z_r}{L}}}. \tag{2.32}$$

In Eq. (2.29), H_n is the Hermite polynomial of order n. w_x, R_x and w_y, R_y are the beam radius and the radius of curvature along the x and y axes respectively. Equation (2.31) shows that the beam radius along the x axis remains the same for both the orders. However, the beam radius along the y axis being dependent on q, the order of diffraction, is different for different orders. Moreover, due to the quadratic phase variation in the phase mask, phase shifts will be different for wavefronts propagating in (+) and (-) diffracted orders [65]. This diffraction order dependence is responsible for different dynamics between positive and negative diffraction orders. A careful observation of Eq. (2.29) will show that the vortex becomes elliptical as it propagates under quadratic phase transformation. It should be noted that if $t(y_1)$ in Eq. (2.16) is replaced by its complex conjugate, positive diffraction orders become negative and vice versa. However, the respective dynamics remains the same.

Experimental Setup

The experimental setup is shown in Fig. 2.6. We have used an intensity stabilized He-Ne laser (Spectra-Physics, Model 117A) as the light source. The screen of the SLM (Holoeye, LCR-2500) is divided into two parts, one for a forked grating to make vortices and the other for the QPM ($w_f = 0.61$ mm), which is shown in the inset. The grayscale of the QPM represents phase modulation. By illuminating the part of the SLM that contains the forked grating with the laser beam, the optical vortex is generated as a diffracted order in the reflection. A biconvex lens ($f = 50$ cm) is used to focus the vortex beam on the other part of the SLM where the QPM is situated. This helps to create the waist ($w_0 = 0.35$ mm) at the phase mask, i.e., $z = 0$ with a view to study the propagation dynamics. The CCD camera (Media Cybernetics, Evolution VF cooled color camera) is used to capture the images at various

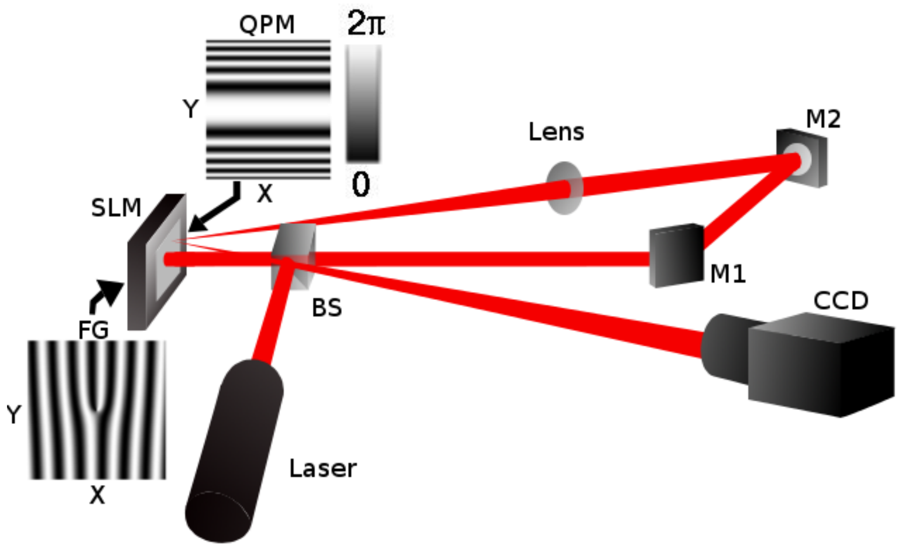

Figure 2.6: Experimental Setup: BS, beam-splitter; SLM, spatial light modulator; M1, M2, mirrors; CCD, camera; QPM, quadratic space mask; FG, fork grating.

propagation distances.

Results and Discussion

The propagation dynamics of diffracted vortex beams formed in (+) and (-) orders are shown in Fig. 2.7 for a negatively charged vortex with $l = 2$. At $z = 20$ cm, diffracted vortices become elliptical in both of the diffraction orders but with different beam radii. As the distance increases, ellipticity in the diffracted beams increases, which leads to the formation of secondary vortices in both the orders. One can see that in the (-) diffraction order, the secondary vortices form at smaller values of z compared to the (+) diffraction order. The observed results are due to dependence of w_y on the diffraction order, as shown in Eq.(2.31). In the (-) diffracted order, the diffracted vortex beam breaks into three intensity components at larger values of z. And the single charged secondary vortices are seated between the intensity components [66].

Figure 2.8 shows theoretical results for the propagation dynamics of diffracted vortices both negative and positive orders. Note that the pitchfork hologram does not produce pure LG modes; rather, it is a superposition of infinite LG modes [51]. However, as shown by our experiments [60, 61], the first-order

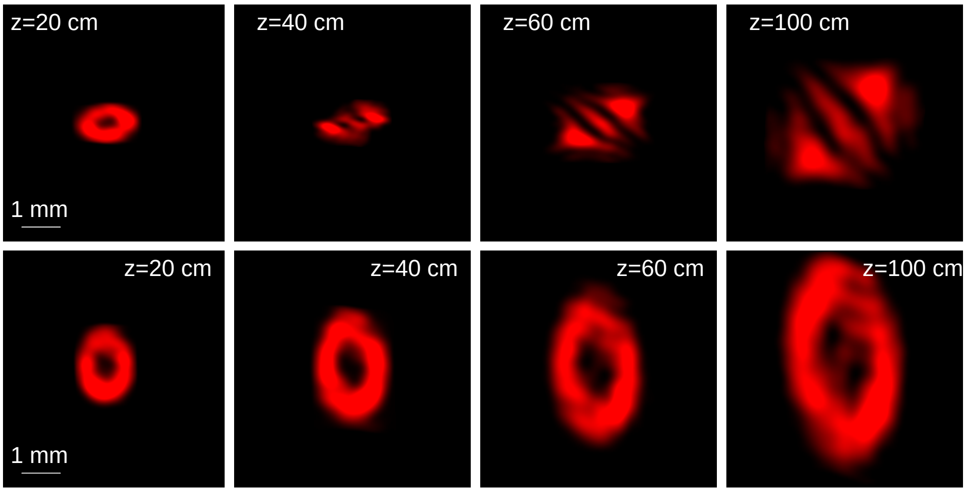

Figure 2.7: Experimental intensity profiles of negative (first row) and positive (second row) diffraction order at different distance z.

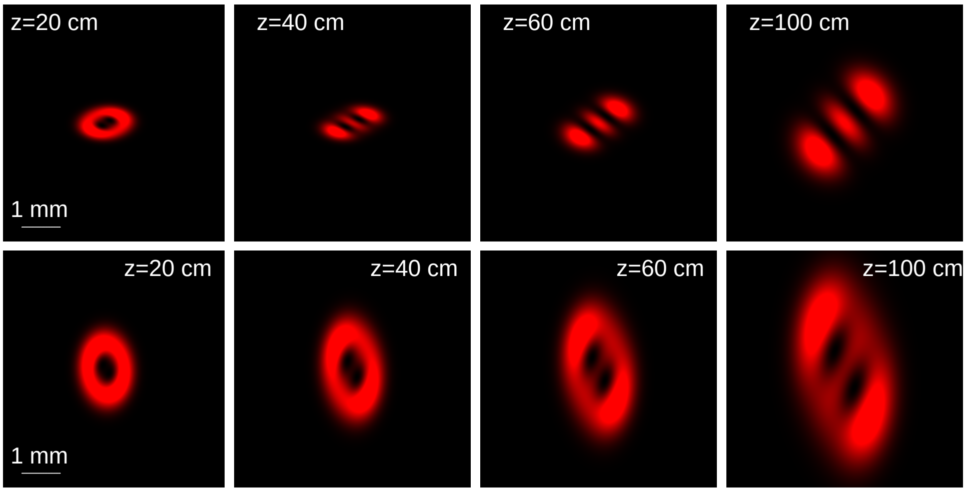

Figure 2.8: Theoretical intensity profiles of negative (first row) and positive (second row) diffraction order at different distance z.

diffraction will have a dominant mode according to the fork hologram used. In the present experiment also, although there is a difference in the shape and size of the spots between the theory and the experiment due to the presence of other modes, the number of spots characteristically remains the same. Although the diffraction pattern looks like HG modes obtained through a cylindrical lens mode converter (CLMC) [38], unlike CLMC, the QPM does not act as a mode converter. It transforms primary vortices into secondary vortices under quadratic phase transformation [66]. The transformation changes the

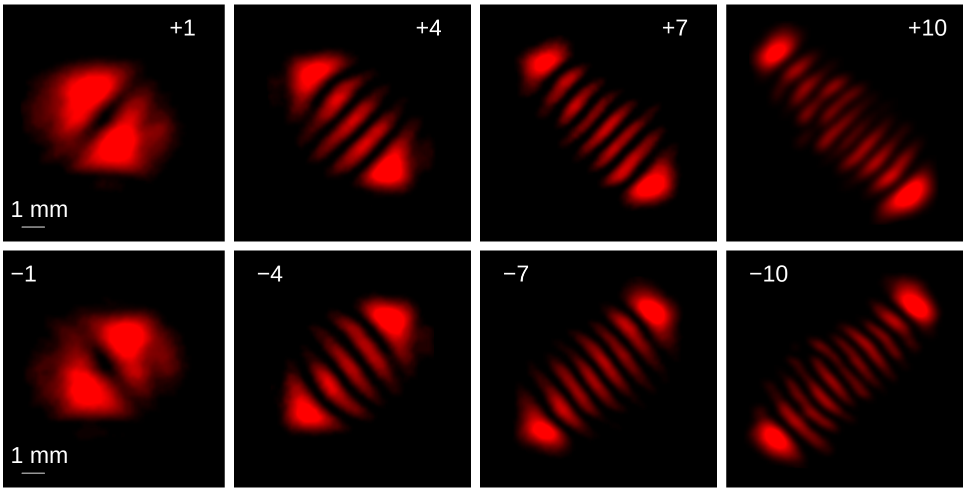

Figure 2.9: Experimental intensity profiles of positively (first row) and negatively (second row) charged vortices at distance $z = 110$ cm.

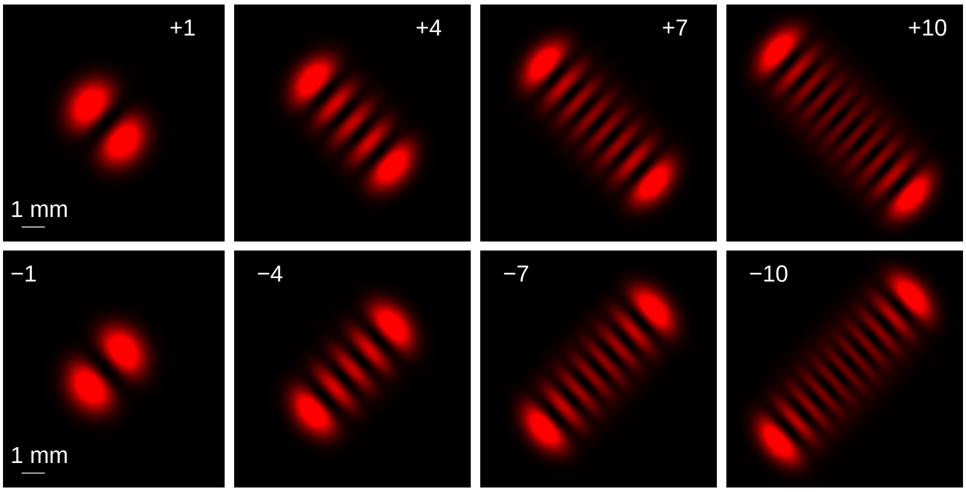

Figure 2.10: Theoretical intensity profiles corresponding to experimental intensity profiles in Fig. 2.9

nature of dislocations that depend on the parameters of the input beam as well as of the phase mask.

Figure 2.9 shows the intensity distribution of the (-) diffracted order generated from the QPM for different topological charges of the vortex, both positive and negative, at $z = 110$ cm, i.e., in the far field. It is observed that the vortex of charge l breaks into $l + 1$ intensity components with a certain orientation. Therefore, by looking at the intensity components, one can easily recognize the topological charge of the optical vortex beam or the OAM state of the beam. The orientation of intensity components flips by 90° for a change in the sign of charge of the vortex. For the positively charged vortex, intensity components align themselves in the second and fourth quadrant whereas for the negatively charged vortex, it is in the first and third quadrant, as shown in Fig. 2.9. We could identify the topological charge along with its sign for vortices up to $l = 10$. The corresponding theoretical intensity distributions obtained from Eq. (2.29), for the same values of the topological charge are shown in Fig. 2.10. This is in good agreement with the experiment. We have verified our results with the complex conjugate of the transmittance function $t(y_1)$ as well. It simply replaces positive diffraction orders with negative and vice versa however, the respective dynamics remains the same.

2.4.2 Measurement of the Orbital Angular Momentum using Simple Biconvex Lens

In this technique, we have utilized a simple spherical biconvex lens to characterize the sign and the magnitude of charge of the optical vortices. The optical vortices of different orders are generated using the SLM and propagated through a lens. As the lens rotates around the y_1-axis, an l^{th} order vortex beam breaks into $l+1$ intensity spots and their orientation gives the sign of the topological charge of vortex.

Theory

The complex field distribution of an optical vortex embedded in a Gaussian beam at $z = z_1$ can be written as (Eq. (1.25)

$$\begin{aligned} A(x_1, y_1, z_1) &= (x_1 + \mathrm{sgn}\, i y_1)^l \frac{w_0}{w^{l+1}} \exp[-\frac{(x_1^2 + y_1^2)}{w^2}] \\ &\quad \times \exp[ik\frac{(x_1^2 + y_1^2)}{2R}] \exp[ikz_1 - i\psi], \end{aligned} \tag{2.33}$$

where

$$w = w_0\sqrt{1 + (\frac{z_1}{z_r})^2}, \psi = \tan^{-1}(\frac{z_1}{z_r}), R = \frac{z_1^2 + z_r^2}{z_1}.$$

Now, consider a spherical lens with focal length f, tilted with an angle θ

along the y_1- axis. The phase factor for such a tilted lens is written as [50]

$$L(x_1, y_1) = \exp[-\frac{ik}{2f}(x_1'^2 + y_1'^2)], \quad (2.34)$$

where (x_1', y_1', z_1') are the new coordinates for the tilted lens which can be written in terms of old coordinates (x_1, y_1, z_1),

$$x_1' = x_1\cos\theta + z_1\sin\theta, y_1' = y_1, z_1' = -x_1\sin\theta + z_1\cos\theta. \quad (2.35)$$

By substituting Eq. (2.35) into Eq. (2.34), the phase factor of lens becomes,

$$L(x_1, y_1) = \exp[-\frac{ik}{2f}((x_1\cos\theta)^2 + (z_1\sin\theta)^2 + 2x_1z_1\cos\theta\sin\theta + y_1^2)]. \quad (2.36)$$

Let the optical vortex beam pass through the tilted spherical lens at $z = z_1$ plane. Therefore, the complex field amplitude at a point (x_1, y_1) in a plane transverse to $z = z_1$ can be written as

$$A_1(x_1, y_1) = A(x_1, y_1)L(x_1, y_1). \quad (2.37)$$

First we put Eq. (2.33) and (2.36) in Eq. (2.37), then putting Eq. (2.37) in Eq. (2.20), we obtain

$$\begin{aligned} A(x_2, y_2) &= \frac{kw_0}{i2\pi Lw^{l-1}}\exp[\frac{ik}{2L}(2L^2 + x_2^2 + y_2^2)]\exp[ikz_1 - i\psi - \frac{ikz_1^2\sin^2\theta]}{2f}] \\ &\times\sum_{n=0}^{l}\frac{(i\mathrm{sgn})^{l-n}l!}{(n!(l-n)!)}\iint x_1^n y_1^{l-n}\exp[-\frac{(x_1^2 + y_1^2}{w^2} + \frac{ik(x_1^2 + y_1^2}{2R}] \\ &\times\exp[\frac{-ik}{2f}(x_1^2\cos^2\theta + y_1^2 + 2x_1z_1\sin\theta\cos\theta)] \\ &\times\exp[\frac{ik}{2L}((x_1^2 + y_1^2) - 2(x_1x_2 + y_1y_2))]dx_1dy_1. \end{aligned} \quad (2.38)$$

We have used Binomial expansion in above equation. Let us first consider an integration with respect to x,

$$I_x = \int x_1^n\exp[-(\frac{x_1^2}{l_x^2} - \frac{2kx_1x_2'}{i2L})]dx_1, \quad (2.39)$$

where

$$\frac{1}{l_x^2} = \frac{1}{w^2} - \frac{ik}{2R} - \frac{ik}{2L} + \frac{ik\cos^2\theta}{2f}, x_2' = x_2 + \frac{Lz_1}{f}\cos\theta\sin\theta. \quad (2.40)$$

Using standard integral (Eq. (2.24)), we get

$$I_x = \frac{l_x^{n+1}\sqrt{\pi}}{(2i)^n} H_n[\frac{kl_x x_2'}{2L}]\text{exp}[-(\frac{kl_x x_2'}{2L})^2]. \tag{2.41}$$

Now, consider an integral with respect to y,

$$I_y \;=\; \int y_1^{l-n}\text{exp}[-(\frac{y_1^2}{l_y^2} - \frac{2ky_1y_2}{i2L})]dy_1, \tag{2.42}$$

where

$$\frac{1}{w_y^2} = \frac{1}{w^2} - \frac{ik}{2R} + \frac{ik}{2f} - \frac{ik}{2L}. \tag{2.43}$$

Again using standard integral (Eq. (2.24)), we obtain

$$I_y = \frac{l_y^{l-n+1}\sqrt{\pi}}{(2i)^{l-n+1}} H_{l-n}[\frac{kl_y y_2}{2L}]\text{exp}[-(\frac{kl_y y_2}{2L})^2]. \tag{2.44}$$

After Substituting Eq. (2.41) and (2.44) in Eq (2.38), we get

$$\begin{aligned} A_2(x_2, y_2) \;&=\; \frac{kw_0}{(2w)^{l+1}L}\text{exp}[-(\frac{k}{2L})^2((l_x x_2')^2 + (l_y y_2)^2)] \\ &\times\text{exp}[\frac{ik}{2L}(x_2^2 + y_2^2) - i(l+1)\psi]\text{exp}[ik(z_1 + L - \frac{(z_1\text{sin}\theta)^2}{2f})] \\ &\times\sum_{n=0}^{l}\frac{l!\text{sgn}^n(-i)^{l-n+1}}{n!(l-n)!}l_x^{n+1}l_y^{l-n+1}H_n[\frac{k}{2L}l_x x_2']H_{l-n}[\frac{k}{2L}l_y y_2]. \end{aligned} \tag{2.45}$$

In above equation, H_n is the Hermite polynomial of order n. At $\theta = 0$ i.e. when there is no tilt, there is no change in the input optical vortex. But as the angle of rotation increases, the phase between two terms of the series in Eq. (2.45) changes which results into two intensity lobes for $l = 1$ at the focus. Similar behavior is observed for higher order vortices also. A vortex of order l breaks into $l + 1$ intensity components. The 45^o oriented Hermite-Gaussian (HG) mode will be formed, if phase difference between the successive terms in Eq. (2.45) becomes zero. However, a small phase difference is always there for all rotation angles, so no pure HG mode will be formed in our case. It should be noted that the two cylindrical lens system has been used to convert a Laguerre-Gaussian (LG) mode containing a vortex into 45° oriented HG mode and vice versa [38].

Experimental Setup

The experimental setup is shown in Fig. 2.5. The phase masks for vortex beams of different orders are constructed using computer generated holography technique and sent to the SLM (Holoeye, LCR-2500) via a computer. The SLM illuminated by a He-Ne Laser (Spectra-Physics, Model 117A) of wavelength 632.8 nm provides us with the desired vortex. Our experimental proposal is implemented using a spherical biconvex lens of focal length $f = 50$ cm. The vortex beam is passed through the lens and recorded with a CCD camera (MediaCybernetics, Evolution VF cooled Color Camera) at the focal point of lens. The lens is kept on a rotation stage (least count of 0.1°). The rotation is performed around y_1-axis with z_1-axis as the optical axis of lens.

Results and Discussion

Figure 2.11 shows the intensity distribution of optical vortex with unit charge at the focal point of lens for different values of rotation angles. The experimental results displayed in the first row are for positively charged vortex while the second row for negatively charged. It can be seen that for $\theta = 0$, the optical vortex remains as it is. At small rotation angles, the optical vortex becomes elliptical. As we increase the angle, optical vortex starts breaking.

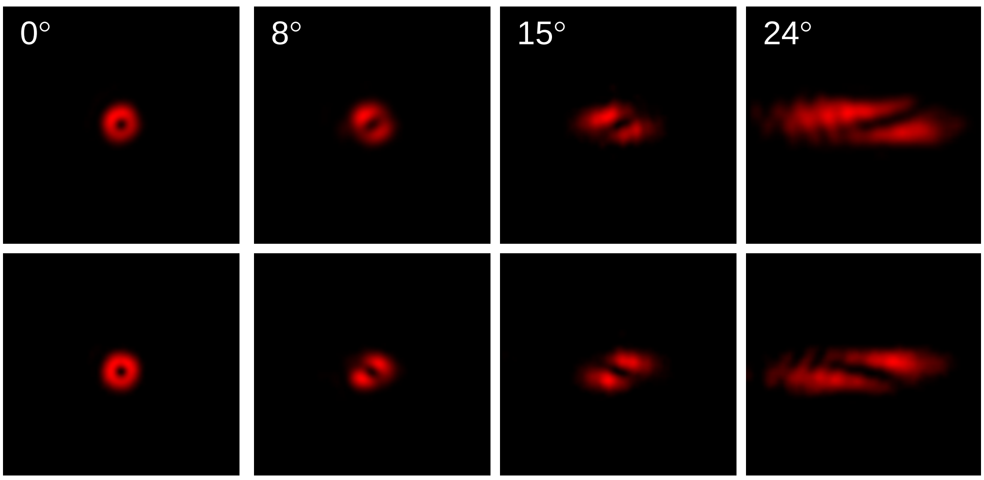

Figure 2.11: Experimental intensity distributions at the focus for the first order vortex - positively charged (top) and negatively charged (bottom), for different rotation angles.

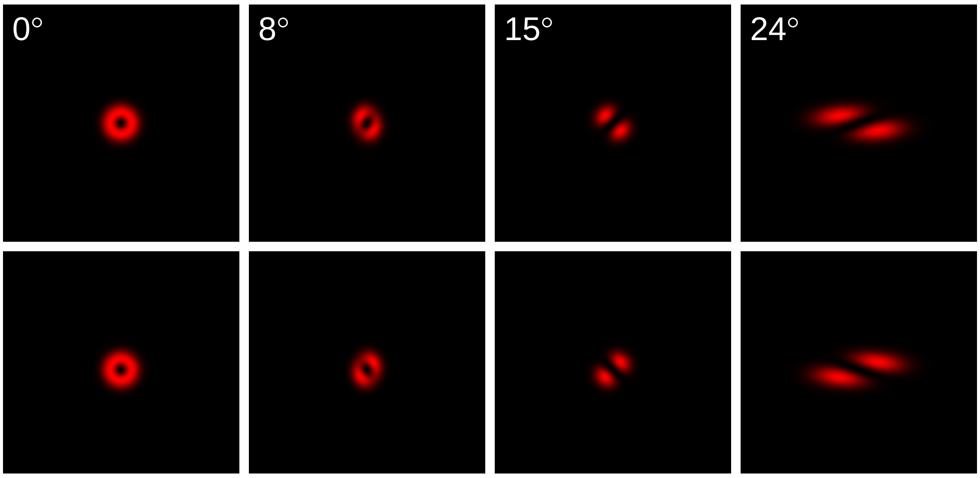

Figure 2.12: Theoretical intensity distributions corresponding to experimental intensity distributions in Fig. 2.11

At the rotation angle of 15° we observe that a single charge vortex breaks into two parts. The break away parts align themselves either clockwise or counter-clockwise depending on the sign of topological charge of the vortex. We have verified experimental results with theoretical calculations using experimental parameters ($w_0 = 0.16$ mm, $z_1 = 120$ cm and $L = 90$ cm). The experimental results are in good agreement with the theoretical results.

We have repeated the process for higher order vortices also. Figure 2.13 shows results for vortices up to fourteenth order, both positive and negative charge, keeping lens rotation angle as 15°. By counting the number of peaks in the intensity distribution one can easily recognize the charge of input vortex beam, for a vortex of charge l, it was always been found to be $l + 1$.

The above setup breaks optical vortex into intensity components at the focal point. As one moves away from the focus the optical vortex reappears. However, one can use another lens to create magnified image of the intensity components on a screen. It must be pointed out that a similar break up of vortices has been observed in the context of lens astigmatism [38, 66–68].

The triangular aperture could find the topological charge of optical vortex upto the eighth order only [52–54]. As the order of vortex increases further, it becomes difficult to resolve the spots, moreover, there is problem of alignment. If alignment is not proper then the measurement of intensity spots becomes

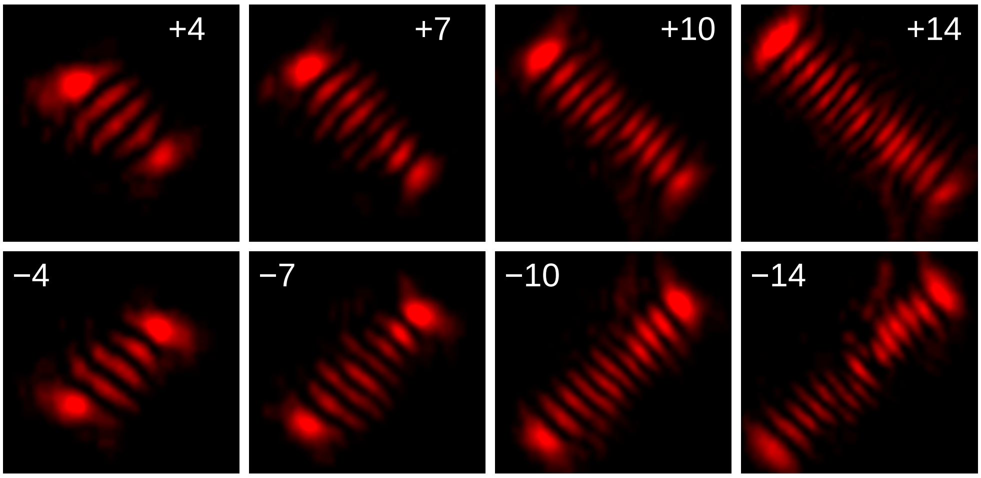

Figure 2.13: Experimental intensity distributions at the focus for vortices of different topological charges.

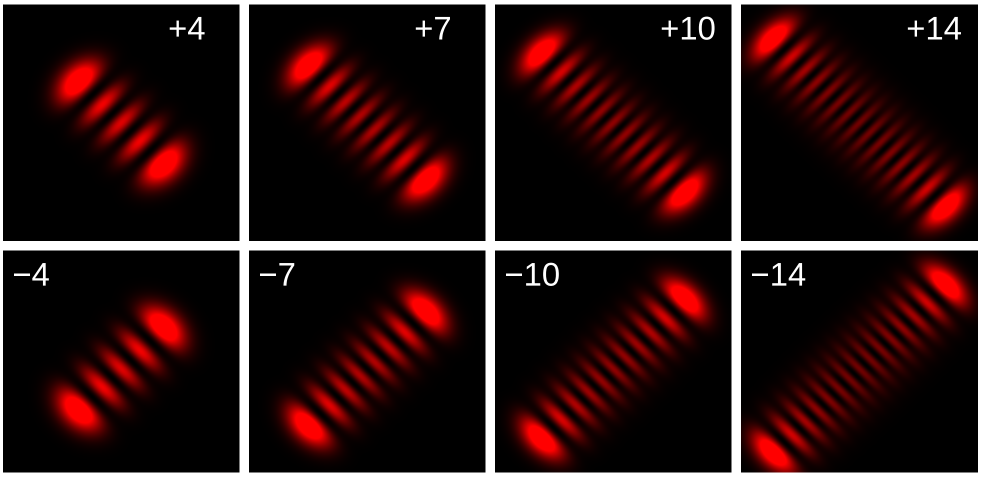

Figure 2.14: Theoretical intensity distributions corresponding to experimental intensity distributions in Fig. 2.13.

critical. However, in our case it is the misalignment that leads to the formation of intensity components. If one can generate a higher order vortex then its charge can be measured by this technique.

We have generated the optical vortices of different orders, both positive and negative charges, using the SLM. We have given methods to find out the OAM states of light, using the QPM and a simple biconvex lens. By our techniques one can measure the sign as well as the magnitude of the OAM states of the vortices.

Chapter 3

Physics of Photorefractive Nonlinearity

In 1966 at the Bell Laboratories, when researchers were studying the transmission of laser beams through Lithium Niobate crystal, it was found that crystal became "optically damaged" after irradiation by a laser beam. This turned out to be the spatial variation of index of refraction which caused a distortion in the wave-front and the effect is now known as photorefractive effect. Two years later scientists at the same laboratory found that these refractive index changes are of interest for applications in holographic data storage [7].

Since the first observation of the PR effect, this effect has been found in many electro-optic materials which includes lithium niobate ($LiNbO_3$), strontium barium niobate (SBN), barium titanate($BaTiO_3$), potassium niobate ($KNbO_3$), bismuth silicon oxide (BSO), bismuth germanium oxide (BGO), and gallium arsenide (GaAs). Apart from these inorganic materials, the PR effect is observed in organic materials also [69].

In addition to holographic data storage, PR materials also have applications in two-wave mixing, four-wave mixing, phase conjugation, ring resonator, optical interconnect, and neural network [7]. The PR materials can be used for slow as well as fast light generation [70].

In this chapter, we introduce the physics behind the PR nonlinearity. Section 1 describes the basics of PR effect. This effect is very well explained by a band transport model, which is discussed in Section 2. The isotropic and anisotropic approximations are also presented in the same section. Section 3 focuses on refractive index modulation in the PR media.

3.1 Basics of Photorefractive Effect

When PR material is exposed to light beam, free charge carriers are generated at the rate proportional to an input optical power. These charges move away from the high intensity region due to diffusion or drift or both, leaving behind the fixed charges of opposite sign. The free charge carriers are trapped by ionized impurities at other locations where intensity is low or zero, depositing their charge as they recombine. The result is the formation of a space charge field which modulates local refractive index via linear electro-optic effect or Pockels effect.

Total four basic processes are involved which cause the PR effect in a medium. These are 1) Photogeneration of charges, 2) Transportation of charges due to drift or diffusion 3) Trapping of charges and formation of space-charge field 4) Modulation of index of refraction via electro-optic effect.

3.2 Band Transport Model

Most of the observed properties (e.g. absorption, conductivity, charge carrier mobility) in a PR medium could be explained by a band transport model developed by Kukhtarev et al [7,71]. According to this model, in the PR material there exist impurities or imperfections. All donor impurities are assumed to be identical and have energy state middle of a bandgap as shown in Fig. 3.1. For simplicity, one can consider an electron as a sole charge carrier. When light illuminates on the PR material, the photons are absorbed by these impurities and photoionization takes place with the emission of electrons. Let N_D be the number density of donor with N_D^i being the ionized donor. The rate of photoionization is proportional to the light intensity I_t which is the sum of

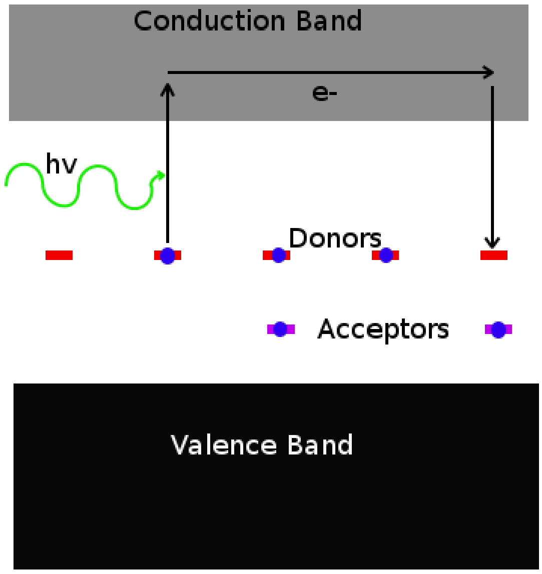

Figure 3.1: Band transport model.

light intensities illuminating the medium. The sum includes the intensity of input light beam I_{in}, the intensity I_b due to an uniform background light, and the dark intensity I_d due to a thermal effect.

$$I_t = I_{in} + I_b + I_d. \tag{3.1}$$

In all oxide and sillenite PR materials, I_d is very small i.e. of the order of mW/cm^2. As the dielectric relaxation time is inversely proportional to the sum of the optical and the dark intensity, the presence of this dark intensity without I_b causes very long response time in the PR media. Additional uniform illumination I_b not only increases the response of PR media but also provides an additional control over the PR nonlinearity. As $I_b \gg I_d$, Eq. (3.1) becomes

$$I_t \approx I_{in} + I_b. \tag{3.2}$$

The rate of generation of electron due to I_t is written as

$$G = s(I_{in} + I_b)(N_D - N_D^i), \tag{3.3}$$

where s is the cross section for photoexcitation. The electrons in a conduction band can move at some other place where intensity is low or zero and trapped by an ionized impurity. Their recombination rate depends on the electron number density N and ionized donor density N_D^i. Hence, the rate of recombination of electron is

$$R = \gamma N N_D^i. \tag{3.4}$$

Here, γ is the probability of recombination of electron and ion. Since ions are fixed but electrons can move in the conduction band, therefore, the rate of generation of ionized donor can be written as,

$$\frac{\partial N_D^i}{\partial t} = s(I_{in} + I_b)(N_D - N_D^i) - \gamma N N_D^i. \tag{3.5}$$

The electrons in conduction band can experience three different transport processes. These process are 1) Diffusion, 2) Drift due to the electric field E, and 3) Photovoltaic or photogalvanic field. Thus, the resulting current density is written as

$$\begin{aligned} J &= J_{drift} + J_{diff} + J_{pv}, \\ &= e\mu N E + \mu K_b T \nabla N + \beta_{ph}(N_D - N_D^i) e_c I_{in}, \end{aligned} \tag{3.6}$$

where e, μ, T and K_b are the elementary charge, mobility of electron, absolute temperature and Boltzmann constant respectively. e_c denotes the unit vector along the c-axis of the crystal. The input intensity of light beam is represented by I_{in}. β_{ph} is the photovoltaic tensor which represents the strength of photovoltaic field. This tensor has the largest component along the c-axis for $LiNbO_3$. Therefore, in this thesis work we have chosen polarization of the input light beam parallel to the c-axis, to utilize maximum value of β_{ph}. The c-axis of the crystal remains parallel to the y-axis, with the z-axis as the propagation direction of light beam in our coordinate system.

To maintain the charge neutrality, the acceptor impurities must be present in a PR medium. They are assumed to be ionized and denoted by N_A. The total space charge density can be written as

$$\rho = e(N_D^i - N - N_A). \tag{3.7}$$

Due to this space charge density, space charge field E_{sc} is formed inside the PR material. This space charge potential and field must satisfy Gauss law and continuity equation. Using Gauss law, one can write,

$$\nabla(\epsilon\epsilon_0 E_{sc}) = \rho = e(N_D^i - N - N_A), \tag{3.8}$$

and continuity equation takes form

$$\frac{\partial \rho}{\partial t} = -\nabla \cdot J. \tag{3.9}$$

The space charge field E_{sc}, responsible for change in refractive index in the PR media, can be calculated using two models - the isotropic model [72] and the anisotropic model [73]. These models are discussed below.

3.2.1 Isotropic Model

The isotropic model assumes that the change in index of refraction is symmetric to the propagation axis. Therefore, it is suitable for circularly symmetric solutions due to a symmetric nature of the change in index of refraction. This model is best suited for one dimensional (1D) beam propagation. In the two dimensional (2D) case, it shows results which are in good agreement with experimental results for short propagation distances only [74].

In this model, following approximation is used

$$N_D^i, N_A \gg N \tag{3.10}$$

From this approximation one can derive E_{sc} using equations of band transport model [26, 72],

$$E_{sc} = E_0 \frac{1}{1+I} - E_p \frac{I}{1+I} \tag{3.11}$$

where E_0 is the applied field, $E_p = \frac{\beta_{ph}\gamma N_A}{e\mu s}$ is the photovoltaic field and $I = I_{in}/I_b$ is the input intensity normalized by the intensity of background light.

3.2.2 Anisotropic Model

It requires considering an anisotropic model that takes into account nonlocal response specific to the PR media and could explain the results for 1D as well as 2D beam propagation at all distances [73, 75]. In the anisotropic model, the change in index of refraction is asymmetric. In the present thesis work, we have studied the propagation of engineered beams through an anisotropic PR media. As our aim is to study the effect of anisotropy on the propagation dynamics of these beams, we have used the anisotropic model to explain our experimental results.

At steady state, the model assumes that ionized acceptors are comparable with ionized donors i.e. $N_A = N_D^i$. With this assumption, Eq. (3.5) can be written as

$$N = \frac{sI_b}{\gamma N_A}(N_D - N_A)(1 + I). \tag{3.12}$$

The electric field E can be expressed in the terms of potential which consists of light induced space charge potential and potential due to applied electric field.

$$\begin{aligned} \phi_t &= \phi - E_0 y, \\ \nabla\phi_t &= \nabla\phi - E_0, \\ E &= E_{sc} + E_0. \end{aligned} \tag{3.13}$$

In above equations, we have applied the dc electric field externally along the y-axis i.e. the c-axis of the crystal. The choice of the c-axis is discussed in the next section.

Now consider continuity equation at steady state

$$\begin{aligned} \nabla \cdot J &= -e\mu\nabla \cdot (N\nabla\phi_t) + \mu K_b T \nabla \cdot \nabla N + \beta_{ph}(N_D - N_A)\nabla \cdot e_c I_{in}, \\ 0 &= -e\mu(N\nabla^2\phi_t + \nabla\phi_t \cdot \nabla N) + \mu K_b T \nabla^2 N + \beta_{ph}(N_D - N_A)\frac{\partial I_{in}}{\partial y}. \end{aligned} \tag{3.14}$$

Substituting Eq. (3.12) in Eq. (3.14), we obtain

$$\nabla^2\phi_t + \nabla\phi_t \cdot \nabla \ln(1 + I) = E_p \frac{\partial \ln(1 + I)}{\partial y} + \frac{K_b T}{e}\frac{\nabla^2(1 + I)}{I + I}. \tag{3.15}$$

Substituting Eq. (3.13) in Eq. (3.15), we get

$$\nabla^2\phi + \nabla\phi \cdot \nabla \ln(1 + I) = (E_0 + E_p)\frac{\partial \ln(1 + I)}{\partial y} + \frac{K_b T}{e}\frac{\nabla^2(1 + I)}{I + I}. \tag{3.16}$$

The last term in Eq. (3.16) is due to diffusion effect that is responsible for the spatial soliton bending [75]. One can neglect this term and write Eq. (3.16) as

$$\nabla^2\phi + \nabla\phi \cdot \nabla \ln(1+I) = (E_0 + E_p)\frac{\partial \ln(1+I)}{\partial y}. \tag{3.17}$$

We have used above equation i.e. Eq. (3.17) through out the thesis work. The finite difference method is used to solve Eq. (3.17) numerically. This method is discussed in Appendix B. Once, the space charge potential is known, one can calculate space charge field from the following expression,

$$E_{sc} = -\nabla\phi. \tag{3.18}$$

The space charge field modifies the index of refraction which is discuss in next section.

3.3 Change in Index of Refraction

There are certain materials in which index of refraction is modified by an electric field. This effect is called as electro-optic effect [6, 7, 76]. The change in refractive index depends on two ways,

- If the modified index of refraction is proportional to the strength of the applied electric field, then it is called as linear electro-optic effect or Pockels effect.

- If the index of refraction is modified in proportion to the square of the applied electric field, then it is called as quadratic electro-optic effect or Kerr effect.

The PR materials are electro-optic in nature. In these materials, a space charge field is generated in response to the input light beam, which alters the refractive index via linear electro-optic effect or Pockels effect. Traditionally, this linear electro-optic effect is written in terms of the change in impermeability tensor

$$\Delta\eta_{ij} = \Delta\left(\frac{1}{n^2}\right)_{ij} = r_{ijk}E_k, \tag{3.19}$$

where r_{ijk} is the linear electro-optic coefficient. E_k is the component of the electric field with $k = x, y, z$ and the summation over repeated indices is assumed.

Most of the PR crystals are anisotropic electro-optic crystals having tensorial nature of ϵ. The rank of this tensor is two and it is written in principal coordinates as

$$\epsilon = \begin{pmatrix} \epsilon_x & 0 & 0 \\ 0 & \epsilon_y & 0 \\ 0 & 0 & \epsilon_z \end{pmatrix} = \epsilon_0 \begin{pmatrix} n_x^2 & 0 & 0 \\ 0 & n_y^2 & 0 \\ 0 & 0 & n_z^2 \end{pmatrix},$$

where ϵ_x, ϵ_y, ϵ_z represent the principal dielectric constants, and n_x, n_y, n_z are the principal indices of refraction. When any two principal indices of refraction of the crystal are equal then it is called as uniaxial crystal. However, if all principal indices of refraction are different, then it is termed as biaxial crystal. The uniaxial crystal has one optic axis whereas biaxial has two optic axes. When light travels along this axis, there is no change in its polarization. For the crystal having tetragonal and hexagonal symmetry, the optic axis coincides to the c-axis of the crystal. We have used lithium niobate ($LiNbO_3$) and strontium barium niobate (SBN) crystal in our work, both are uniaxial in nature with hexagonal symmetry.

The electro-optic tensor for SBN and $LiNbO_3$ in contracted notation is written as

$$r_{\mathrm{SBN}} = \begin{pmatrix} 0 & 0 & r_{13} \\ 0 & 0 & r_{13} \\ 0 & 0 & r_{33} \\ 0 & r_{42} & 0 \\ r_{42} & 0 & 0 \\ 0 & 0 & 0 \end{pmatrix}, r_{\mathrm{LiNbO_3}} = \begin{pmatrix} 0 & -r_{22} & r_{13} \\ 0 & r_{22} & r_{13} \\ 0 & 0 & r_{33} \\ 0 & r_{51} & 0 \\ r_{51} & 0 & 0 \\ -r_{22} & 0 & 0 \end{pmatrix}.$$

An input light with polarization perpendicular and parallel to the c-axis, is termed as an ordinary and extraordinary polarized respectively. The nonlinear change in index of refraction in both the crystals, for the ordinary polarized and the extraordinary polarized light beams, is obtained from Eq. (3.19) and written as

$$\begin{aligned} \Delta n_o &= -\frac{1}{2} n_o^3 r_{13} E_{sc}, \\ \Delta n_e &= -\frac{1}{2} n_e^3 r_{33} E_{sc}. \end{aligned} \tag{3.20}$$

In both the crystals, $r_{33} \gg r_{13}$, therefore we have chosen polarization of an input beam and applied field along the c-axis of the crystal through out the thesis. The sign of E_{sc} decides the presence of self-focusing or self-defocusing nonlinearity in the crystal. Advantage of using external potential is that the sign of E_{sc} can be controlled by changing the polarity of applied field. In SBN, there is no photovoltaic field therefore it is easy to control the nonlinearity by applying a field. However, one has to cancel photovoltaic field in case of $LiNbO_3$. It should be noted that when external field is absent, $LiNbO_3$ shows defocusing nonlinearity only.

Chapter 4

Propagation Dynamics of Diffraction Broadened Beams

We have divided the beams engineered by us into two categories: the beams which do not diffract while propagation in linear medium i.e. non-diffracting beams and the beams which show diffraction under the same condition. The evolution of non-diffracting beams will be considered in the next chapter. In this chapter, we have studied propagation dynamics of diffraction broadened beams which include HG beams, LG beams, ring lattice beams, dipole and quadrupole vortex beams. These beams are produced using computer-generated holography technique as discussed in Chapter 2. The numerical model described in Chapter 3, Appendix A and B have been used to compare experimental results for their propagation dynamics in the PR media. The evolution of dipole and quadrupole vortex beams in free space have been examined experimentally along with their evolution through an analytical expression derived by us. The dipole itself and pair of dipoles in the quadrupole, annihilate to form crescent kind structure. We have used the Poynting vector to study the flow of energy in the dipole and quadrupole vortices as they propagate. The evolution of these beams in a photovoltaic PR medium have also been studied. It is observed that they form a stable dipole or quadrupole structure in the PR medium with defocusing nonlinearity unlike their free space propagation. We have used a $LiNbO_3$ crystal as our PR medium for all the experiments mentioned in this chapter. The experimental results are verified with the numerical simulations.

Since the propagation dynamics of the HG and LG beams are well known in free space or in a linear medium, we have studied their spatial evolution through a photovoltaic PR medium. A dark stripe beam is generated by using HG modes to study its propagation dynamics. Instead of forming dark soliton, the dark stripe undergoes through instability in a $LiNbO_3$. We have produced beams with dark rings using LG modes and studied their propagation through the $LiNbO_3$. We observe that the dark rings, instead of forming dark ring solitons, break into vortex-antivortex pairs, forming quadrupoles. The experimental results could be taken as a consequence of modulational instability during beam propagation that is revealed through our numerical analysis.

We generate experimentally optical ring lattice structures which are the superposition of two coaxial LG modes with common waist position and waist parameter. Some of these beams have rotational dynamics. It is observed that this dynamics depends on the indices of LG beams which superpose to generate these structures. We have examined their dynamics through a defocusing PR medium. It is found that the lattice beams with rotational dynamics can convert their edge dislocation into a screw dislocation while propagating through the PR medium. The beams which do not have rotational dynamics undergo defocusing.

In Section 1, we discus about the dipole and quadrupole vortex beams along with their spatial evolution in free space and through a defocusing PR medium. The analytical expression to study free space propagation for these beams has been derived in the same section. The evolution of dark stripe beams generated through HG modes is described in Section 2. In Section 3, we focus on the nonlinear dynamics of dark ring beams generated from the LG beams. The rotational dynamics of the ring lattice beams in free space and through the PR medium are presented in Section 4.

4.1 Dipole and Quadrupole Vortex Beams

The optical vortex is the singularity in a light field having phase variation from 0 to $2\pi l$ (l is the topological charge) within the period of λ (λ is the wavelength of light) [32]. This singularity can be embedded in a Gaussian beam using a phase mask. The evolved light beam has helical wavefront that causes orbital angular momentum to this beam [33]. The helical wavefront is twisted in a clock-wise or an anticlockwise sense which is decided by the sign of vortex i.e. sign of the topological charge. The unique behavior of the vortex results in a variety of its applications in the fields of optical tweezing [34], optical communication [35], as well as in quantum information [36].

The nonlinear dynamics of optical vortex through the PR media is well studied. It is observed that the vortex beam with high topological charge decays into unit charges in the PR media with defocusing nonlinearity [77, 78]. The time evolution of the optical vortex shows charge-dependent stretching and rotation in the PR medium [79]. The propagation of the optical vortex in lithium niobate is also influenced by the propagation direction and the polarization of the input beam [80].

One can incorporate a number of vortices in a single host beam to study their dynamics [81–87]. Indebetouw [81] have theoretically investigated the propagation dynamics of an array of vortices embedded in a Gaussian beam. The opposite charges annihilate each other whereas same charge vortices just rotate around the axis of beam. A pair of two oppositely charge vortices embedded in the Gaussian host beam form an optical vortex dipole. The propagation of such a vortex dipole have been studied in both linear [81–86] and nonlinear media [87]. In the linear media, the vortices of dipole annihilate each other during the propagation. This leads to the formation of crescent like structure. However, they remain separated depending upon the strength of nonlinearity in a defocusing PR medium [87]. This is true only if the line joining the two vortices in the dipole is perpendicular to the applied field which induces nonlinearity. Otherwise they follow the dynamics similar to the linear regime.

For a quadrupole, each vortex has nearest neighbor with opposite sign of the topological charge, thus having dipole distribution in the transverse directions. Such a quadrupole can be generated by a linearly polarized Gaussian beam propagating along the optic axis or the c-axis of the uniaxial crystal [88, 89] or through the computer-generated holography technique.

It is observed that the stable dipoles are formed when dark stripe undergoes to snake instability in the PR media [90, 91]. It is also found recently that the dark rings generated from LG modes form quadrupole vortex while propagating through the PR media [92]. These results suggest that the dipole and quadrupole may be the solution of nonlinear paraxial wave equation with PR nonlinearity.

In this work we have studied propagation of quadrupole and dipole vortices in free space as well as through a photovoltaic PR medium. We generate these vortex beams using computer generated hologram (CGH). The dipole and the quadrupole vortices are observed to be unstable in free space and form crescent kind of structures. We have verified our experimental results with theoretical results from exact analytical expression. The energy flow during propagation of these beams are plotted by using Poynting vector.

To study their nonlinear propagation dynamics we have used a $LiNbO_3$ crystal as a PR medium. In the linear regime, the dipole and the quadrupole vortices are observed to be unstable. However, we have observed that they become stable in the PR crystal for a particular orientation of the dipole or quadrupole in an input Gaussian host beam. It is seen that the formation of stable dipole as well as quadrupole in the nonlinear medium is decided by the formation of crescent structure in its linear counterpart.

4.1.1 Linear Dynamics

Theory

The optical dipole with the vortices separated by a distance "a" from beam axis has complex field amplitude at $z = 0$

$$A_0(x_1, y_1) = \left(\frac{x_1 + a + iy_1}{w_0}\right)\left(\frac{x_1 - a - iy_1}{w_0}\right)\exp[-\frac{(x_1^2 + y_1^2)}{w_0^2}], \tag{4.1}$$

where w_0 is the beam radius of Gaussian host beam at $z = 0$. After simplification one can write above equation as

$$A_0(x_1, y_1) = \left(\frac{x_1^2 + (y_1 - ia)^2}{w_0^2}\right) \exp[-\frac{(x_1^2 + y_1^2)}{w_0^2}]. \tag{4.2}$$

The field distribution at a distance $z = L$ from the $z = 0$ can be calculated using Fresnel diffraction integral (Eq. (1.35)),

$$\begin{aligned} A(x_2, y_2) &= \frac{k}{i2\pi L}\exp[\frac{ik}{2L}(2L^2 + x_2^2 + y_2^2)] \iint A_0(x_1, y_1) \\ &\times \exp[\frac{ik}{2L}((x_1^2 + y_1^2) - 2(x_1x_2 + y_1y_2))]dx_1dy_1. \end{aligned} \tag{4.3}$$

After substituting Eq. (4.2) in Eq. (4.3), we get

$$A(x_2, y_2) = \frac{k}{i2\pi L w_0^2}\exp[\frac{ik}{2L}(2L^2 + x_2^2 + y_2^2)](I_a + I_b), \tag{4.4}$$

where

$$\begin{aligned} I_a &= \int x_1^2 \exp[-\frac{x_1^2}{w_0^2} + \frac{ik}{2L}x_1^2 - \frac{ik}{L}x_1x_2]dx_1 \\ &\times \int \exp[-\frac{y_1^2}{w_0^2} + \frac{ik}{2L}y_1^2 - \frac{ik}{L}y_1y_2]dy_1, \\ I_b &= \int \exp[-\frac{x_1^2}{w_0^2} + \frac{ik}{2L}x_1^2 - \frac{ik}{L}x_1x_2]dx_1 \\ &\times \int (y_1 - ia)^2 \exp[-\frac{y_1^2}{w_0^2} + \frac{ik}{2L}y_1^2 - \frac{ik}{L}y_1y_2]dy_1. \end{aligned} \tag{4.5}$$

Using standard integral (Eq. (2.24)), we get

$$\begin{aligned} I_a &= -\frac{d^3\sqrt{\pi}}{4}H_2[\frac{kdx_2}{2L}]\exp[-(\frac{kd}{2L})^2(x_2^2 + y_2^2)]. \\ I_b &= -\frac{d^3\sqrt{\pi}}{4}H_2[\frac{a}{d} + \frac{kdx_2}{2L}]\exp[-(\frac{kd}{2L})^2(x_2^2 + y_2^2)], \end{aligned} \tag{4.6}$$

where

$$d = \frac{w_0}{\sqrt{1 - i\frac{kw_0^2}{2L}}}.$$

Substituting Eqs. (4.6) in Eq. (4.4), we obtain

$$\begin{aligned} A(x_2, y_2, L) &= \frac{ikd^3}{8\pi L w_0^2}\exp[ikL + \frac{k}{2R}(x_2^2 + y_2^2)]\exp[-\frac{x_2 + y_2}{w^2}] \\ &\times \left(H_2[\frac{kdx_2}{2L}] + H_2[\frac{a}{d} + \frac{kdy_2}{2L}]\right), \end{aligned} \tag{4.7}$$

where

$$R = L + \frac{z_r^2}{L}, w = w_0\sqrt{1+(\frac{L}{z_r})^2}, z_r = \frac{kw_0^2}{2}.$$

In above equations, H_n is the Hermite polynomial of order n. w and R are the beam radius and the radius of curvature respectively which represent the Gaussian beam parameters. The propagation dynamics of dipole vortex in free space can be calculated by using (Eq. (4.7)) which is the mathematical expression for dipole vortex. The last term in the parentheses contains dipole vortex field with the Guoy phase whereas remaining terms belong to the Gaussian beam field.

The quadrupole with the vortices separated from each other by a distance "$2a$" has complex field amplitude at $z = 0$

$$\begin{aligned} A_0(x_1, y_1) &= ((x_1+a)+i(y_1+a))((x_1-a)+i(y_1-a))((x_1-a)-i(y_1+a)) \\ &\quad \times((x_1+a)-i(y_1-a))\frac{\exp[-\frac{(x_1^2+y_1^2)}{w_0^2}]}{w_0^4}. \\ &= \left((x_1^4+2x_1^2y_1^2+y_1^4)-2a^2i(x_1^2-y_1^2)-4a^4\right)\frac{\exp[-\frac{(x_1^2+y_1^2)}{w_0^2}]}{w_0^4}. \end{aligned} \quad (4.8)$$

After substituting Eq. (4.8) in Eq. (4.3), we get

$$\begin{aligned} A(x_2, y_2) &= \frac{k}{i2\pi Lw_0^4}\exp[\frac{ik}{2L}(2L^2+x_2^2+y_2^2)] \\ &\quad \times(I_1+2I_2+I_3-2a^2i(I_a-I_4)-4a^4I_5), \end{aligned} \quad (4.9)$$

where

$$\begin{aligned} I_1 &= \int x_1^4\exp[-\frac{x_1^2}{w_0^2}+\frac{ik}{2L}x_1^2-\frac{ik}{L}x_1x_2]dx_1\int\exp[-\frac{y_1^2}{w_0^2}+\frac{ik}{2L}y_1^2-\frac{ik}{L}y_1y_2]dy_1, \\ I_2 &= \int x_1^2\exp[-\frac{x_1^2}{w_0^2}+\frac{ik}{2L}x_1^2-\frac{ik}{L}x_1x_2]dx_1\int y_1^2\exp[-\frac{y_1^2}{w_0^2}+\frac{ik}{2L}y_1^2-\frac{ik}{L}y_1y_2]dy_1, \\ I_3 &= \int\exp[-\frac{x_1^2}{w_0^2}+\frac{ik}{2L}x_1^2-\frac{ik}{L}x_1x_2]dx_1\int y_1^4\exp[-\frac{y_1^2}{w_0^2}+\frac{ik}{2L}y_1^2-\frac{ik}{L}y_1y_2]dy_1, \\ I_4 &= \int\exp[-\frac{x_1^2}{w_0^2}+\frac{ik}{2L}x_1^2-\frac{ik}{L}x_1x_2]dx_1\int y_1^2\exp[-\frac{y_1^2}{w_0^2}+\frac{ik}{2L}y_1^2-\frac{ik}{L}y_1y_2]dy_1, \\ I_5 &= \int\exp[-\frac{x_1^2}{w_0^2}+\frac{ik}{2L}x_1^2-\frac{ik}{L}x_1x_2]dx_1\int\exp[-\frac{y_1^2}{w_0^2}+\frac{ik}{2L}y_1^2-\frac{ik}{L}y_1y_2]dy_1. \end{aligned} \quad (4.10)$$

Using standard integral (Eq. (2.24)), we obtain

$$\begin{aligned}
I_1 &= -\frac{d^6\pi}{2^4}H_4[\frac{kdx_2}{2L}]\exp[-(\frac{kd}{2L})^2(x_2^2+y_2^2)],\\
I_2 &= -\frac{d^6\pi}{2^4}H_2[\frac{kdx_2}{2L}]H_2[\frac{kdy_2}{2L}]\exp[-(\frac{kd}{2L})^2(x_2^2+y_2^2)],\\
I_3 &= -\frac{d^6\pi}{2^4}H_2[\frac{kdy_2}{2L}]\exp[-(\frac{kd}{2L})^2(x_2^2+y_2^2)],\\
I_4 &= -\frac{d^3\sqrt{\pi}}{4}H_2[\frac{kdy_2}{2L}]\exp[-(\frac{kd}{2L})^2(x_2^2+y_2^2)],\\
I_5 &= -\frac{d^6\pi}{2^4}\exp[-(\frac{kd}{2L})^2(x_2^2+y_2^2)]. \qquad (4.11)
\end{aligned}$$

Substituting Eqs. (4.11) in Eq. (4.9), we obtain

$$\begin{aligned}
A(x_2,y_2) &= \frac{-ik}{2Lw_0^4}\exp[ikL+\frac{k}{2R}(x_2^2+y_2^2)]\exp[-\frac{x_2+y_2}{w^2}]\\
&\times(\frac{d^6}{2^4}(H_4[\frac{kdx_2}{2L}]+H_4[\frac{kdy_2}{2L}]+2H_2[\frac{kdx_2}{2L}]H_2[\frac{kdy_2}{2L}])\\
&+ia^2d^4(H_2[\frac{kdx_2}{2L}]-H_2[\frac{kdy_2}{2L}])-4d^2a^4). \qquad (4.12)
\end{aligned}$$

This is an expression for the quadrupole vortex. The propagation dynamics of quadrupole vortex in free space can be calculated by this expression. Again the last term in the parentheses contains quadrupole field with the Guoy phase whereas remaining terms stand for a Gaussian beam field in Eq. (4.12).

The formation of crescent structures in dipole and quadrupole can be understood by monitoring energy flow of the field during propagation. The Poynting vector indicating the energy flow of the optical field is defined as [47]

$$\mathbf{S}=\mathbf{S_z}+\mathbf{S}_\perp=\frac{1}{2\eta_0}[|u|^2\hat{z}+\frac{i}{2k}[u\nabla_\perp u^*-u^*\nabla_\perp u]], \qquad (4.13)$$

where $\eta_0=\sqrt{\mu_0/\epsilon_0}$ is the impedance of free space. $\mathbf{S_z}$ and $\mathbf{S}_\perp$ are the longitudinal and transverse components of the Poynting vector.

Experiment

Figure 4.1 shows the experimental setup. We generate CGHs for the dipole and the quadrupole vortex beams with different configuration of vortices. The CGHs are sent to an SLM interfaced with computer. We have used an intensity stabilized He-Ne laser (Spectra-Physics, Model 117A) having wavelength 632.8

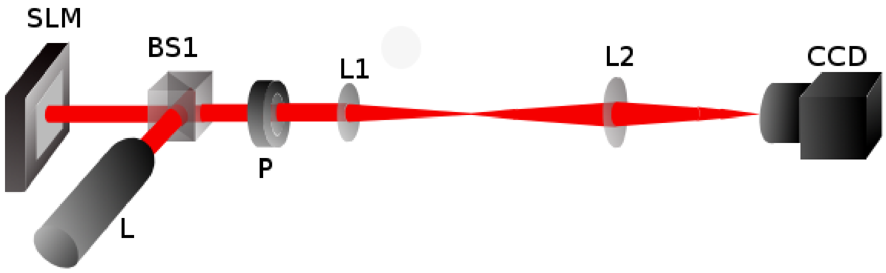

Figure 4.1: Experimental Setup. L, laser; BS1, beam-splitter; SLM, spatial light modulator; P, Polarizer; L1, Fourier lens; L2, imaging lens; and CCD, camera.

nm. After illuminating the SLM with laser, the desired beam is generated in the first diffracted order. As this beam propagates in free space, the opposite charges annihilate each other to form a crescent at the far field. We use Fourier transform property of a lens (focal length f = 50 cm) to generate dipole or quadrupole at the focus from this crescent structure. We assume this focus point as the $z = 0$. The waist size of Gaussian beam at this focus point is 0.15 mm. The CCD camera (MediaCybernetics, Evolution VF cooled Color Camera) and imaging lens is used to grab the images at different propagation distances.

Results and Discussion

Let us consider the propagation of dipole vortex beam in free space. The vortices of dipole are separated from the beam axis by a distance of $w_0/2$ i.e. $a = w_0/2$. The experimental intensity distributions at different propagation distances are shown in Fig 4.2. At $z = 0$ cm, the dipole has two vortices of opposite sign. As the beam propagates, both the vortex cores undergo a natural diffraction as seen at $z = 5$ cm. Consequently, both vortices come closer to each other and annihilate that leads to a dark region sandwiched between the two bright lobes. At $z = 15$ cm, the dark region forms a crescent structure.

To explain the formation of crescent from the dipole vortex beam, we have plotted theoretical intensity profiles at different propagation distances using

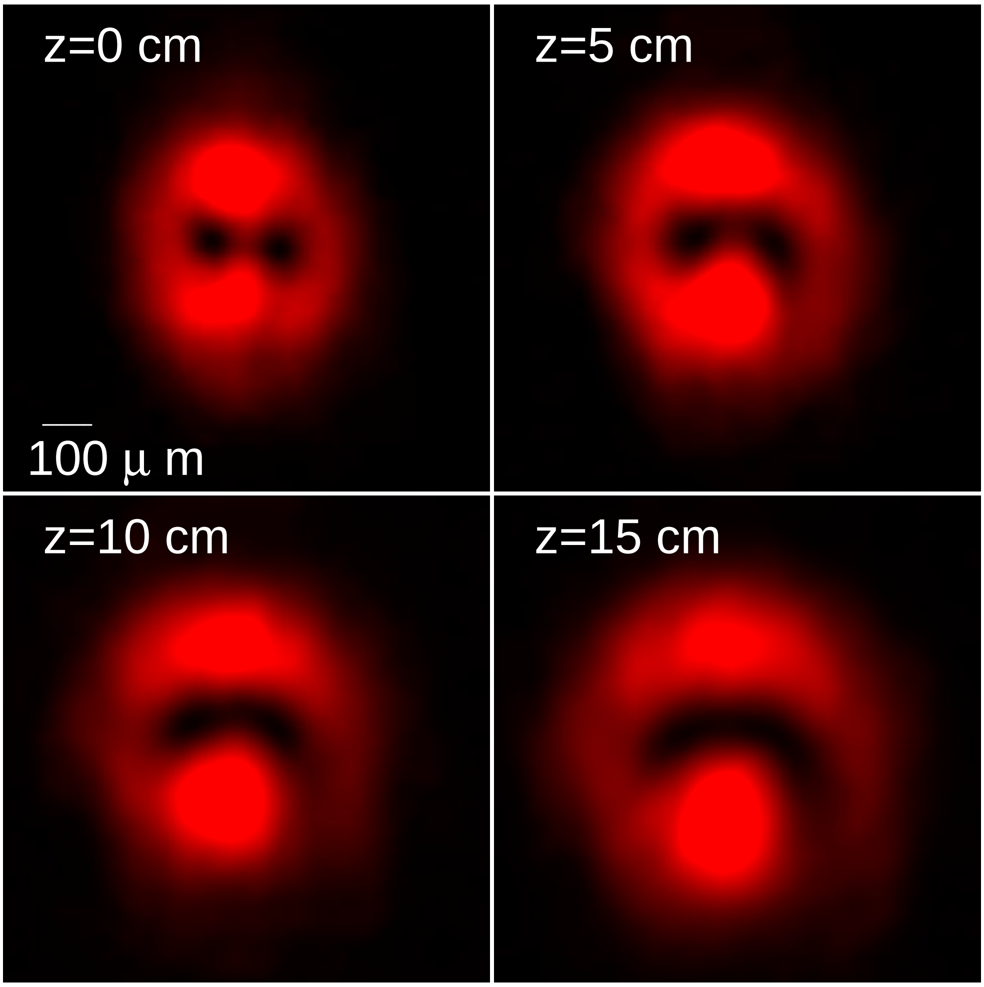

Figure 4.2: Experimental propagation dynamics of dipole vortex.

Eq. (4.7) in Fig. 4.3. The arrows in figure are Poynting vectors which represent flow of energy. At $z = 0$ cm, Poynting vectors curl around the center of the vortices. This implies that left vortex rotates in an anticlockwise sense whereas right has a clockwise sense of rotation. Due to this rotation, the energy of the system moves away from the center and creates an expanded region of darkness as the beam propagates that can be seen in Fig. 4.3 at $z = 10$ cm. This darkness forms a crescent structure.

The similar measurements have been done by reversing the sign of vortices in dipole. One can do this by taking complex conjugate of the Eq. (4.1). Here, left vortex rotates in a clockwise sense whereas right has an anticlockwise sense of rotation. This is exactly opposite to the previous case. Therefore, the crescent structure is formed at upper side instead of lower side in a free space

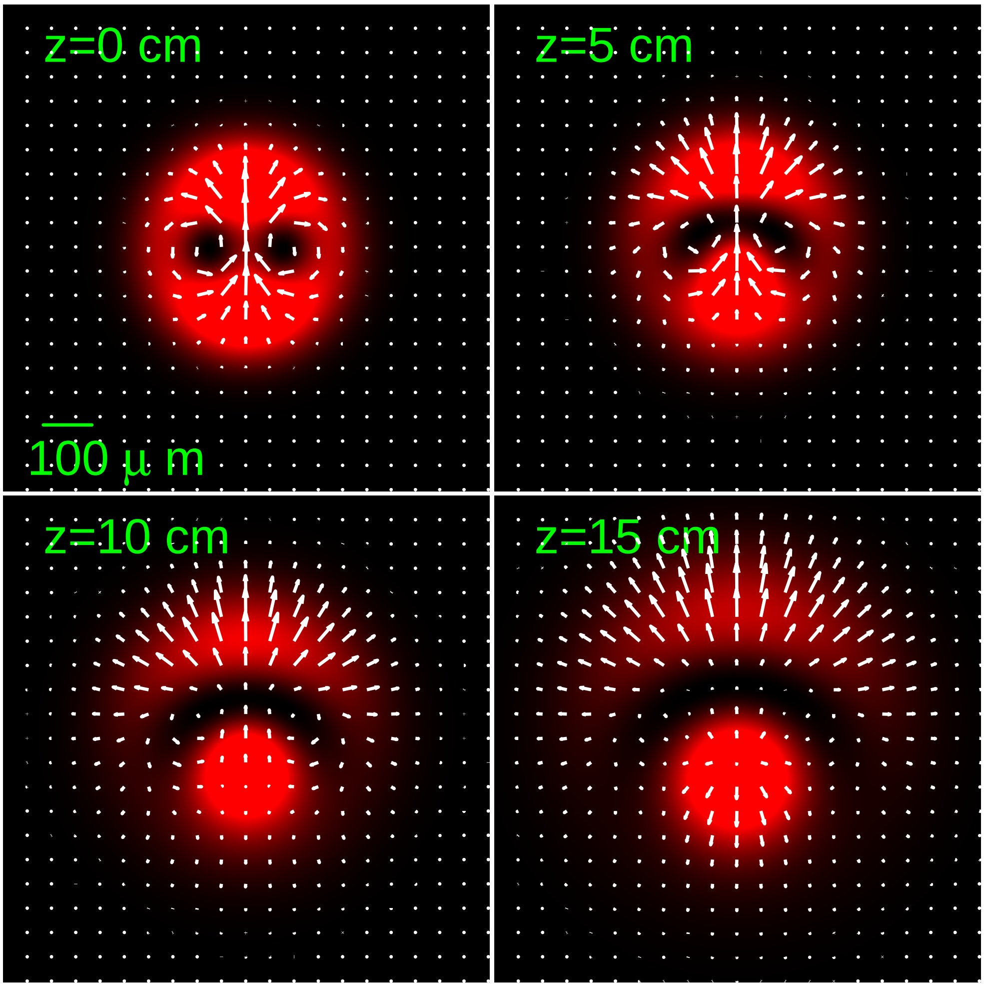

Figure 4.3: Theoretical propagation dynamics of dipole vortex.

propagation.

Now consider the case of quadrupole vortex. Any vortex in this system is separated from its nearest neighbor by a distance of w_0. The experimental results on the propagation dynamics of this quadrupole are shown in Fig. 4.4. The quadrupole shown at distance z=0 cm, undergoes to diffraction as it propagates. At distance z=5 cm, the vortices belonging to the first and the second quadrant as well as the vortices belonging to the third and the fourth quadrant approach each other. This leads to the annihilation of these vortices to form two crescents on the lower and the upper side as shown at distance z=15 cm.

The theoretical intensity profiles plotted from analytical expression for quadrupole with Poynting vectors are shown in Fig. 4.5. The energy of the

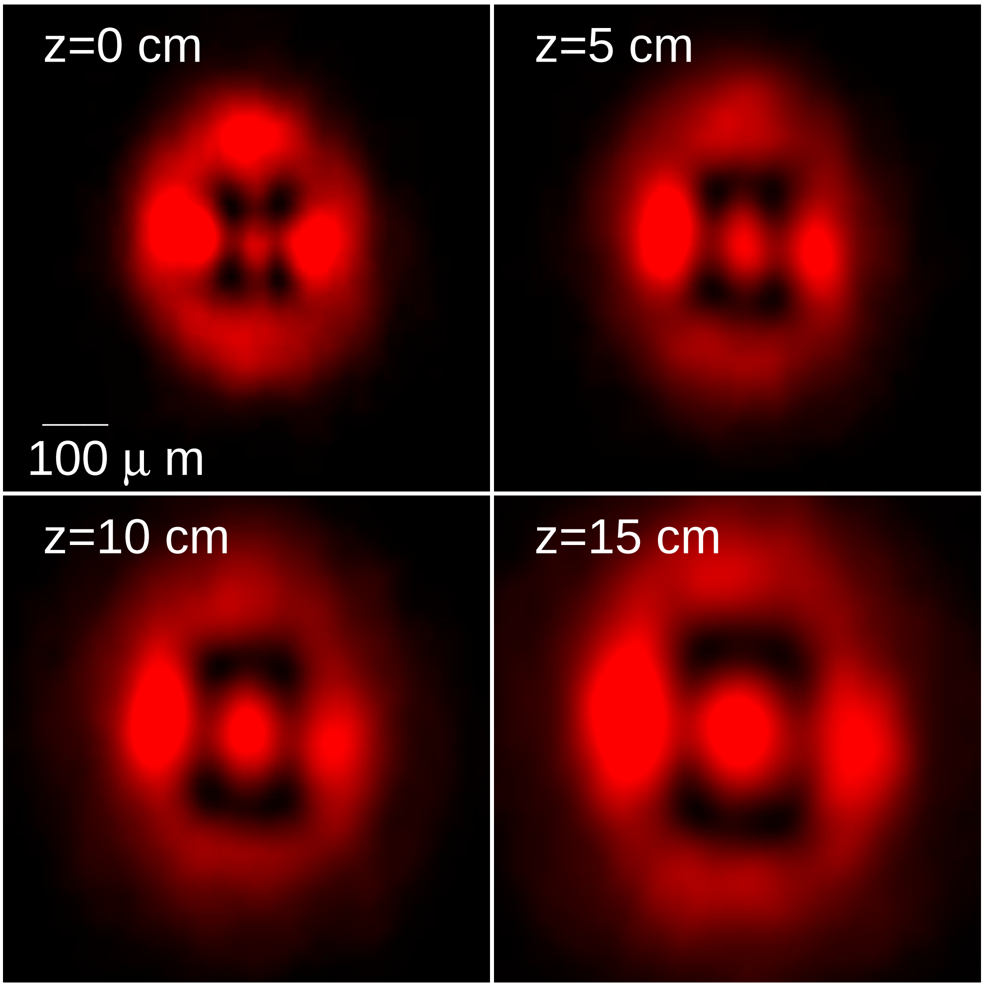

Figure 4.4: Experimental propagation dynamics of quadrupole vortex.

vortices in the first and the third quadrant curl around the center of vortex in a clockwise sense, whereas in an anticlockwise sense for the vortices in the second and the fourth quadrant. As the beam propagates, energy concentrates along the x-axis at the center, lower and upper borders of the beam as seen at z =5 cm. At z=10 cm, this creates darkness at the sandwiched regions between the center, lower and upper border of the beam. These regions of darkness form two crescents as seen at z=15 cm.

We also study the case in which the quadrupole shown in Fig. 4.4 are rotated by 90°. This is equivalent to inversion of the sign of vortices, which can be done by taking complex conjugate of the Eq. (4.8). In this case, the vortices in the first and the third quadrant rotate in an anticlockwise sense, whereas the vortices in the second and the fourth quadrant rotate in a clockwise sense.

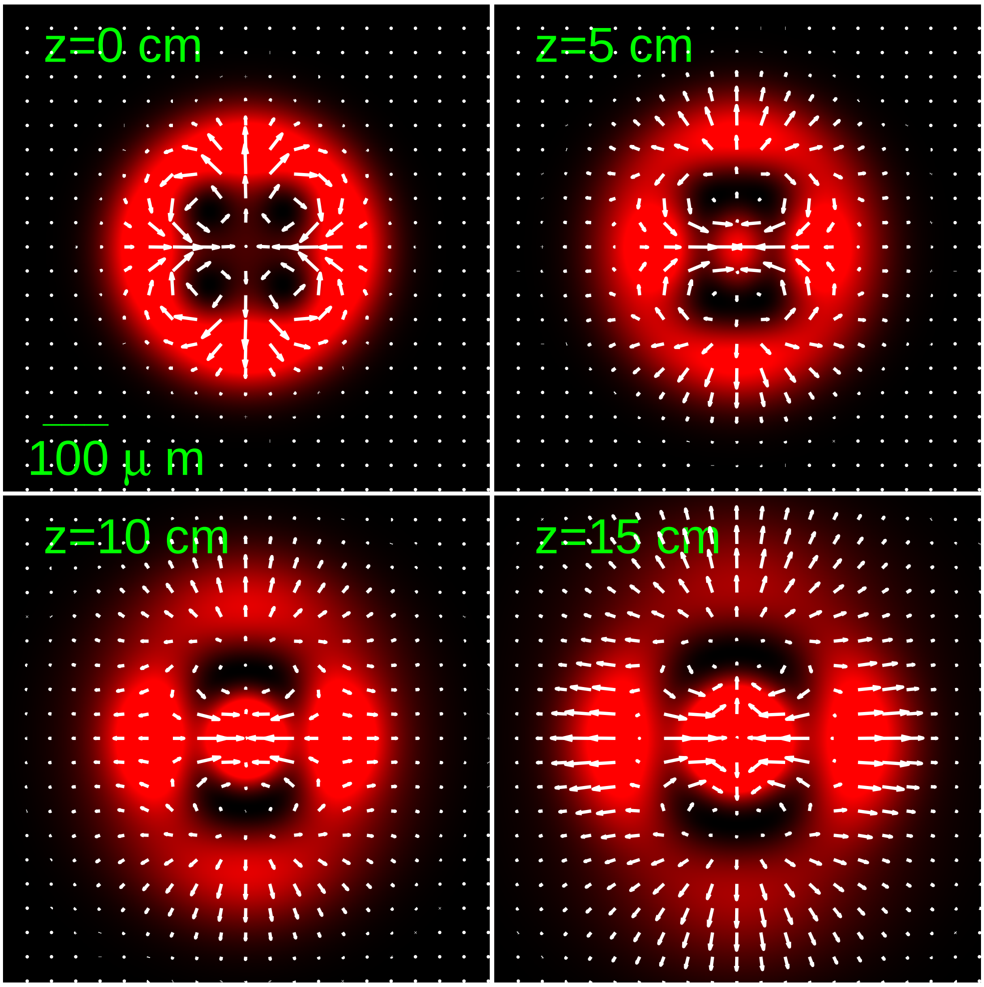

Figure 4.5: Theoretical propagation dynamics of quadrupole vortex.

Therefore, the crescent structure is generated at left and right sides instead of upper and lower sides. Since each vortex of the quadrupole has its nearest neighbor with opposite sign, vortex can annihilate with any one of its neighbor. However, the above results show that the annihilation of vortices take place according to the flow of energy.

Conclusion

In conclusion, we have studied the propagation dynamics of vortex dipole and quadrupole in free space. It is observed, both theoretically as well as experimentally, that dipole and quadrupole annihilate to form crescents while propagating. This annihilation can be explained by analyzing the flow of energy obtained with the help of Poynting vector. Our results show that the annihilation of vortices is governed by internal flow of energy associated with the individual vortex.

4.1.2 Nonlinear Dynamics

Numerical Model

We have already discussed about numerical model for beam propagation through the PR media in the last chapter. Here, we again briefly introduce it for completeness.

The spatial evolution of optical beam with field distribution $A(x, y)$ inside the PR medium can be calculated by solving the nonlinear PWE in normalized form (Eq. 1.17),

$$\frac{\partial A(x,y)}{\partial z} = \frac{i}{2}\nabla^2 A(x,y) + in_0 k_0^2 w_0^2 \Delta n A(x,y), \tag{4.14}$$

where Δn is the change in index of refraction, written as

$$\Delta n = \frac{1}{2} n_0^3 r_{eff} \frac{\partial \phi}{\partial y}. \tag{4.15}$$

Here, k_0 is the wave number of light in free space and w_0 is the beam waist size. n_0 and r_{eff} are the refractive index in the absence of light and the effective electro-optic coefficient of the PR material respectively. The transverse coordinates x, y are scaled by w_0 whereas the propagation coordinate z is scaled by the diffraction length $k_0 n_0 w_0^2$. The space charge potential ϕ can be calculated by using following potential equation (Eq. 3.17)

$$\nabla^2\phi + \nabla\phi\nabla[ln(1+I)] = (E_0 + E_p)\frac{\partial ln(1+I)}{\partial y}. \tag{4.16}$$

In the above equation, E_p is the photovoltaic field and I is the intensity of input beam, which is normalized by the background illumination. We have kept applied electric field E_0 equal to zero throughout the present chapter. We have used $LiNbO_3$ crystal in all experiments mentioned in this chapter. For $LiNbO_3$, $n_0 = 2.2$, r_{eff}=32 pV/m, and E_p =-27 kV/cm. Equations (4.14) and (4.16) are solved by the split-step Fourier transform method and the finite difference method which are explained in the Appendix A and B respectively.

Experiment

Figure 4.6 shows the experimental setup. The generation of dipole and quadrupole vortex beams are similar to the free space. The $LiNbO_3$ crystal (20 x 20 x 20 mm, 0.1% Fe-doped) is placed at the focus of the lens. The CCD camera (MediaCybernetics, Evolution VF cooled Color Camera) and imaging lens are used to grab the images at the back surface of the crystal. The extra beam

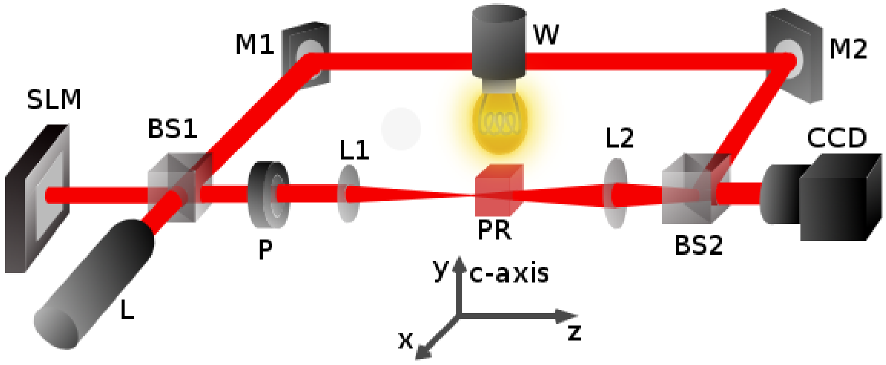

Figure 4.6: Experimental Setup. L, laser; BS1, BS2, beam-splitter; SLM, spatial light modulator; P, Polarizer; L1, Fourier lens; L2, imaging lens; M1, M2, mirror; PR, photorefractive crystal; W, white light source and CCD, camera.

from mirror is used for an interferometry. The polarization of the input light beam is kept along the c-axis of the crystal using a polarizer. This configuration induces a photovoltaic current and field along the c-axis. A white light source is used for background illumination.

Results and Discussion

We first propagate a dipole vortex beam through the PR crystal. Consider the case in which the line joining a pair of vortices is along the x-axis. The complex field distribution of such a dipole at the input of PR medium is given by

$$A(x, y, z = 0) = \sqrt{I_m}(x + 0.5 + iy)(x - 0.5 - iy)\exp[-(x^2 + y^2)], \quad (4.17)$$

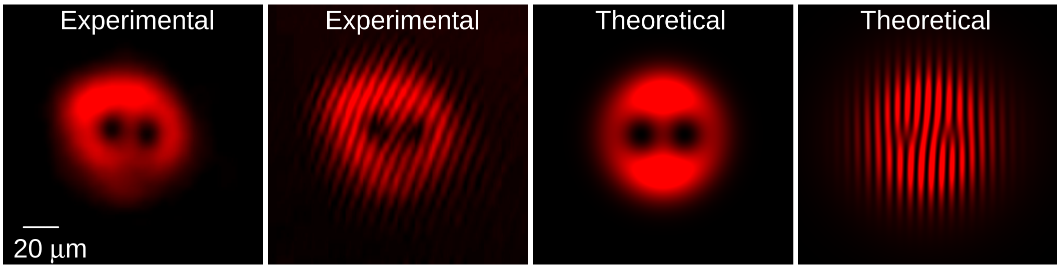

Figure 4.7: Input intensity profiles of dipole with line joining the pair oriented along the x-axis (first and third column) and corresponding interferograms (second and fourth column).

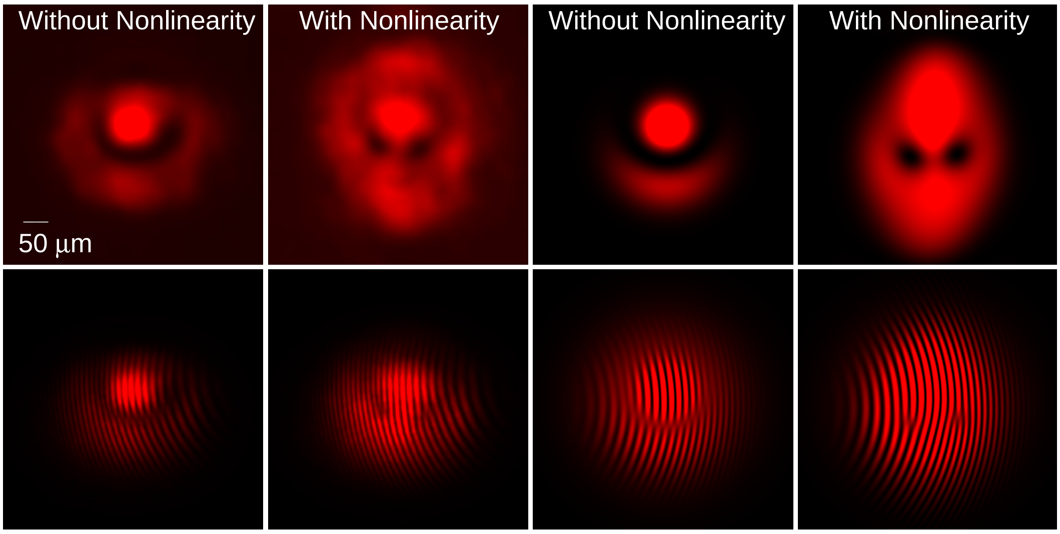

Figure 4.8: Experimental (first and second column) and numerical (third and fourth column) intensity profiles at back surface of the crystal for the dipole shown in Fig. 4.7 as an input beam (first row) and corresponding interferograms (second row).

where I_m is the normalized peak intensity having value 0.5 in our experiments. The vortices of dipole are separated by a normalized distance of unit beam waist. By interfering the field given by Eq. (4.17) with tilted plane wave, we have generated CGH that produces the dipole. The experimental and the theoretical intensity distributions produced at the input of the crystal are shown in Fig. 4.7 along with their interferograms.

Figure 4.8 shows the experimental and the numerical results for the propagation of above mentioned dipole through a PR medium, at the back surface of the crystal. In the absence of nonlinearity, left vortex rotates in a clockwise sense whereas right with an anticlockwise sense of rotation. Because of this, both vortices come closer to each other and annihilate that creates a dark region sandwiched between two bright lobes. The dark region has a crescent kind of structure. The interference pattern shows that the two bright lobes have a phase shift of π. There is no indication for the presence of vortex. As the dipole propagates inside the crystal, it generates space charge field which increases the nonlinearity of the crystal with time. At steady state, this nonlinearity forces the crescent to form two separate vortices with opposite sign. The presence of vortices are confirmed through the fork pattern observed in the interferograms shown in Fig. 4.8. The experimental results are in good agreement with the numerical results.

We also make measurements by reversing the sign of vortices in a dipole. One can do this by taking complex conjugate of the Eq. (4.17). Here, left vortex rotates in an anticlockwise sense whereas right has a clockwise sense of rotation. This is exactly opposite to the previous case. Therefore, the crescent structure is formed at upper side instead of lower side in the absence of nonlinearity. Once again two vortices are formed in the presence of nonlinearity at the steady state.

We have studied propagation of a dipole in which line joining a pair of vortices is along the y-axis as well. The complex field distribution of such a dipole at the input of PR medium can be written as,

$$A(x, y, z = 0) = \sqrt{I_m}(x + i(y + 0.5))(x - i(y - 0.5))\exp[-(x^2 + y^2)]. \quad (4.18)$$

Figure 4.9 shows experimental and theoretical intensity distributions at the input of the crystal along with their interferograms. The corresponding experimental and numerical intensity profiles with interferograms at the back surface of the crystal are shown in Fig. 4.10. The pair of charges annihilate and form crescent structure when the nonlinearity is absent. This structure undergoes self-defocusing in the presence of nonlinearity. However, the charges instead of remaining separated lose their sign unlike the previous case. This is confirmed by interferograms shown in Fig. 4.10. The interferogram shows π

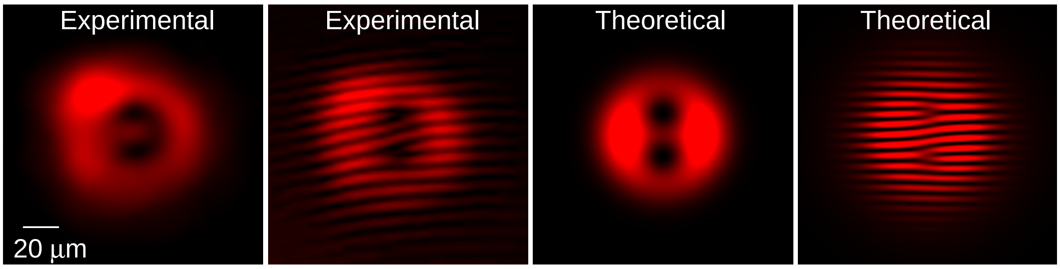

Figure 4.9: Input intensity profiles of dipole with line joining the pair oriented along the y-axis (first and third column) and corresponding interferograms (second and fourth column).

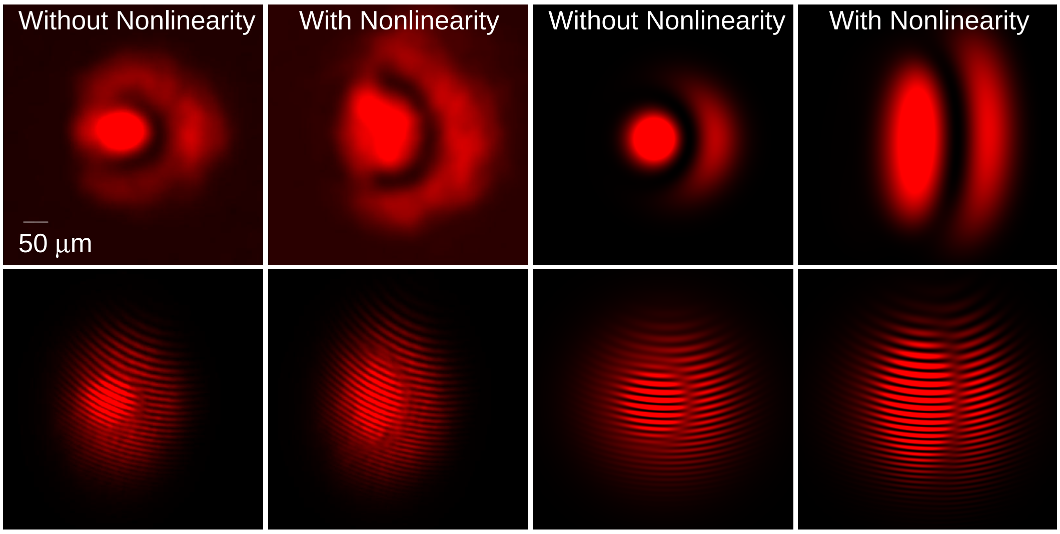

Figure 4.10: Experimental (first and second column) and numerical (third and fourth column) intensity profiles at back surface of the crystal for the dipole shown in Fig. 4.9 as an input beam (first row) and corresponding interferograms (second row).

phase shift between the two intensity lobes and no fork pattern. The observed experimental results are verified by numerical results.

Above results indicate that the formation of stable dipole in a PR medium depends on its behavior in the absence of nonlinearity. When crescent is formed perpendicular to the photovoltaic field then vortices remain separated, however, for the field being parallel, they loose their sign. The dipole dynamics is observed to remain unaffected by the exchange of vortex with its complex conjugate.

Now consider the case of the quadrupole vortex. The complex field distribution of quadrupole at the input of PR medium is given by

$$\begin{aligned} A(x,y,z=0) &= \sqrt{I_m}((x+0.5)+i(y+0.5))((x-0.5)+i(y-0.5)) \\ &\times((x+0.5)-i(y-0.5))((x-0.5)-i(y+0.5)) \\ &\times\exp[-(x^2+y^2)]. \end{aligned} \tag{4.19}$$

The experimental and theoretical intensity distributions at the input of the crystal with their interferograms are shown in Fig. 4.11. Here, each vortex is separated from its nearest neighbor by a normalized distance equal to unit beam waist i.e. the beam waist of a Gaussian host beam.

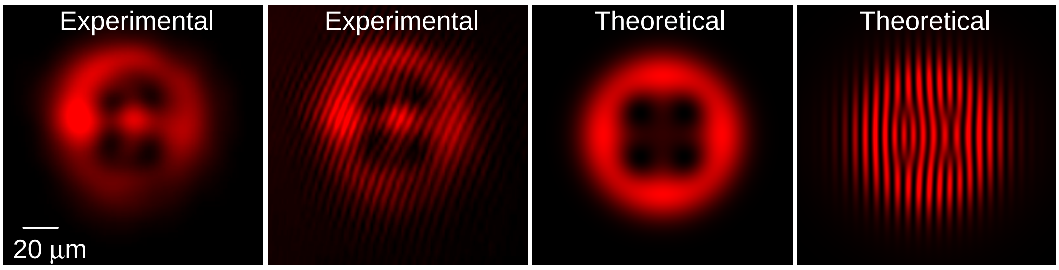

Figure 4.11: Input intensity profiles of quadrupole (first and third column) and corresponding interferograms (second and fourth column).

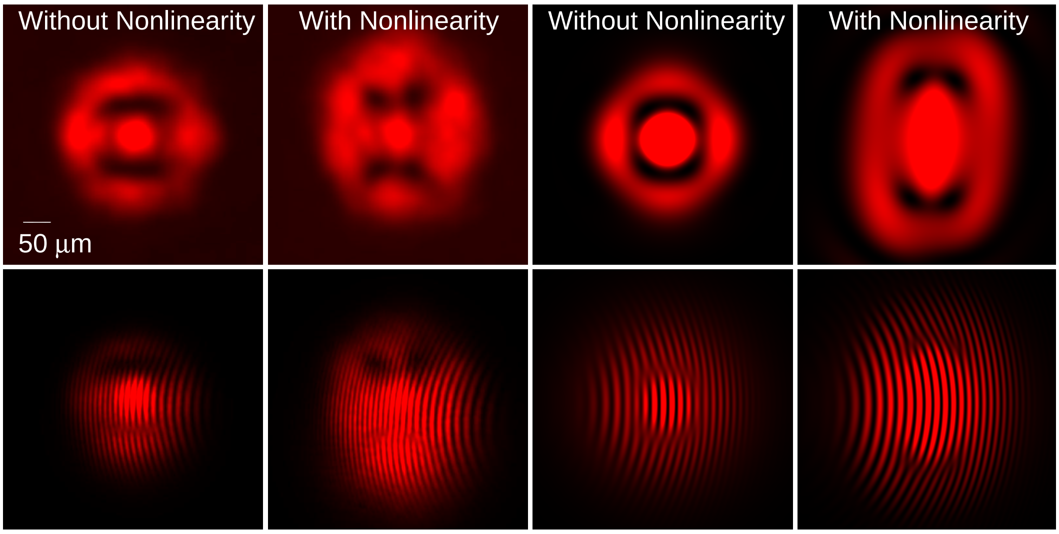

Figure 4.12: Experimental (first and second column) and numerical (third and fourth column) intensity profiles at back surface of the crystal for quadrupole (first row) and corresponding interferograms (second row).

The experimental and numerical results after the propagation of quadrupole through the PR crystal are shown in Fig. 4.12. In the absence of nonlinearity, the vortices in the first and the third quadrant rotate in a clockwise sense, whereas the vortices in the second and the fourth quadrant rotate in an anti-clockwise sense. Therefore, the vortices belonging to the first and the second quadrant come closer and annihilate to form crescent on the upper side. Similarly, the vortices belonging to the third and the fourth quadrant approach each other and annihilate to form crescent on the lower side. In the presence of field, induced nonlinearity creates two separate vortices from each crescent. Thus, a stable quadrupole is generated at the steady state. The presence of vortices are confirmed through the interferograms shown in Fig. 4.12.

One can form a quadrupole by reversing the sign of vortices as well, which can be done by taking complex conjugate of the Eq. (4.19). This is equivalent to rotation of the quadrupole shown in Fig. 4.11 by 90°. In this case, the vortices in the first and the third quadrant rotate in an anticlockwise sense, whereas the vortices in the second and the fourth quadrant rotate in a clockwise sense in the absence of nonlinearity. Therefore, the crescent structure is formed

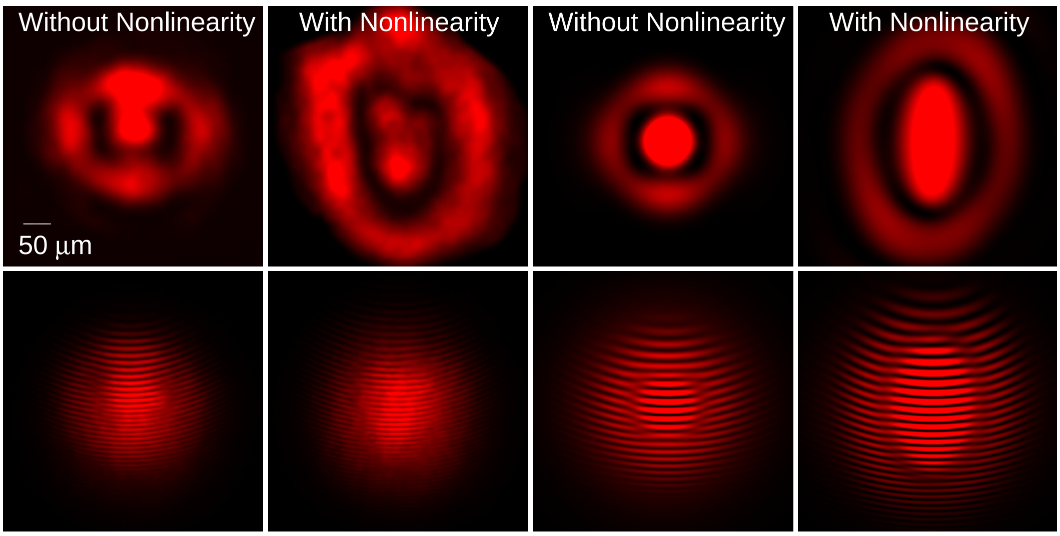

Figure 4.13: Experimental (first and second column) and numerical (third and fourth column) intensity profiles at back surface of the crystal for complex conjugated quadrupole (first row) and corresponding interferograms (second row).

at left and right sides instead of upper and lower sides. Here, crescents are parallel to the direction of photovoltaic field of the nonlinear crystal. In the presence of the nonlinearity, both the crescents merge with each other due to the defocusing and produce an elliptical dark ring at the steady state. This is shown experimentally and numerically in Fig. 4.13.

The results show that the exchange of vortices with their complex conjugates in a quadrupole will change the orientation of crescents. Therefore, it will affect the dynamics of vortices unlike vortex dipole. For crescents being perpendicular to the photovoltaic field, one obtains a stable quadrupole structure while an elliptical dark ring is observed for crescents being parallel to the field.

Conclusion

In conclusion, we have studied the orientation dependent propagation of the dipole and the quadrupole through a photovoltaic PR medium with defocusing nonlinearity. The formation of stable dipole as well as quadrupole in the PR medium is decided by the orientation of crescent structure formed in the linear regime. There is a stable dipole or quadrupole formation if the crescent formed without nonlinearity is perpendicular to the photovoltaic field of the nonlinear crystal. Our results demonstrate that the dipole and the quadrupole are the solutions of nonlinear PWE with the defocusing PR nonlinearity.

4.2 Hermite-Gaussian Beams

Since the last two decades, the self-focusing and self-defocusing nonlinearity are used to generate bright and dark soliton in the PR materials respectively. The dark soliton is formed through the propagation of dark band or notch embedded in a uniform background light through the PR media. Two types of dark solitons are observed in the PR media, 1) Dark screening solitons [30] and 2) Dark photovoltaic solitons [24]. These solitons can be used to form X and Y junctions waveguides [18].

However, dark solitons are observed to be unstable. They go under the transverse instability during propagation. This instability leads to formation of optical vortices, a phase singularity in the light field [90,91]. It was proposed that the transverse instability can be suppressed by bending the dark stripe to form a dark ring [18, 93]. We will study propagation of the dark ring beam in the next section.

In this work, we have generated dark stripe or band using HG modes. The HG modes contain dark stripes with π phase jump which act as edge dislocations. We have studied propagation of these stripes through the defocusing PR media.

Numerical Model

To study propagation of dark stripe through a photovoltaic PR medium, we have used an HG mode having complex field distribution

$$A(x, y, z = 0) = \sqrt{I_m}\exp[-(x^2 + y^2)]H_m[\sqrt{2}x]H_n[\sqrt{2}y], \tag{4.20}$$

where, I_m is the peak intensity normalized by the background illumination. We have used numerical model as explained in Section (4.1.2) to study the propagation of field given by Eq. (4.20).

Experiment

The experimental setup is shown in Fig. 4.6. We have done same experiment as mentioned in the last section (4.1.2) by replacing a CGH of dipole vortex with the CGH of HG beam.

Results and Discussion

Figure 4.14 shows experimental observation of nonlinear propagation of dark stripe beam generated from HG beam with m=0 and n=1. In this case, the dark stripe is perpendicular to the y-axis i.e. the c-axis of the crystal. In the absence of nonlinearity, the beam diffracts naturally. As the beam propagates, a space charge field starts to build up with time and at steady state it forms

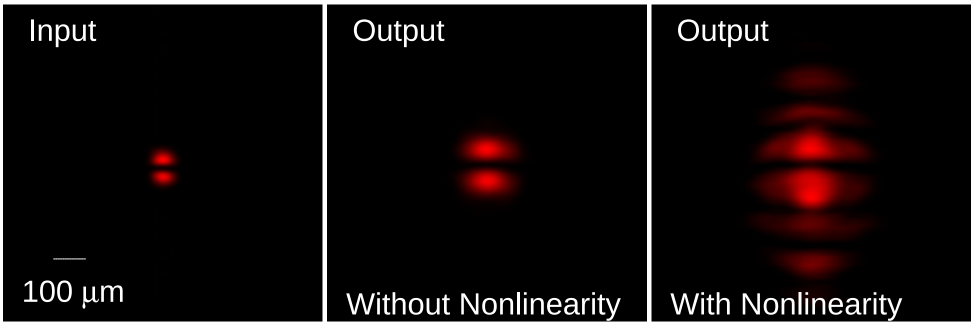

Figure 4.14: Experimental propagation dynamics of HG beam with m=0 and n=1

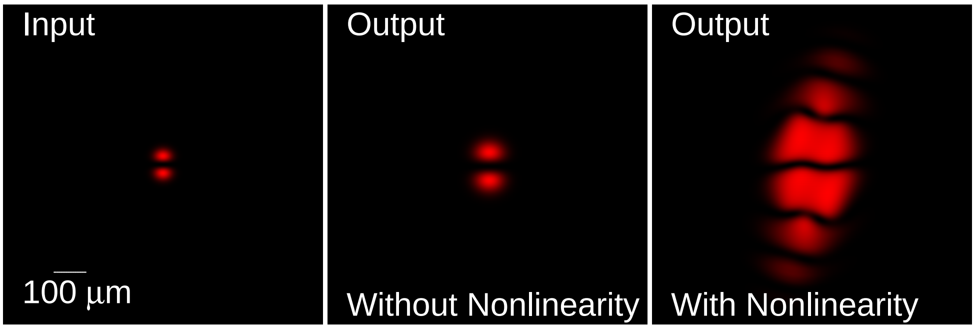

Figure 4.15: Numerical propagation dynamics corresponds to Fig. 4.14

a strong nonlinearity. Two lobes of the HG beam get defocused due to this nonlinearity, which leads to the self focusing of the dark stripe sandwiched between them, and develops transverse instability, consequently [90, 91]. The radiated waves formed over the bright lobes due to instability, decay while propagating away from the center. It seems that the dark stripe looses its energy in the form of these radiated waves. However, we could not observe any sign of vortices unlike for the case of dark stripe generated from glass slides [24]. The observed experimental results match with numerical results.

Now we consider the case of HG beam with m=1 and n=0. In this case, the dark stripe is parallel to the c-axis of the crystal. The experimental results for this beam propagation through the PR crystal are shown in Fig. 4.16. In the absence of nonlinearity, the beam diffracts naturally. In the presence of nonlinearity, two lobes of the HG beam are defocused along the c-axis, therefore, there is no self-focusing of the dark stripe. The experimental results are verified numerically.

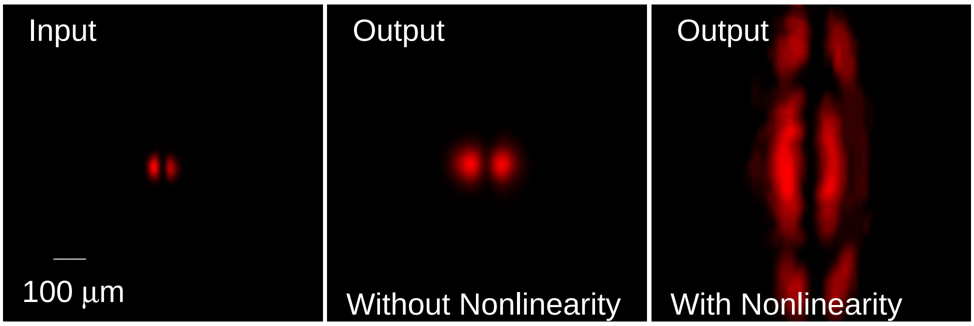

Figure 4.16: Experimental propagation dynamics of HG beam with m=1 and n=0

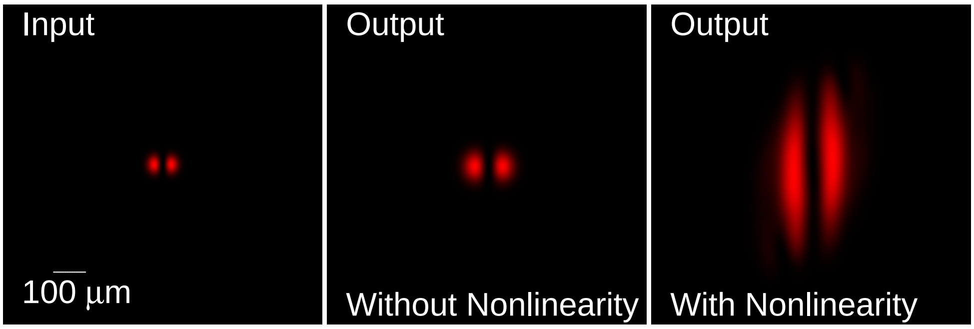

Figure 4.17: Numerical propagation dynamics corresponds to Fig. 4.16

Conclusion

We conclude that when a dark stripe beam produced from an HG beam is perpendicular to the c-axis of the crystal, the radiated waves are formed over the bright lobes due to instability, however, they decay while propagating away from the center.

4.3 Laguerre-Gaussian Beams

An optical dark ring beam forms a ring dark soliton, which is a special class of the dark solitons, while propagating through Kerr media [93–95]. The concept of ring dark solitons has also been studied in Bose-Einstein condensates (BECs), where they split into cluster of vortex pairs [96]. Recently, a comparative numerical study has been made on the dynamics of ring dark solitons in BECs and nonlinear optics [97].

In the present work, instead of Kerr media, we have taken a photovoltaic photorefractive (PR) medium with defocusing nonlinearity. It is observed that the dark ring undergoes a modulation instability called snake instability as it propagates through the PR medium. Unlike forming a dark soliton in the case of Kerr media, this instability leads to formation of a quadrupole that remains stable while propagating through the PR medium.

We generate dark rings using LG modes since LG beams contain dark rings in their intensity profiles with a π phase jump, which are defined by the radial index p. In addition, they have a twist of $2\pi l$ in their wavefront due to azimuthal phase term $\exp[il\phi]$. The azimuthal index l is called topological charge of the beam. The twist generates screw dislocation, while the π phase jump generates edge dislocation. Thus, LG beams have the advantage that one can obtain dark rings with and without topological charge.

We construct the LG beams with different radial and azimuthal indices by using a computer generated hologram (CGH). We observe that the LG beam with zero topological charge gains topological charge in the form of a quadrupole, while propagating through the lithium niobate crystal [92]. It is observed that the LG beam with unit topological charge breaks to form a pair of bright lobes, whereas the beam with high topological charge decays into unit charges in the PR medium with defocusing nonlinearity [77,87]. However, the breakup of a single charge vortex can be suppressed by the hybrid nonlinearity that is generated using nonconventional biasing in the PR medium [78].

Numerical Model

To study propagation of a dark ring through a photovoltaic PR medium, we have used a LG mode having complex field distribution

$$A(x,y) = \sqrt{I_m}(\sqrt{2(x^2+y^2)})^l \exp[-(x^2+y^2)]\exp[il\theta]L_p^l[2(x^2+y^2)], \quad (4.21)$$

at the input of the PR medium. In Eq. (4.21) $\theta = \arctan(y/x)$, L_p^l is the associated Laguerre polynomial and I_m is the initial peak intensity.

Figure 4.18 shows spatial dynamics of an LG beam having a single dark ring ($p = 1$ and $l = 0$) through the photovoltaic PR media with w_0= 26 μm, I_m=

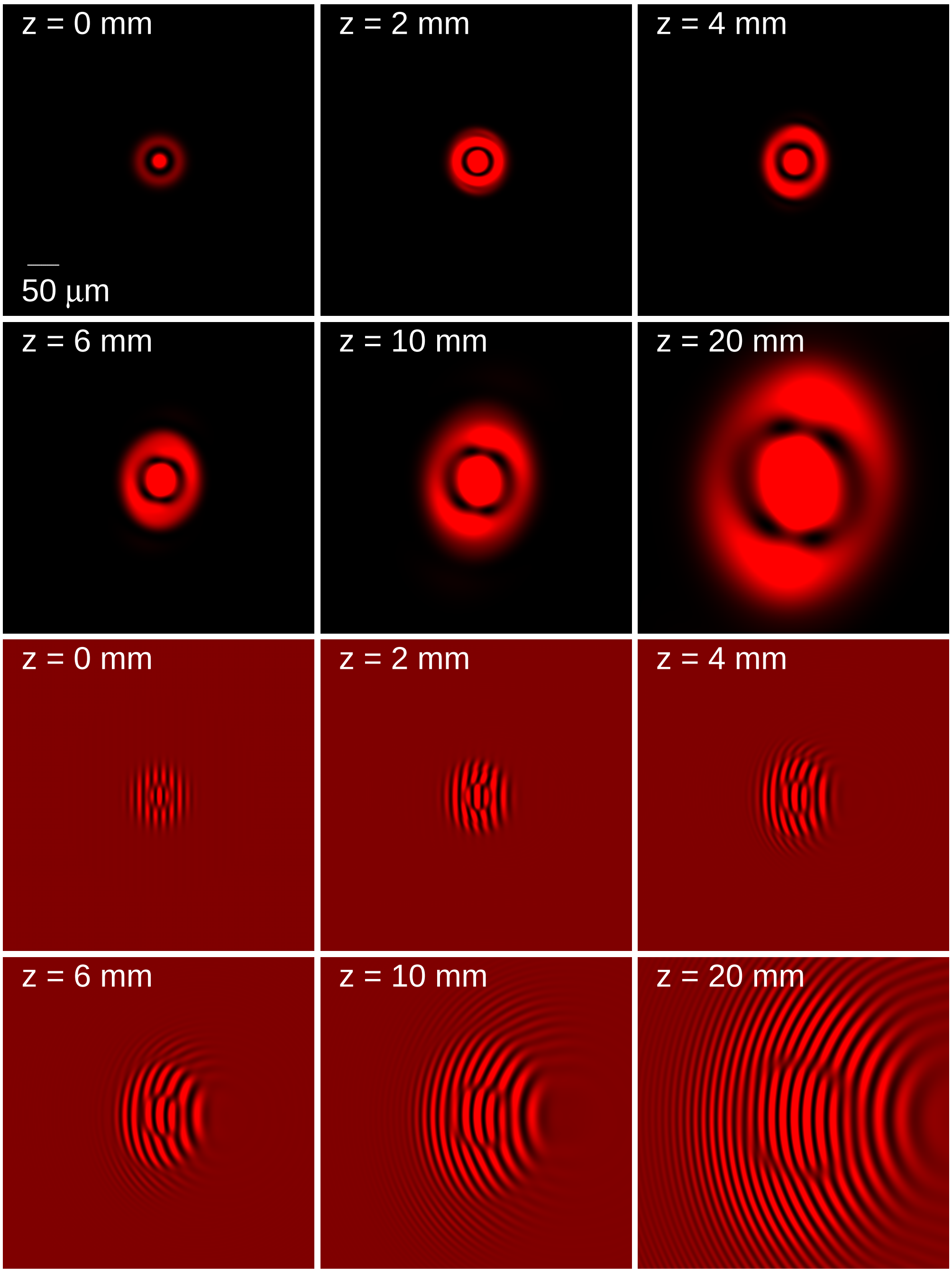

Figure 4.18: Numerical intensity distributions (first and second row) and corresponding interferograms (third and fourth row) at different propagation distances for LG beam with $p = 1$ and $l = 0$.

1 and E_p= -27 kV/cm. As the beam propagates, both the center lobe and the bright ring experience self-defocusing, consequently the sandwiched dark ring goes through self-focusing. Since the crystal is anisotropic, the self-focusing of the ring occurs asymmetrically. The self-focusing is more along the c-axis (y-

axis in our case), as seen in the image at $z = 2$ mm (Fig. 4.18). The radiated waves can be seen over the bright ring at $z = 2$ and 4 mm, which decay while propagating away from the center. A similar decay is observed for the case of a dark stripe beam [90, 91]. As the beam propagates, two vortex-antivortex pairs are generated along the c-axis to form a quadrupole that diffracts with distance. The above results show that the single edge dislocation of the dark ring converts into multiple screw dislocations in the form of quadrupole as the beam propagates in the PR material.

Experiment

The experimental setup is shown in Fig. 4.6. In the current experiment, we have generated LG beams instead of dipole vortex.

Results and Discussion

Figure 4.19 shows experimental and numerical results for propagation of the dark ring, the LG beam with unit radial index, through the PR crystal. In the absence of nonlinearity, there is a natural diffraction for the input dark ring.

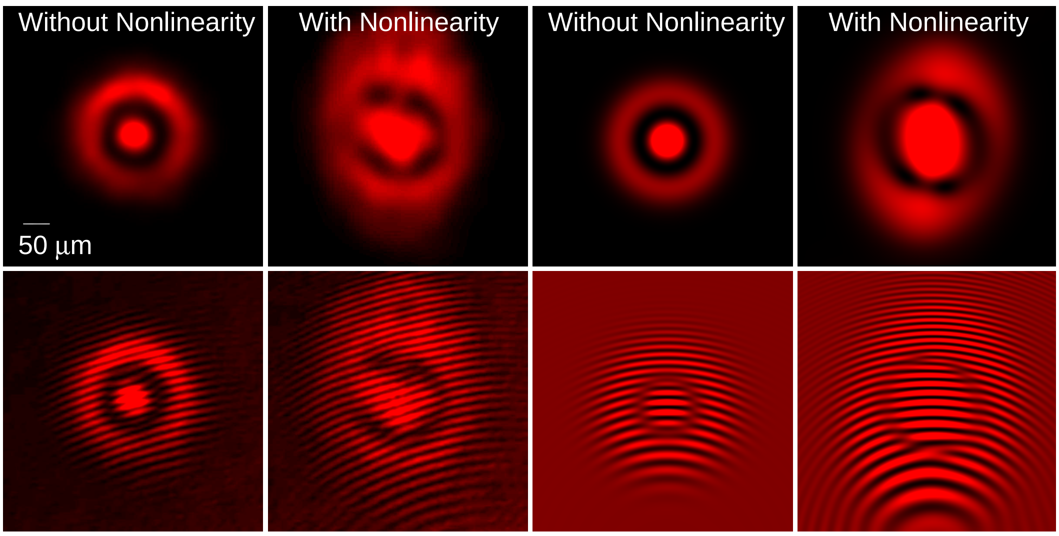

Figure 4.19: Experimental (first and second column) and numerical (third and fourth column) intensity profiles at back surface of the crystal for LG beam with $p = 1$ and $l = 0$ (first row) and corresponding interferograms (second row).

As the beam propagates, a space charge field starts to build up with time, which increases the nonlinearity of the crystal. The center lobe and the bright ring of the LG beam are defocused by the generated field that leads to the self-focusing of the dark ring. However, instead of forming a dark ring soliton, it evolves into vortex-antivortex pairs, forming a quadrupole.

This kind of quadrupole generation has been observed in uniaxial crystals, for a linearly polarized Gaussian beam propagating along the optic axis or the c-axis [88, 89]. However, in our case, we have sent the LG beam with a single dark ring perpendicular to the c axis. It should be noted that the cause of formation of the quadrupole is different in the two cases. In our case, it is the defocusing nonlinearity, while it is polarization singularities in the case of uniaxial crystals. The presence of vortices are confirmed through the interferograms shown in Fig. 4.19. The experimental results are in good agreement with the numerical results.

We have studied the propagation of an LG beam with two dark rings, $p = 2$, as well. The intensity profiles and the interferograms at the back face of the crystal are shown in Fig. 4.20. At steady state, one observes four vortex and

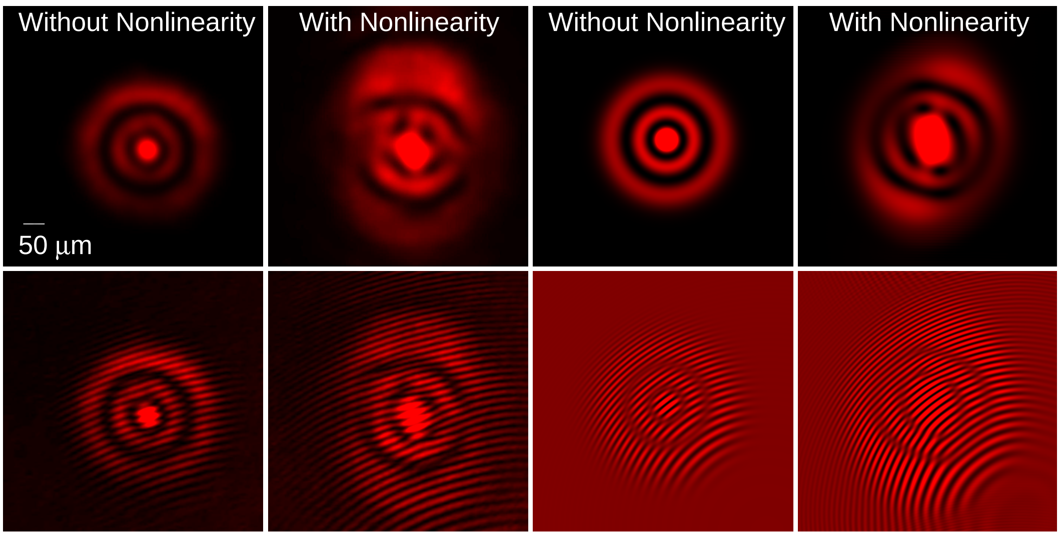

Figure 4.20: Experimental (first and second column) and numerical (third and fourth column) intensity profiles at back surface of the crystal for LG beam with $p = 2$ and $l = 0$ (first row) and corresponding interferograms (second row).

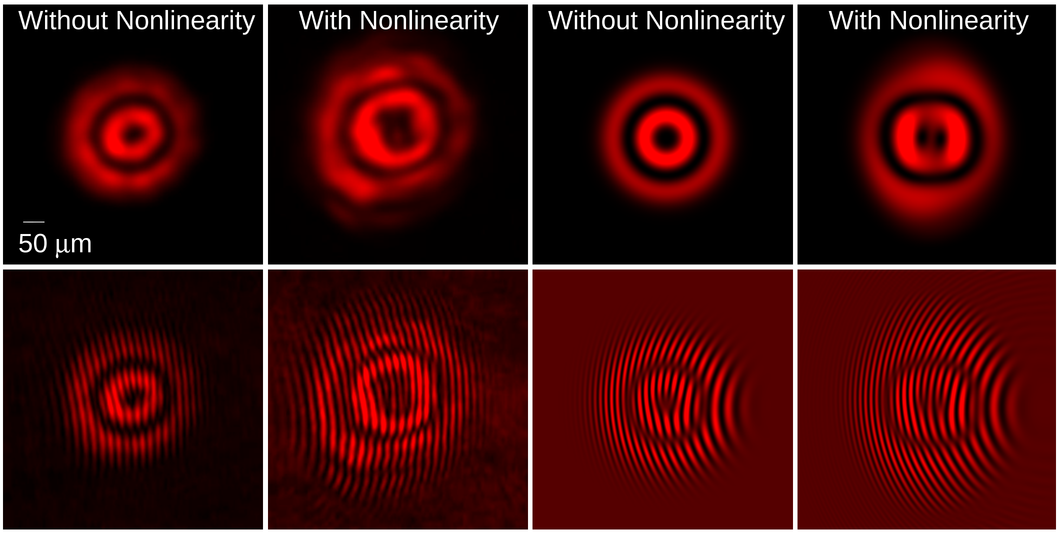

Figure 4.21: Experimental (first and second column) and numerical (third and fourth column) intensity profiles at back surface of the crystal for LG beam with $p = 1$ and $l = 2$ (first row) and corresponding interferograms (second row).

antivortex pairs. As we increase the number of dark rings by increasing the value of p in the LG beam, each of the ring ends up in a quadrupole.

We have also considered experimentally and numerically the case of a dark ring with doubly charged vortex at the center. To form such a structure, one produces an LG beam with radial mode index $p = 1$ and azimuthal index $l = 2$. Figure 4.21 shows experimental and numerical results at the back face of the PR crystal. As the beam propagates, the nonlinearity increases. Because of nonlinearity, the center lobe containing a topological charge ($l = 2$) breaks into two unit charge vortices. At the same time, the dark ring breaks to form a quadrupole. Therefore, at steady state, an LG beam with $p = 1$ and $l = 2$ forms a system of six vortices, as shown in Fig. 4.21. The unit charges at the center align perpendicular to the c axis of the crystal [77,78]. We have observed that, at higher values of p and l, the dark rings break to form quadrupoles, but the high topological charge at the center decays into an array of vortices with unit charge. It should be noted that this dynamics becomes more complicated at higher nonlinearity.

The anisotropic nonlinearity of the photovoltaic PR crystal plays a crucial role in the present experiment, which results in instability for the dark ring propagation [90, 91]. When the light beam propagates through this crystal, a photovoltaic field starts to build up along the c axis and consequently develops transverse modulation instability. The dark rings of an LG beam are subjected to this instability and they are distorted to form a quadrupole vortex. It should be noted that the same instability is responsible for distortion of the self-trapped vortex in the photovoltaic PR crystal [98]. Along with the modulation instability, the photovoltaic-field-induced nonlinearity in the crystal results in stretching of the beam that gives ellipticity to the input beam. Because of this ellipticity, high charge vortices of the LG beam break into single charge vortices [99, 100]. We would like to emphasize that any distortion to the high-charge-carrying symmetric vortex beam results in the breaking of the high charge vortex into unit vortices in linear [100] as well as nonlinear media [77,78].

It would be worthwhile to compare our results with propagation of a dark stripe beam in PR media. In contrast to a dark stripe breaking into a number of vortices [90,91], we have observed that the dark ring breaks into just two pairs of vortex-antivortex and forms a quadrupole in the defocusing PR medium. One can compare our results with instability of the ring dark soliton in a BEC, where it breaks into a necklace array consisting of vortex-antivortex pairs, but in multiples of four [96], and also with a Kerr medium, where it forms a stable dark ring soliton [93–95].

Conclusion

In conclusion, we have studied the propagation of dark rings, with and without topological charge, in a photovoltaic PR medium. We observe, for the first time to the best of our knowledge, the formation of quadrupoles in a photovoltaic PR medium. In this process, the edge dislocation converts into screw dislocations. We expect that Bessel beams that carry edge dislocations will show a similar formation of quadrupoles when they propagate through such a nonlinear medium.

4.4 Ring Lattice Beams

The superposition of two LG beams with different radial and azimuthal indices, but having the same waist position and waist parameter, generates interesting light structures. In literature, these structures have been called by various names such as composite vortex beam [101], Ferris wheel [102], combined beams [103], spiral beams, and linear azimuthons [104]. They show diffraction broadening with some of them showing a rotational dynamics as well [103–105]. These beams preserve their shape, like Gaussian beams.

The Bessel beam and the Airy beams which are also solutions of the paraxial diffraction equation, are non-diffracting, unlike the beams discussed above. It has been observed that these diffraction-free beams show the self-reconstruction or self-healing property [40,47]. However, the ring lattice beams, the superposition of LG beams which are diffracting in nature also show self-healing property [106].

The superposed structures generated from LG beams have been studied in highly nonlocal nonlinear media [107, 108] and BEC [109]. However, in this work, we have studied their dynamics in a PR medium with defocusing nonlinearity. We generate the optical ring lattice by using a CGH, which is formed by interference of the plane wave and the two superposed LG beams with different azimuthal index l. For simplicity, radial index p of the beams has been taken as zero. In this work we have examined the rotational dynamics of ring lattice beams in both linear as well as nonlinear medium.

4.4.1 Linear Dynamics

Theory

The complex field amplitude of LG beams are written as (Eq. (1.27))

$$\begin{aligned} A_p^l(r,\phi,z) &= \frac{1}{w}\sqrt{\frac{2p!}{\pi(p+|l|)!}}(\frac{r\sqrt{2}}{w})^{|l|}\exp[-\frac{r^2}{w^2}]\exp[-\frac{ikzr^2}{2(z^2+z_R^2)}] \\ &\quad \times L_p^l(\frac{2r^2}{w^2})\exp[-il\phi]\exp[i(2p+l+1)\psi]. \end{aligned} \tag{4.22}$$

When two LG beams having indices (p, l) and (p', l'), are superposed with common waist and waist parameter, they form a field amplitude written as

$$A(r, \phi, z) = A_p^l + A_{p'}^{l'}. \tag{4.23}$$

The above superposed field gives an intensity distribution whose azimuthal orientation changes with z as [103–105]

$$\phi = \phi_0 + B\psi \tag{4.24}$$

where B is a constant and defined as

$$B = \frac{2(p - p') + |l| - |l'|}{l - l'}. \tag{4.25}$$

The sign of B decides the sense of rotation of the superposed structure (it is optical ring lattice in our case).

Experiment

To produce the ring lattice in our laboratory, we have employed a computer generated holography technique which is discussed in the second chapter. We make an interferogram with Eq. (4.23) and plane wave $\exp[ik_x x]$. This interferogram is imprinted on the spatial light modulator (SLM) (Holoeye, CR-2500) via a computer.

The experimental setup is shown in Fig. 2.5. We have used a stabilized He-Ne laser (Spectra-Physics, Model 117A) as the light source. By illuminating the SLM with the laser beam, the ring lattice is generated as a diffracted order in the reflection. A biconvex lens ($f = 50$ cm) is used to create the waist with a view to study the propagation dynamics, taking ($f = 50$ cm)at the waist. The CCD camera (MediaCybernetics, Evolution VF cooled Color Camera) is used to capture the images at various propagation distances.

Results and Discussion

The rotational dynamics of the ring lattice in free space are shown in Fig. 4.22 at different z distances. In the case of $l = 3$ and $l' = -3$, there is no rotation because $B = 0$ for this case. The superposed beams form a bright ring lattice with $2l$ petals which show diffraction while propagating in free space.

Now we study the case where l and l' are different. Let us take $l = -3$ and $l' = 4$. The superposition of these LG beams again forms bright ring lattice with $|l| + |l'|$ petals which show rotational dynamics along with diffraction. However, when we take $l = -1$ and $l' = -6$, i.e., the initial LG beams having the same sign of the azimuthal index, the superposition results into the dark ring lattice. For this case, $B = -1$, which implies the opposite sense of rotation. We have also verified that as the formed ring lattice propagates, its angular speed decreases [103–105]. In Fig. 4.23, we have shown the theoretical results obtained from (Eq. (4.23)).

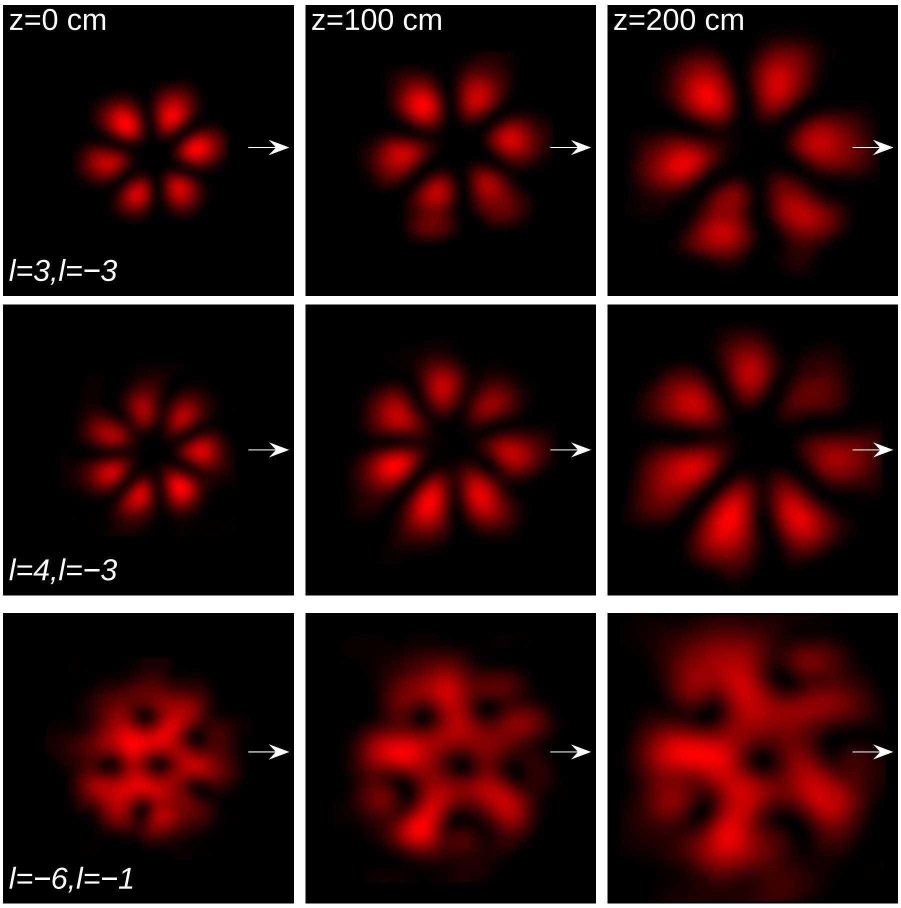

Figure 4.22: Experimental intensity profile. For reference, the horizontal arrow has been placed to visualize the rotation.

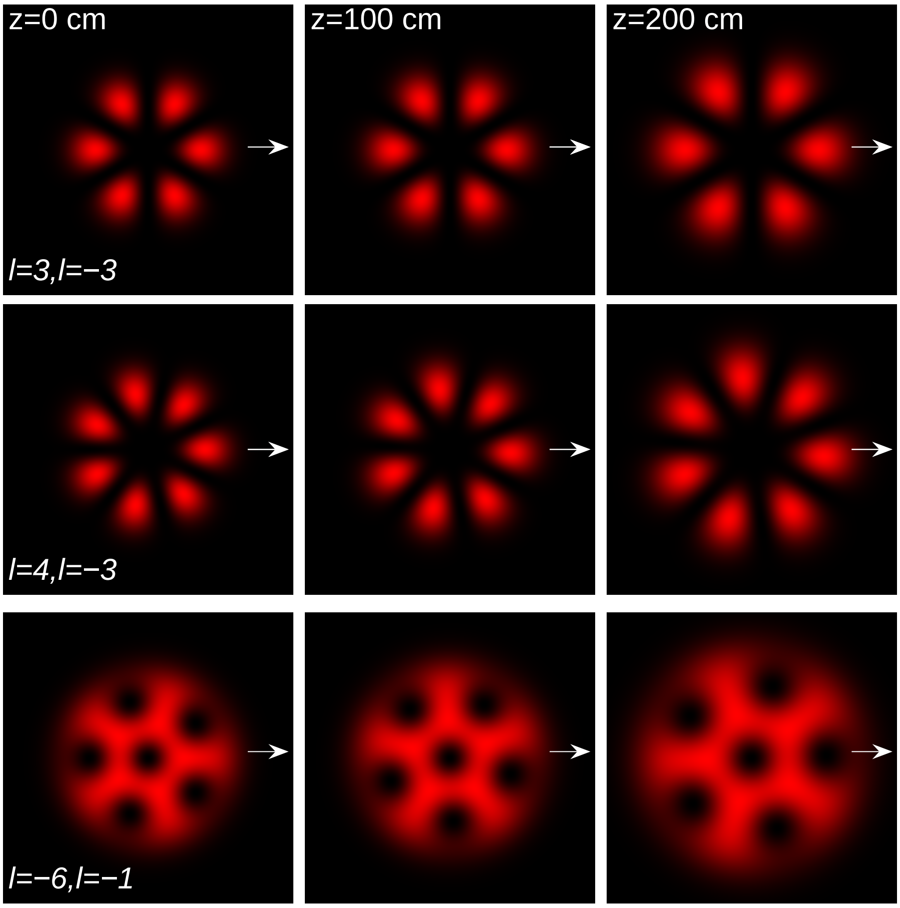

Figure 4.23: Theoretical intensity profile for the same z values as in Fig. 4.22.

4.4.2 Nonlinear Dynamics

Numerical Model

The complex field distribution of lattice beams at $z = 0$ is written as

$$A(x, y, z = 0) = \sqrt{I_m}((\sqrt{2}r)^l L_l^p[2r^2]\exp[-il\phi] + (\sqrt{2}r)^{l'} L_{l'}^p[2r^2]\exp[-il'\phi]) \times\exp[-(x^2 + y^2)]. \quad (4.26)$$

Here, r is normalized by w_0. We have used same numerical model as explained in Section (4.1.2) to study the field propagation given by Eq. (4.26).

Experiment

The experimental setup is shown in Fig. 4.6. We repeat the same experiment as mentioned in Section (4.1.2). However, instead of dipole vortex beam we have taken ring lattice beam. The beam waist w_0 of a Gaussian beam in which the ring lattices are embedded, is 50 μm. The peak intensity I_m is 0.05.

Results and Discussion

Figure 4.24 shows propagation of ring lattice beam with $l = 3$ and $l' = -3$. From interferogram, it is clear that there are π phase jumps between any two petals of the ring lattice considered. These phase jumps form edge dislocations. In the absence of nonlinearity, there is a natural diffraction for the input ring lattice beam. As this beam propagates, a space charge field builds up in time. At steady state, these fields generate nonlinearity which causes defocusing of the ring lattice. Since there is no fork pattern in the interferogram shown in Fig. 4.24, conversion of edge dislocations to screw dislocations, unlike dark ring beam, does not happen for this ring lattice. The experimental results are verified with numerical results shown in Fig. 4.24.

Now consider the ring lattice beam which has rotational dynamics. The propagation dynamics of ring lattice beam with $l = -3$ and $l' = 4$ is shown in Fig. 4.25. The edge dislocations are present between any two petals of

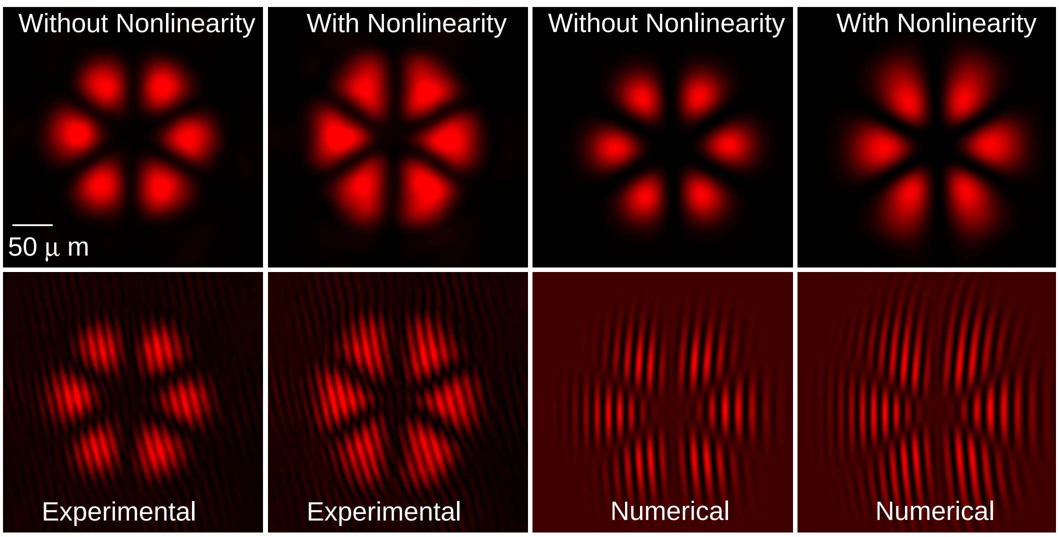

Figure 4.24: Experimental (first and second column) and numerical (third and fourth column) intensity profiles at back surface of the crystal for ring lattice beam with $l = 3$ and $l' = -3$ (first row) and corresponding interferograms (second row).

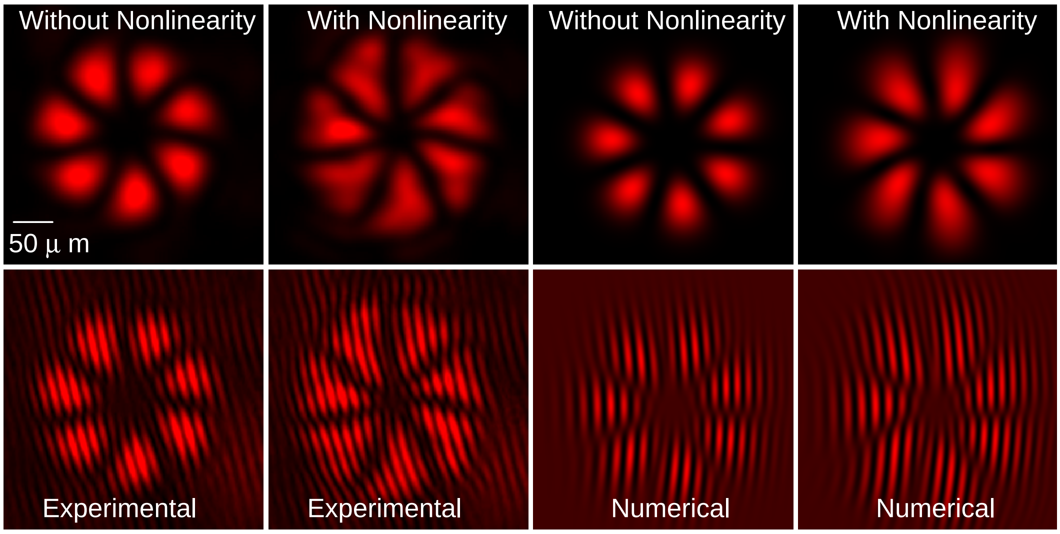

Figure 4.25: Experimental (first and second column) and numerical (third and fourth column) intensity profiles at back surface of the crystal for ring lattice beam with $l = -3$ and $l' = 4$ (first row) and corresponding interferograms (second row).

the ring lattice similar to the previous case. In the absence of nonlinearity, there is a natural diffraction for the ring lattice beam along with rotation. As the beam propagates, a space charge field starts to build with time which increases the nonlinearity in the crystal. In the presence of nonlinearity, at the steady state, the defocusing of this ring lattice creates singularities in the form of screw dislocations in the region between the petals. We have observed fork patterns in the interferogram which confirm that there is a transition from edge dislocations to screw dislocations. These experimental results are in agreement with numerical results shown in Fig. 4.25.

Conclusion

It is clear from the above results that if the ring lattice beam has rotational dynamics then only edge dislocations of that beam convert into screw dislocations. For ring lattice with zero rotation, the petals are defocused in the defocusing PR media, however, the edge dislocations between them remain as it is.

Chapter 5

Nonlinear Dynamics of Non-Diffracting Beams

There are certain beams which are immune to diffraction. They propagate in linear media or free space without changing their beam shape, such beams are called as non-diffracting or diffraction-free beams. Airy beams and Bessel beams are examples of these beams. In this chapter, we have discussed phenomena arising due to propagation of these beams in the PR media.

We have experimentally generated Airy beams to study their propagation through a PR medium in the presence of an external applied field. As we increase the external field, energy from the bottom lobes is transferred to the upper lobes of Airy beams. The direction of energy transfer is along the c-axis of the crystal. We compare the isotropic and the anisotropic models for the PR materials in the case of Airy beams' propagation.

In the last chapter, we have found that a dark ring beam having edge dislocations, forms quadrupole while passing through a PR medium. The Bessel beams ideally have infinite number of such dark rings. We have examined that these rings of the Bessel beam also form quadrupole in the defocusing PR medium.

Since the propagation dynamics of Airy and Bessel beams in a linear medium are well understood, we present results on their nonlinear propagation. In Section 1, we discuss about Airy beams' interaction in the PR media.

The formation of quadrupole from Bessel beam is described in Section 2.

5.1 Airy Beams

Airy beams are one of the non-diffracting solutions of the PWE. It was first realized by Berry and Balazs in the context of quantum mechanics that the Airy wave packet could be solution of the Schrödinger equation [44]. Due to similarity of the Schrödinger equation with the PWE, the Airy wave packet can be observed as the Airy beams in optics, forming 1D as well as 2D beams [4]. Apart from non-diffracting nature and consequent self-healing property, Airy beams show acceleration even in free space. Due to their peculiar properties, Airy beams find applications which include optical trapping [48], and plasma wave-guiding [49].

Recently, it has been shown numerically that Kerr, quadratic and PR nonlinearities can support 1D self-accelerating self-trapped optical beams [110]. Before that, the diffusion trapped 1D Airy beams were observed in the PR media [111]. The behavior of 2D Airy beams propagating from a nonlinear medium to a linear medium have also been studied recently [112]. These results were explained using the isotropic model [72].

In the present work, we have studied the propagation of 2D Airy beams through a PR medium in the presence of an external applied field. We observe deacceleration of the Airy beams in the form of energy transfer among the lobes of the Airy beams. We have compared our experimental results with numerical models, both the isotropic [72] and the anisotropic [73]. Our experimental results of Airy beams propagation through the PR media under an external applied field were observed to follow the anisotropic model.

Theoretical Background

The field amplitude of Airy beams can be written as (Eqs. 1.29-1.30),

$$A(x, y, z) = A_x(x, z)A_y(y, z), \tag{5.1}$$

where

$$A_x(x,z) = Ai[\frac{x}{x_o} - (\frac{z}{2kx_o^2})^2 + \frac{iaz}{kx_o^2}]$$
$$\exp[\frac{ax}{x_o} - \frac{a}{2}(\frac{z}{kx_o^2})^2 - \frac{i}{12}(\frac{z}{kx_o^2})^3 + \frac{ia^2}{2}\frac{z}{kx_o^2} + \frac{ix}{2x_o}\frac{z}{kx_o^2}], \quad (5.2)$$

$$A_y(y,z) = Ai[\frac{y}{y_o} - (\frac{z}{2ky_o^2})^2 + \frac{iaz}{ky_o^2}]$$
$$\exp[\frac{ay}{y_o} - \frac{a}{2}(\frac{z}{ky_o^2})^2 - \frac{i}{12}(\frac{z}{ky_o^2})^3 + \frac{ia^2}{2}\frac{z}{ky_o^2} + \frac{iy}{2y_o}\frac{z}{ky_o^2}] \quad (5.3)$$

The Fourier transform of Eq. (5.1), at $z = 0$ is

$$A(k_x, k_y) = \exp[-a(k_x^2 + k_y^2)]\exp[i(k_x^3 + k_y^3)]. \quad (5.4)$$

where k_x and k_y are the spatial frequencies. The equation (5.4) contains two terms, first one is a Gaussian and another is a cubic phase term. It implies that the Airy beams can be formed by Fourier transformation of the Gaussian beam with a cubic phase factor.

Numerical Model

We have employed both the isotropic and the anisotropic model of the PR media. In the case of isotropic model, the change in refractive index in the PR media is given by (Eq. (3.11) and (3.19))

$$\Delta n = -\frac{1}{2}n_0^3 r_{eff} E_0 \frac{1}{1+I}, \quad (5.5)$$

where n_0 is the refractive index in the absence of light and E_0 is the applied electric field. The input beam intensity I is normalized by a background illumination. However, the change in index of refraction Δn, in the anisotropic model is written as (Eq. (3.17) and (3.19))

$$\Delta n = \frac{1}{2}n_0^3 r_{eff} \frac{\partial \phi}{\partial y}. \quad (5.6)$$

The space charge potential ϕ can be calculated using following equation,

$$\nabla^2\phi + \nabla\phi \cdot \nabla[ln(1+I)] = E_0 \frac{\partial ln(1+I)}{\partial y}. \quad (5.7)$$

Equation (5.7) can be solved numerically as shown in Appendix B.

The complex field distribution of Airy beams at the input of the PR crystal can be written as

$$A(x, y) = \sqrt{I_m} Ai[\frac{x}{w_0}]\exp[\frac{ax}{w_0}] Ai[\frac{y}{w_0}]\exp[\frac{ay}{w_0}], \qquad (5.8)$$

where Ai is the Airy function and a is the aperture parameter. w_0 and I_m are the full width half maxima of the main lobe and the input intensity normalized by a background illumination. The experimental value of these parameters are w_0= 11 μm and $I_m = 15$.

The field distribution $A(x, y)$ inside the PR material can be calculated by solving the nonlinear PWE (Eq. (4.14)),

$$\frac{\partial A(x, y)}{\partial z} = \frac{i}{2}\nabla^2 A(x, y) + in_0 k_0^2 w_0^2 \Delta n A(x, y). \qquad (5.9)$$

We have solved Eq. (5.9) as discussed in Appendix A.

Experiment

We have generated Airy beams by using a cubic phase mask [4] which is shown in Fig. 5.1. The cubic phase mask is constructed through a cubic phase term from Eq. (5.4). The experimental setup, to generate the Airy beams and to study their propagation dynamics through the PR crystal is shown in Fig. 5.2.

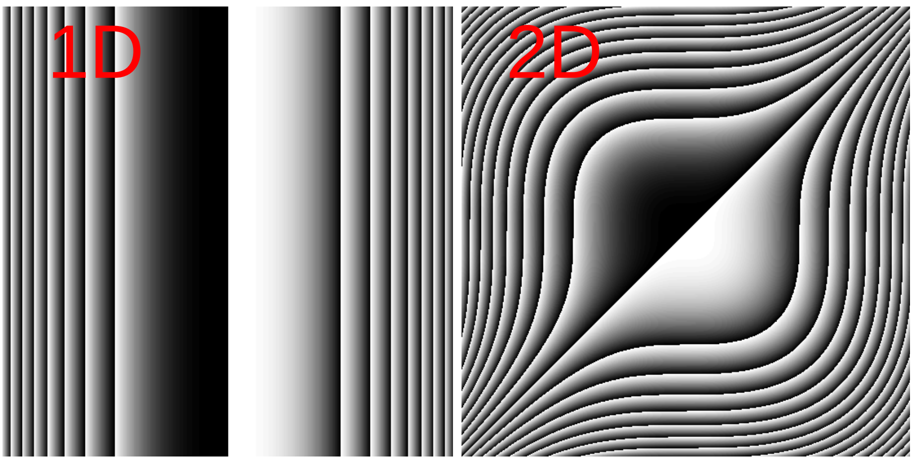

Figure 5.1: Cubic phase mask for Airy beams generation

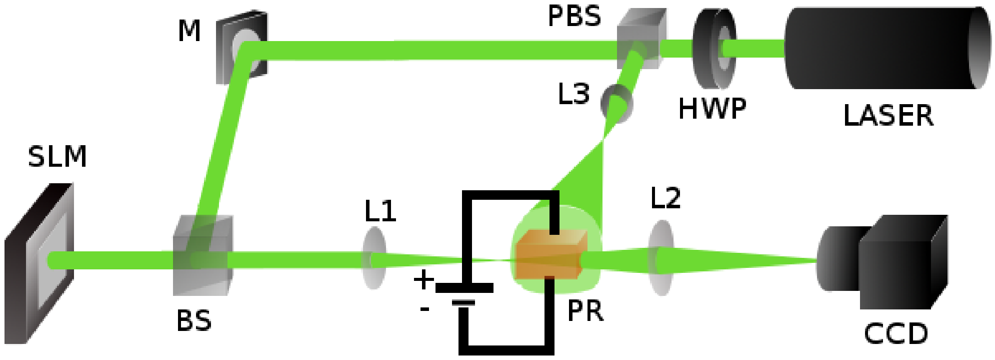

Figure 5.2: Experimental Setup. HWP, half-wave plat; PBS, Polarizing beam-splitter; BS, beam-splitter; L1, L2, L3 lens; M, mirror; SLM, spatial light modulator; PR, photorefractive crystal; CCD, camera

A cubic phase mask which is used to form the Airy beams, is sent to a SLM (P512-0532 Spatial Light Modulator from Boulder Nonlinear Systems, USA) via computer. We have used a solid state pump laser (Coherent, Verdi V10) as light source. The laser beam is divided into two parts using polarizing beam-splitter. The intensity ratio between two beams is controlled by a half-wave plate. One of the beams illuminates the SLM which contains cubic phase mask for generation of the Airy beams. A biconvex lens (f = 15 cm) is used as a Fourier lens. The PR crystal, cerium doped strontium barium niobate (SBN, 5 mm x 5 mm x 10 mm), is placed at the focus because the Airy beams are formed at the focus. A CCD camera (MediaCybernetics, Evolution VF cooled Color Camera) and an imaging lens are used to capture the images at the back surface of the crystal. An external dc field is applied along the c-axis of the crystal. The polarization of input light field is kept along the c-axis. Another beam acts as a background illumination.

Results and Discussion

Figure 5.3 shows experimental observation of Airy beams after propagation through the PR crystal. Figure 5.3a shows the intensity distribution of the Airy beams when no voltage is applied. In this case, the Airy beams show same behavior as in a linear medium. Applying external voltage along the crystal

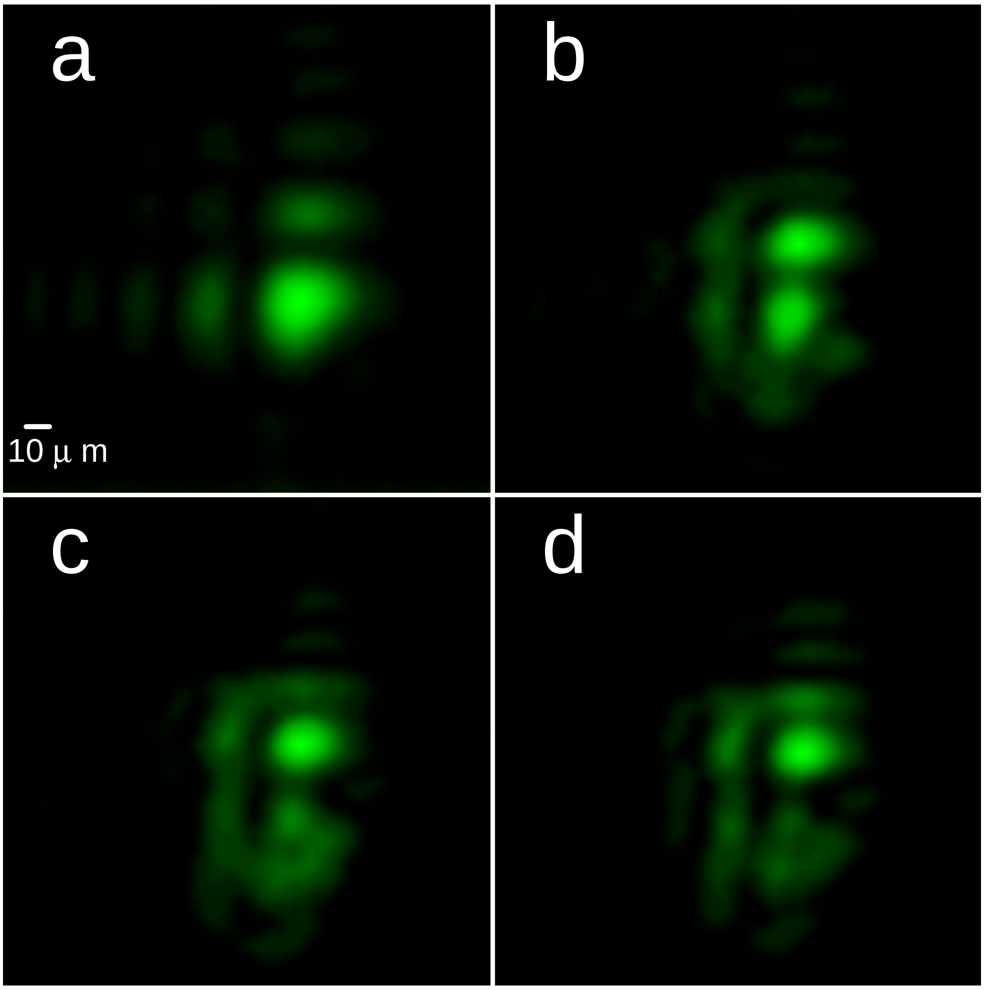

Figure 5.3: Experimental intensity distribution at back surface of the crystal a) 0V, b) 200V, c) 300V, d) 400V.

increases the nonlinearity, which causes focusing of the Airy beams. This leads to the interaction between main lobe and its nearest neighbor situated along the c-axis. With further increase in the applied voltage, the energy of main lobe is transferred to its nearest neighbor along the c-axis of the crystal, i.e. the direction of applied field (Fig. 5.3c and 5.3d). Similar energy transfer occurs for the lobes which are at left of the main lobe. However, due to low intensity it is not visible. Overall, the energy of bottom lobes is transferred towards the upper lobes of Airy beams along the c-axis. It seems that Airy beams deaccelerate along the c-axis. It shows that the results for 1D-self-trapped self-accelerated beams cannot be extended for 2D beams in the PR media [110].

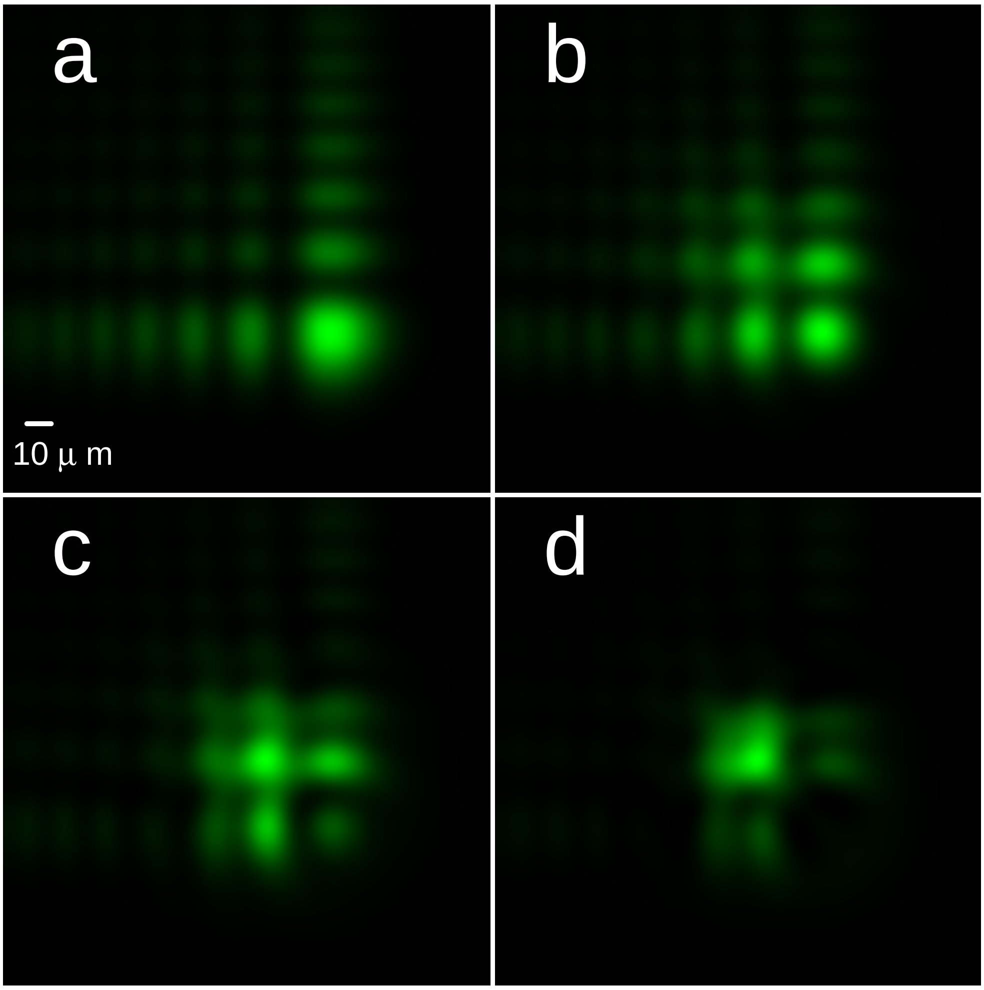

Figure 5.4: Numerical intensity distribution (isotropic model) at back surface of the crystal a) 0V, b) 200V, c) 300V, d) 400V.

Figure 5.4 shows numerical intensity distribution of the Airy beams at the back face of the crystal, calculated by using the isotropic model. The experimental parameters for the results shown in Fig. 5.3 are used for the numerical calculation. As the applied field increases, the energy of main lobe is transferred to its nearest neighbors. Similar results are observed in Ref. [112]. Further increase in the field, causes energy transfer towards the lobes which are in the path of axis of symmetry. In this case the beams deaccelerate in the direction opposite to the direction of original acceleration. But these numerical results do not match with our experimental findings.

Using anisotropic model, the output intensity distribution of Airy beams at the back plane of the crystal are shown in Fig. 5.5. It is found that the

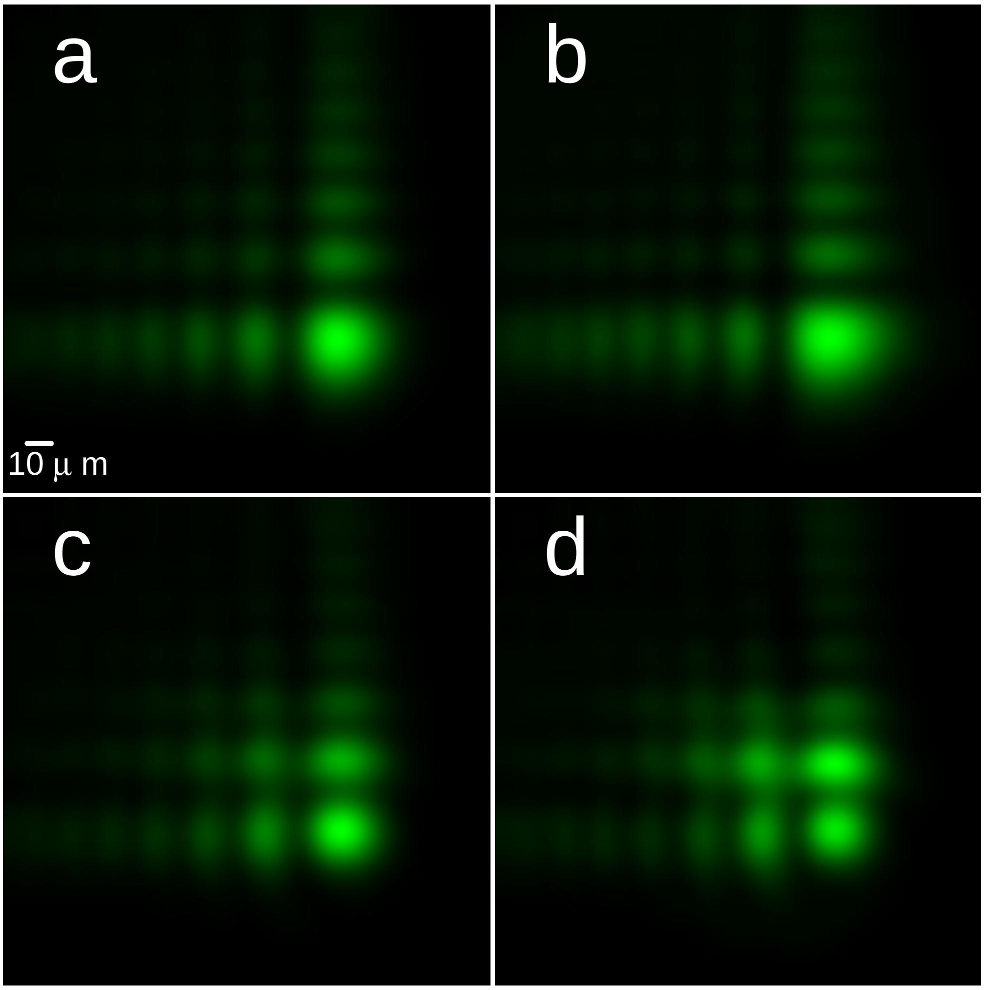

Figure 5.5: Numerical intensity distribution (anisotropic model) at back surface of the crystal a) 0V, b) 200V, c) 300V, d) 400V.

energy of lobes at the bottom is transferred towards the upper lobes with increase in the applied field. Numerical results from the anisotropic model are in good agreement with the experimental results. It is also noted that the beam radius, the input beam intensity and the applied field play a crucial role in the interaction of Airy beams. The interaction amongst the lobes slows down as we increase the input beam radius. For an increase in the applied field interaction becomes more prominent.

Conclusion

In conclusion, our experimental results show that the anisotropic model is a better model to explain Airy beams propagation in the PR media. It is not possible to observe 2D self-trapped self-accelerated beam in the PR media as the lobes of Airy beams start interacting with each other.

5.2 Bessel Beam

Bessel beams were first observed by Durnin et al [39]. These beams preserve their shape during propagation, therefore, these beams are called as diffraction-free. These beams also show self-healing or self-reconstruction property i. e. when some portion of these beams is blocked, they reconstruct after certain propagation [40]. These beams have applications in various fields which include nonlinear optics [42], and optical manipulation [43].

The Bessel beams are used to form light induced lattice inside the PR media [113–115]. These lattices support bright solitons [113], and discrete solitons [114]. The interaction of bright solitons and their planet like orbiting is observed in these lattices [113]. This orbiting of solitons depends on their initial phase difference. The experimental observation of self-focusing and localization of light in azimuthally modulated Bessel lattices have also been studied [115].

Since all the above mentioned studies were done in SBN with a focusing nonlinearity. In this work, we have made a numerical study of a Bessel beam propagating through a defocusing PR medium using parameters of $LiNbO_3$. We have found that the dark rings of Bessel beam break to form quadrupoles like LG beams [92].

Numerical Model

The complex field distribution of Bessel beams at $z = 0$ is written as (Eq. (1.28))

$$A(r, \phi, z) = \sqrt{I_m}\, J_n[r]\exp[in\phi]. \tag{5.10}$$

We have used the same numerical model as explained in section (4.1.2). We keep I_m=1 and w_0=16 μm in the numerical calculations.

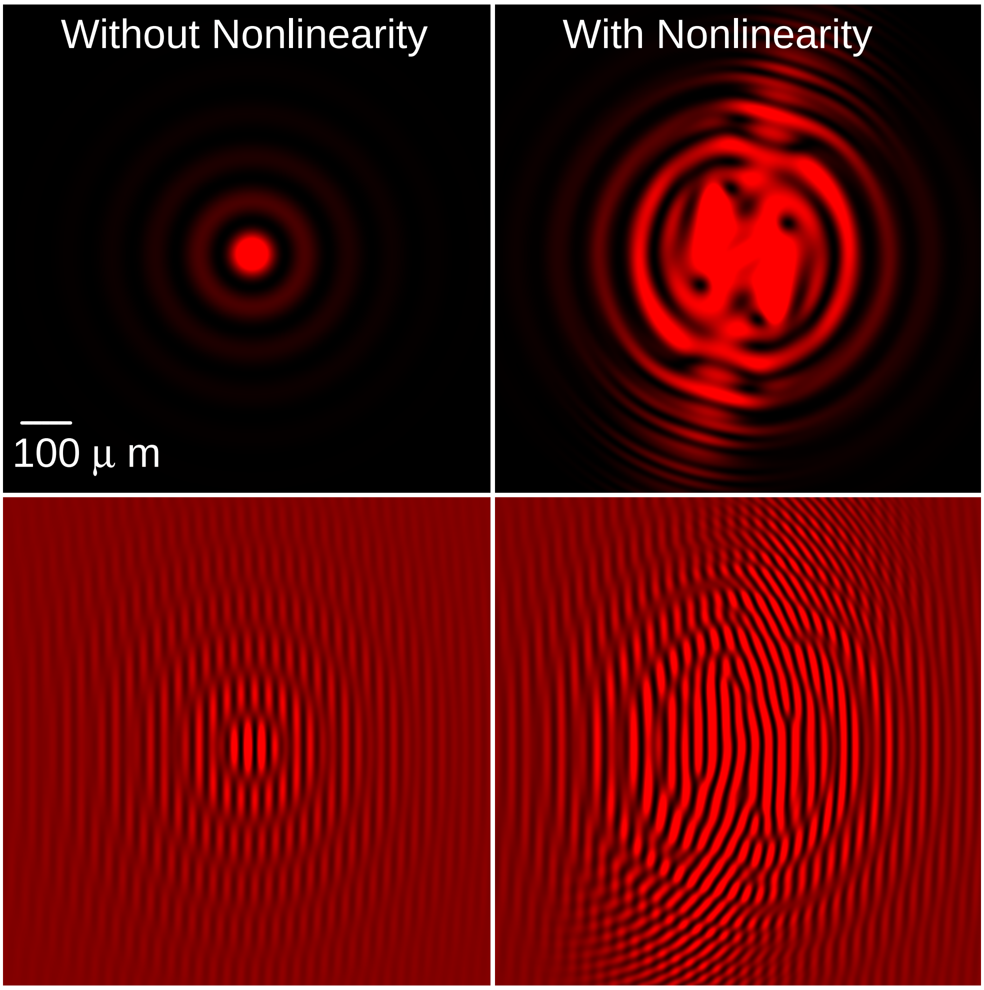

Figure 5.6: Numerical intensity profiles at back surface of the crystal for zeroth order Bessel beam (first row) and corresponding interferograms (second row).

Results and Discussion

Figure 5.6 shows numerical results for the propagation of a zeroth order Bessel beam through the PR crystal. In the absence of nonlinearity, there is no change in its profile. An interferogram shown in Fig. 5.6 confirms that there is a π phase jump at dark rings of this beam. As the beam propagates, space charge field develops with time which causes nonlinearity via electro-optic effect. In the presence of nonlinearity, at the steady state, the center lobe and the bright rings of the Bessel beam are defocused to form a quadrupole vortex like an LG beam with dark rings [92]. The presence of vortices are confirmed through the interferogram shown in Fig. 5.6

It is noted that all the dark rings of Bessel beam do not form quadrupole.

The reason is that the intensity of the beam decreases as one moves away from center which causes poor nonlinearity away from the center.

Conclusion

We conclude that the dark rings of Bessel beam behave similar to the dark rings of LG beam. In both the cases, the dark ring undergoes to instability to form a quadrupole in a defocusing PR medium.

Chapter 6

Summary and Scope for Future Work

This thesis deals with the propagation dynamics of different engineered beams in the PR media. These engineered beams are generated by using computer-generated holography technique. New methods for characterization of topological charge or OAM state of these beams have been proposed and verified experimentally. We have studied the effect of PR nonlinearity on the dynamics of these beams. The dipole and quadrupole vortices are found to be unstable in free space. The dipoles merge together and form crescent like structure as the beam propagates in free space. We have observed that these vortices become structurally stable in the defocusing PR medium. On the other hand, the dark ring beams generated from LG modes are found to be unstable while propagating through the defocusing PR media. They experience snake instability during propagation and form a quadrupole. These results show that dipole and quadrupole vortices are solutions of the nonlinear PWE with the PR nonlinearity. The rotational dynamics of ring lattice beams generated from the superposition of LG beams are examined in both the linear and the nonlinear media. It is found that for the beams having rotational velocity the edge dislocations change into screw dislocations. We have also studied the propagation dynamics of diffraction-free beams such as Airy beams and Bessel beams through the PR media. It is seen that the Airy beams' lobes interact with each other and exchange energy while propagating through the PR medium. We have compared our experimental results with numerical results obtained from isotropic as well as anisotropic model. A study of zeroth order Bessel beam propagating through the defocusing PR media shows that the dark ring convert to the quadrupole vortex. The results were similar to the LG beam with dark rings.

Chapter 1 gives elementary mathematical background for the work presented in the thesis. We have derived the PWE from Maxwell's equation for an inhomogeneous media. Since there are a number of nonlinear process which can create inhomogeneity in the medium, we have explained different nonlinearities with an emphasis on PR nonlinearity. The soliton solution of the nonlinear PWE with the PR nonlinearity has also been described. The various solutions of linear PWE which include Gaussian Beams, HG beams, LG beams, Bessel beams and Airy beams are discussed in this chapter.

In Chapter 2, we have discussed generation and characterization of engineered beams. The computer-generated holography technique have been employed for generation of these beams. The conventional holography have been introduced briefly with explanation of different types of holograms. The steps of computer-generated holography are presented in the same chapter. We have described our experimental technique for generation of the engineered beams in which a SLM is the key element. The working principle of the SLM has been highlighted with a description of various types of SLM. We have proposed new techniques for the measurement of OAM or topological charge of vortex. The analysis is done with a vortex embedded in a Gaussian beam i.e. pure vortex mode, however, these methods can be used for the LG and Bessel beams with phase singularities also. First method involves a QPM whereas a simple biconvex lens is used in the second method. It is observed that the propagation of optical vortex beams under quadratic phase depends on the topological charge of vortex beam. In the second method, the lens is tilted in such a way that it breaks the input optical vortex of topological charge l into $l + 1$ intensity spots. In both the methods, sign of charge can be found by looking at the alignment of break away intensity components.

Chapter 3 describes physics of PR nonlinearity. The basics of PR effect have been introduced. The band transport model of PR media is employed to derive the material equations. The isotropic and the anisotropic models are discussed for calculation of space charge field from material equations. The electro-optic effect which is responsible for the change in index of refraction in the PR media are also presented in the same chapter.

In Chapter 4, we have studied propagation dynamics of diffraction broadened beams through the photovoltaic PR media. All along the chapter, nonlinearity has been taken as the defocusing PR nonlinearity. To delineate the effect of nonlinearity, we have studied the propagation dynamics of vortex dipole and quadrupole in free space along with in the defocusing PR medium. It is found, both theoretically as well as experimentally, that dipole and quadrupole annihilate to form crescents while propagating in free space. Our results have shown that the annihilation of vortices is governed by the internal flow of energy associated with the individual vortex. In the PR media, we have observed the orientation dependent propagation of the dipole and the quadrupole. We have found that there is a stable dipole or quadrupole formation if the crescent formed without nonlinearity is perpendicular to the photovoltaic field of the nonlinear crystal. Our results have demonstrated that the dipole and the quadrupole are the solutions of the nonlinear PWE with the defocusing PR nonlinearity. We have also propagated HG beams through the PR medium with a view to study its dynamics. We have observed that when a dark stripe beam produced from the HG beam is perpendicular to the c-axis of the crystal, the radiated waves are formed over the bright lobes due to instability, however, they decay while propagating away from the center.

In the same chapter we have studied the propagation of dark rings produced from an LG beam, with and without topological charge, in a photovoltaic PR medium. We have observed the formation of quadrupoles in the PR medium. It is found that an edge dislocation of the dark ring converts into screw dislocations. We have also examined the propagation dynamics of ring lattice beams formed from the superposition of two LG beams. It is clear from our results that if ring lattice beam has rotational dynamics then only edge dislocations of that beam convert into screw dislocations. For ring lattice with zero rotation, the petals are defocused in the defocusing PR media, however, the edge dislocations between them remain as it is.

Chapter 5 is devoted to the study of nonlinear propagation of diffraction-free beams which include Airy and Bessel beams. We have observed that the Airy beams' lobes start interacting in the presence of an applied field while propagating through a PR medium with focusing nonlinearity. Therefore, it is not possible to observe 2D self-trapped self-accelerated beam in the PR media. It is also found that the anisotropic model is a better model to explain the Airy beams' propagation in the PR media. We have also examined the nonlinear propagation of dark rings of a Bessel beam in the PR media. They behave like the dark rings of LG beam in the defocusing PR media. In both cases, the dark ring undergoes to instability to form a quadrupole.

Scope for Future Work

In this thesis work, we have used $LiNbO_3$ crystal for our experiments which shows only defocusing nonlinearity. However, one can study propagation of engineered beams through the PR media with focusing nonlinearity also. We have done some numerical calculations for this nonlinearity using SBN crystals' parameter. In future, we would implement these numerical simulations experimentally.

First we would study the propagation of ring lattice beam through a focusing PR medium. We have planned to study self-trapping of these beams in the focusing PR media. For example, the optical azimuthons are self-trapped beams with azimuthal phase modulation, which have been observed recently in a saturable medium. We are expecting the observation of these beams in the PR medium. We will form azimuthons by propagating ring lattice beams having azimuthal phase variation through the PR crystal.

We have also planned to study the property of light induced ring lattices in a PR medium with the help of another probe beam. Our numerical results have shown that a bright soliton formed in bright ring lattice oscillates within the single petal throughout its journey. It is also observed that these oscillations depend on the position of petals of the ring lattice. One can also study propagation of an optical vortex as a probe beam through such ring lattices. Since these lattices have rotational dynamics, it will affect the dynamics of vortex beam.

Our next plan is to induce Airy beams' lattice in a PR medium and study its lattice property. We are expecting the self-trapped self-accelerated beam in this lattice. The work regarding the propagation of Airy beams in presence of defocusing nonlinearity is going on. Our numerical results show that the dark region of 1D Airy beam can be self-trapped by defocusing nonlinearity. We are trying to implement this numerical result experimentally.

Appendix A

Split-Step Fourier Transform Method

In this section, we have presented the Split-Step Fourier Transform method (SSFT) to study the propagation dynamics of engineered beams through the PR media. This method is observed to be fast compared to finite differnce method as it uses Fast Fourier Transform (FFT) algorithm [14, 15].

First we consider Eq. (1.17) that can be written in a normalized form as

$$\frac{\partial A(x,y)}{\partial z} = \frac{i}{2}\nabla^2 A(x,y) + i n_0 k_0^2 w_0^2 \Delta n A(x,y), \tag{A.1}$$

where Δn is the change in index of refraction, from Eq. (3.20),

$$\Delta n = -\frac{1}{2} n_0^3 r_{eff} E_{sc}. \tag{A.2}$$

Here, n_0 is the refractive index in the absence of light, k_0 is the wave number of light in free space, w_0 is the beam waist size, E_{sc} is the space charge field and r_{eff} is the effective electro-optic coefficient of the PR material. For all experiments mentioned in this thesis, we have chosen direction of polarization of an input beam along the c-axis of the crystal. Therefore, in our case, $r_{eff} = r_{33}$. The transverse coordinates x, y are scaled by w_0 and the propagation coordinate z is scaled by the diffraction length $k_0 n_0 w_0^2$.

Let us write Eq. (A.1) in the following form

$$\frac{\partial A}{\partial z} = [\hat{D} + \hat{N}]A, \tag{A.3}$$

where $\hat{D}$ and $\hat{N}$ are the differential and nonlinear operators respectively. $\hat{D}$ represents diffraction of a light beam in linear medium, however, effects of nonlinearity is governed by $\hat{N}$. These operators are written as,

$$\begin{aligned}\hat{D} &= \frac{i}{2}\nabla^2, \\ \hat{N} &= in_0 k_0^2 w_0^2 \Delta n.\end{aligned} \tag{A.4}$$

In general, a light beam experiences both diffraction and nonlinearity simultaneously while propagating through the PR medium. However, they act independently one after another in this method. The whole length of crystal is divided into small steps of distance dz. The propagation from z to $z + dz$ is written as

$$A(x, y, z + dz) = \exp[(\hat{D} + \hat{N})dz]A(x, y, z). \tag{A.5}$$

Now using Baker-Hausdorff formula for noncommuting operators $\hat{D}$ and $\hat{N}$, we get

$$\exp[(\hat{D} + \hat{N})dz] = \exp\left[(\hat{D} + \hat{N})dz + \frac{1}{2}[\hat{D}, \hat{N}]dz^2 + ...\right], \tag{A.6}$$

where $[\hat{D}, \hat{N}] = \hat{D}\hat{N} - \hat{N}\hat{D}$ denotes the commutation relation between $\hat{D}$ and $\hat{N}$. The SSFT ignores the noncommuting nature of these operators. With this assumption Eq. (A.5) can take the form

$$A(x, y, z + dz) = \exp[\hat{D}dz]\exp[\hat{N}dz]A(x, y, z). \tag{A.7}$$

The first operator represents the effect of nonlinearity in spatial domain. The second operator accounts for diffraction which carries out its operation in Fourier domain in the following way

$$\exp[\hat{D}dz]\exp[\hat{N}dz]A(x, y, z) = F^{-1}\{\exp[\frac{i}{2}(k_x^2 + k_y^2)dz]F\{\exp[\hat{N}dz]A(x, y, z)\}\}, \tag{A.8}$$

where k_x and k_y are the spatial frequencies in the Fourier domain. F denotes the Fourier transform operation which is performed using the FFT algorithm. The dominant error in the SSFT method comes from the commutator $[\hat{D}, \hat{N}]dz^2/2$ which is second order in step size dz . Hence, the accuracy of method can be increased by keeping dz small. Moreover, it can be improved further by considering nonlinear operator sandwiched between diffraction operator, which is written as

$$A(x,y,z+dz) = \exp[\hat{D}\frac{dz}{2}]\exp[\hat{N}dz]\exp[\hat{D}\frac{dz}{2}]A(x,y,z). \tag{A.9}$$

As exponential operators form a symmetry in this method, this is called as symmetrized SSFT. Here, the error is of third order in step size dz that can be verified from the Baker-Hausdorff formula.

Appendix B

Solving Potential Equation using Finite Difference Method

Consider the potential equation from Eq. (3.17)

$$\nabla^2\phi + \nabla\phi \cdot \nabla \ln(1+I) = (E_0 + E_p)\frac{\partial \ln(1+I)}{\partial y}. \qquad \text{(B.1)}$$

We have solved this equation using finite difference method. A finite difference method involves the following steps [116]:

1. Generation of computational grid.
2. Substitution of finite difference approximation in the place of derivatives in a partial differential equation (PDE) to form a linear system of algebraic equations.
3. Formulation of matrix to solve the system of algebraic equations.
4. Implementation of computer code.

First we generate a computational grid. Since dimension of our crystals are same along the x- and y- axis, the grid can be formed by dividing interval $[p, q]$ and $[r, s]$ into N equal step size h. We assume that,

$$\frac{q-p}{N} = \frac{s-r}{N} = h.$$

Let (x_j, y_k) be the point on the computational grid with $x_j = p + jh$ and $y_j = s + kh$ for $j = 0, 1, 2, ..., N$ and $k = 0, 1, 2, ..., N$.

Now we use the following notation,

$$u_{ij} = \phi(x, y), a_{ij} = \frac{\partial \ln(1+I)}{\partial x}, b_{ij} = \frac{\partial \ln(1+I)}{\partial y}, f_{ij} = (E_0 + E_p)\frac{\partial \ln(1+I)}{\partial x},$$

and substitute finite difference approximation in the place of derivatives in Eq. (B.1),

$$\frac{u_{j-1,k} - 2u_{j,k} + u_{j+1,k}}{h^2} + \frac{u_{j,k-1} - 2u_{j,k} + u_{j,k+1}}{h^2}$$
$$+a_{j,k}\frac{u_{j+1,k} - u_{j-1,k}}{2h} + b_{j,k}\frac{u_{j,k+1} - u_{j,k-1}}{2h} = f_{jk}. \tag{B.2}$$

We have assumed that the beam enters into a crystal almost at the center. Therefore, space charge potential is zero at the crystal boundary as there is no space charge present. This boundary condition implies that,

$$u_{0,0} = u_{j,0} = u_{0,k} = u_{N,N} = 0. \tag{B.3}$$

By applying boundary condition, we get

$$4u_{jk} - \left(1 - \frac{a_{jk}h}{2}\right)u_{j-1,k} - \left(1 + \frac{a_{jk}h}{2}\right)u_{j+1,k}$$
$$-\left(1 - \frac{b_{jk}h}{2}\right)u_{j,k-1} - \left(1 + \frac{b_{jk}h}{2}\right)u_{j,k+1} = -h^2 f_{jk}. \tag{B.4}$$

Above equation is linear with the unknowns, hence, it can be written in matrix form. Let us consider number of intervals as $N = 4$ for simplification. The matrix form of Eq. (B.4) is written as

$$Au = B, \tag{B.5}$$

where u, B and A have following form,

$$u = \begin{bmatrix} u_{11} \\ u_{21} \\ u_{31} \\ u_{12} \\ u_{22} \\ u_{32} \\ u_{13} \\ u_{23} \end{bmatrix}, B = \begin{bmatrix} -h^2 f_{11} \\ -h^2 f_{21} \\ -h^2 f_{31} \\ -h^2 f_{12} \\ -h^2 f_{22} \\ -h^2 f_{32} \\ -h^2 f_{13} \\ -h^2 f_{23} \\ -h^2 f_{33} \end{bmatrix},$$

Since this matrix equation can be generalized for any N, by solving this matrix equation numerically, one can find out the value of u i.e space charge potential ϕ.

A=

$$
\begin{bmatrix}
4 & -\left(1+\frac{a_{11}h}{2}\right) & 0 & | & -\left(1+\frac{b_{11}h}{2}\right) & 0 & 0 & | & 0 & 0 & 0 \\
-\left(1-\frac{a_{21}h}{2}\right) & 4 & -\left(1+\frac{a_{21}h}{2}\right) & | & 0 & -\left(1+\frac{b_{21}h}{2}\right) & 0 & | & 0 & 0 & 0 \\
0 & -\left(1-\frac{a_{31}h}{2}\right) & 4 & | & 0 & 0 & -\left(1+\frac{b_{31}h}{2}\right) & | & 0 & 0 & 0 \\
--- & --- & --- & --- & --- & ---- & --- & --- & --- & --- & --- \\
-\left(1-\frac{b_{12}h}{2}\right) & 0 & 0 & | & 4 & -\left(1+\frac{a_{12}h}{2}\right) & 0 & | & -\left(1+\frac{b_{12}h}{2}\right) & 0 & 0 \\
0 & -\left(1-\frac{b_{22}h}{2}\right) & 0 & | & -\left(1-\frac{a_{22}h}{2}\right) & 4 & -\left(1+\frac{a_{22}h}{2}\right) & | & 0 & -\left(1+\frac{b_{22}h}{2}\right) & 0 \\
0 & 0 & -\left(1-\frac{b_{32}h}{2}\right) & | & 0 & -\left(1-\frac{a_{32}h}{2}\right) & 4 & | & 0 & 0 & -\left(1+\frac{b_{33}h}{2}\right) \\
--- & --- & --- & --- & --- & --- & --- & --- & --- & --- & --- \\
0 & 0 & 0 & | & -\left(1-\frac{b_{13}h}{2}\right) & 0 & 0 & | & 4 & -\left(1+\frac{a_{13}h}{2}\right) & 0 \\
0 & 0 & 0 & | & 0 & -\left(1-\frac{b_{23}h}{2}\right) & 0 & | & -\left(1-\frac{a_{23}h}{2}\right) & 4 & -\left(1+\frac{a_{23}h}{2}\right) \\
0 & 0 & 0 & | & 0 & 0 & -\left(1-\frac{b_{33}h}{2}\right) & | & 0 & -\left(1-\frac{a_{33}h}{2}\right) & 4
\end{bmatrix}
$$

Bibliography

[1] A. Siegman, *Lasers* (University Science Books, Sausalito, 1986).

[2] N. Hodgson and H. Weber, *Optical Resonator* (Springer, London, 1997).

[3] A. Ghatak and K. Thyagarajan, *Optical Electronics* (Cambridge University Press, Cambridge, 2008).

[4] G. A. Siviloglou, J. Broky, A. Dogariu, and D. N. Christodoulides, "Observation of accelerating Airy beams," Phys. Rev. Lett. **99**, 213901 (2007).

[5] D. McGloin and K. Dholakia, "Bessel beams: diffraction in a new light," Contem. Phys. **46,** 15 (2005).

[6] B. Saleh and M. Teich, *Fundamentals of Photonics* (John Wiley and Sons, New York, 1991).

[7] P. Yeh, *Introduction to Photorefractive Nonlinear Optics* (John Wiley and Sons, New York, 1993).

[8] W. Q. Chen, X. Yang, S. Y. Zhong, Z. Yan, T. H. Zhang, J. G. Tian, and J. J. Xu, "Surface dark screening solitons," Opt. Lett. **36,** 3801 (2011).

[9] D. M. Jović, C. Denz, and M. R. Belić, "Vortex solitons at the boundaries of photonic lattices," Opt. Express, **19,** 26232 (2011).

[10] B. Terhalle, A. Desyatnikov, D. N. Neshev, W. Krolikowski, C. Denz, and Y. S. Kivshar, "Dynamic diffraction and interband transitions in two-dimensional photonic lattices," Phys. Rev. Lett. **106,** 083902 (2011).

[11] D. M. Jović, Y. S. Kivshar, C. Denz, and M. R. Belić, "Anderson localization of light near boundaries of disordered photonic lattices," Phys. Rev. A **83,** 033813 (2011).

[12] J. Xavier and J. Joseph, "Tunable complex photonic chiral lattices by reconfigurable optical phase engineering," Opt. Lett., **36,** 403 (2011).

[13] J. Xavier, S. Vyas, P. Senthilkumaran, C. Denz, and J. Joseph, "Sculptured 3D twister superlattices embedded with tunable vortex spirals," Opt. Lett. **36,** 3512 (2011).

[14] G. P. Agrawal, *Nonlinear Fiber Optics* (Academic Press, San Diego, 2003).

[15] T. C. Poon and T. Kim, *Engineering Optics with Matlab* (World Scientific, New Jersey, 2006).

[16] K. Kawano and T. Kitoh, *Optical waveguide analysis* (John Willey and Sons. Inc, New York, 2001).

[17] R. W. Boyd, *Nonlinear Optics* (Academic Press, San Diego, 2003).

[18] Y. S. Kivshar and G. P. Agrawal, *Optical Solitons* (Academic Press, San Diego, 2003).

[19] R. H. Stolen and Chinlon Lin, "Self-phase-modulation in silica optical fibers," Phys. Rev. A **17,** 1448 (1978).

[20] D. E. Spence, P. N. Kean, and W. Sibbett, "60-fsec pulse generation from a self-mode-locked Ti:sapphire laser," Opt. Lett. **16,** 42 (1991).

[21] C. Rotschild, B. Alfassi, O. Cohen, and M. Segev, "Long-range interactions between optical solitons," Nat. Phys. **2,** 769 (2006).

[22] "Special issue: Solitons," Opt. Phot. News. February, Vol.**13,** (2002).

[23] M. Segev, G. C. Valley, B. Crosignani, P. DiPorto, and A. Yariv, "Steady-state spatial screening solitons in photorefractive materials with external applied field," Phys. Rev. Lett. **73,** 3211 (1994).

[24] M. Taya, M. C. Bashaw, M. M. Fejer, M. Segev, and G. C. Valley, "Observation of dark photovoltaic spatial solitons," Phys. Rev. A **52,** 3095 (1995).

[25] M. Segev, G. C. Valley, M. C. Bashaw, M. Taya and M. M. Fejer, "Photovoltaic spatial solitons," J. Opt. Soc. Am. B **14,** 1772 (1997).

[26] W. L. She, K. K. Lee, and W. K. Lee, "Observation of Two-Dimensional Bright Photovoltaic Spatial Solitons," Phys. Rev. Lett. **83,** 3182 (1999).

[27] Z. Chen, M. Mitchell, and M. Segev, "Steady-state photorefractive soliton-induced Y-junction waveguides and high-order dark spatial solitons," Opt. Lett. **21,** 716 (1996).

[28] M. Shih, Z. Chen, M. Mitchell, M. Segev, H. Lee, R. S. Feigelson, and J. P. Wilde, "Waveguides induced by photorefractive screening solitons," J. Opt. Soc. Am. B **14,** 3091 (1997).

[29] S. Lan, E. DelRe, Z. Chen, M. Shih, and M. Segev, "Directional coupler with soliton-induced waveguides," Opt. Lett. **2,** 475 (1999).

[30] M.D Iturbe Castillo, J.J Snchez-Mondragn, S.I Stepanov, M.B Klein, and B.A Wechsler, "(1 + 1)-Dimension dark spatial solitons in photorefractive $Bi_{12}TiO_{20}$ crystal," Opt. Commun. **118,** 515 (1995).

[31] Y. S. Kivshar and B. Luther-Davies, "Dark optical solitons: physics and applications," Phys. Reports **298,** 81 (1998).

[32] M. Soskin and M. Vasnetsov, "Singular optics," in Progress in Optics, Wolf, E., ed. (Elsevier Science EV, 2001), pp. 219-276.

[33] L. Allen, M. J. Padgett, and M. Babiker, “The orbital angular momentum of light,” in Progress in Optics, Wolf, E., ed. (Elsevier Science EV, 1999), pp. 291-372.

[34] H. He, M. E. J. Friese, N. R. Heckenberg, and H. Rubinsztein-Dunlop, “Direct observation of transfer of angular momentum to absorptive particles from a laser beam with a phase singularity,” Phys. Rev. Lett. **75,** 826 (1995).

[35] G. Gibson, J. Courtial, M. Padgett, M. Vasnetsov, V. Pas’ko, S. Barnett, and S. Franke-Arnold, “Free-space information transfer using beams carrying orbital angular momentum,” Opt. Express **12,** 5448 (2004).

[36] G. Molina-Terriza, J. Torres, and L. Torner, “Twisted photons,” Nat. Phys. **3,** 305 (2007).

[37] M. Soskin, V. Gorshkov, M. Vasnetsov, J. Malos, and N. Heckenberg, “Topological charge and angular momentum of light beams carrying optical vortices,” Phys. Rev. A **56,** 4064 (1997).

[38] M. Beijersbergen, L. Allen, H.E.L.O. van der Veen and J.P. Woerdman, “Astigmatic laser mode converters and transfer of orbital angular momentum,” Opt. Commun. **96,** 123 (1993).

[39] J. Durnin, J. J. Miceli, and J. H. Eberly, “Diffraction-free beams,” Phys. Rev. Lett. **58,** 1499 (1987).

[40] Z. Bouchal, J. Wagner, and M. Chlup, “Self-reconstruction of a distorted nondiffracting beam,” Opt. Commun. **151,** 207 (1998).

[41] N. Chattrapiban, E. A. Rogers, D. Cofield, and R. Roy, “Generation of nondiffracting Bessel beams by use of a spatial light modulator,” Opt. Lett. **28,** 2183 (2003).

[42] T. Wulle and S. Herminghaus, “Nonlinear optics of Bessel beams,” Phys. Rev. Lett. **70,** 1401 (1993).

[43] J. Arlt, V. Garces-Chavez, W. Sibbett, and K. Dholakia, "Optical micromanipulation using a Bessel light beam," Opt. Commun. **197,** 239 (2001).

[44] M. V. Berry and N. L. Balazs, "Non-spreading wave packet," Am. J. Phys. **47,** 264 (1979).

[45] G. A. Siviloglou, J. Broky, A. Dogariu, and D. N. Christodoulides, "Ballistics dynamics of Airy beams," Opt. Lett. **33,** 207 (2008).

[46] Y. Hu, P. Zhang, C. Lou, S. Huang, J. Xu, and Z. Chen, "Optimal control of the ballistic motion of Airy beams," Opt. Lett. **13,** 2260 (2010).

[47] J. Broky, G. A. Siviloglou, A. Dogariu, and D. N. Christodoulides, "Self-healing properties of optical Airy beams," Opt. Express **16,** 12880 (2008).

[48] J. Baumgartl, M. Mazilu, and K. Dholakia, "Optically mediated particle clearing using Airy Wavepackets," Nat. Photon. **2,** 675 (2008).

[49] P. Polynkin, M. Kolesik, J. V. Moloney, G. A. Siviloglou, and D. N. Christodoulides, "Curved Plasma Channel Generation using ultra intense Airy beams," Science **324,** 229 (2009).

[50] J. Goodman, *Introduction to Fourier Optics* (Roberts and Company, Greenwood Village, 2004).

[51] L. Janicijevic and S. Topuzoski, "Fresnel and Fraunhofer diffraction of a Gaussian laser beam by fork-shaped gratings," J. Opt. Soc. Am. A **25,** 2659 (2008).

[52] J. Hickmann, E. Fonseca, W. Soares, and S. Chvez-Cerda, "Unveiling a truncated optical lattice associated with a triangular aperture using light's orbital angular momentum," Phys. Rev. Lett. **105,** 053904 (2010).

[53] A. Mourka, J. Baumgartl, C. Shanor, K. Dholakia, and E. Wright, "Visualization of the birth of an optical vortex using diffraction from a triangular aperture," Opt. Express **19,** 5760 (2011).

[54] L. de Araujo and Ma. Anderson, "Measuring vortex charge with a triangular aperture," Opt. Lett. **36,** 787 (2011).

[55] Y. Han and G. Zhao, "Measuring the topological charge of optical vortices with an axicon," Opt. Lett. **36,** 2017 (2011).

[56] C. Guo, L. Lu, and H. Wang, "Characterizing topological charge of optical vortices by using an annular aperture," Opt. Lett. **34,** 3686 (2009).

[57] G. Berkhout and M. Beijersbergen, "Method for probing the orbital angular momentum of optical vortices in electromagnetic waves from astronomical objects," Phys. Rev. Lett. **101,** 100801 (2008).

[58] G. Berkhout, M. Lavery, J. Courtial, M. Beijersbergen, and M. Padgett, "Efficient sorting of orbital angular momentum states of light," Phys. Rev. Lett. **105,** 153601 (2010).

[59] G. Berkhout, M. Lavery, M. Padgett, and M. Beijersbergen, "Measuring orbital angular momentum superpositions of light by mode transformation," Opt. Lett. **36,** 1863 (2011).

[60] S. Prabhakar, A. Kumar, J. Banerji, and R. P. Singh, "Revealing the order of a vortex through its intensity record," Opt. Lett. **36,** 4398 (2011).

[61] A. Kumar, S. Prabhakar, P. Vaity, and R. P. Singh, "Information content of optical vortex fields," Opt. Lett. **36,** 1161 (2011).

[62] P. Vaity and R. P. Singh, "Topological charge dependent propagation of optical vortices under quadratic phase transformation," Opt. Lett. **36,** 1301 (2011).

[63] I. S. Gradshteyn and I. M. Ryzhik, *Table of Integral, Series, and Products* (Acdemic Press, San diego, 2001) pp. 923.

[64] I. S. Gradshteyn and I. M. Ryzhik, *Table of Integral, Series, and Products* (Acdemic Press, San diego, 2001) pp. 361.

[65] P. M. Blanchard and A. H. Greenaway, “Simultaneous multiplane imaging with a distorted diffraction grating,” Appl. Opt. **38,** 6692 (1999).

[66] A. Bekshaev, M. Soskin, and M. Vasnetsov, “Transformation of higher-order optical vortices upon focusing by an astigmatic lens,” Opt. Commun. **241,** 237 (2004).

[67] V. Denisenko, V. Shvedov, A. S. Desyatnikov, D. N. Neshev, W. Krolikowski, A. Volyar, M. Soskin, and Y. S. Kivshar, “Determination of topological charges of polychromatic optical vortices,” Opt. Express **17,** 23374 (2009).

[68] R. Singh, P. Senthilkumaran, and Kehar Singh, “Influence of astigmatism and defocusing on the focusing of a singular beam,” Opt. Commun. **270,** 128 (2007).

[69] B. Goss Levi, “New compound brightens outlook for photorefractive polymers,” Phys. Today **48(1),** 17 (1995).

[70] W. Horn, J. V. Bassewitz, and C. Denz, “Slow and fast light in photorefractive SBN:60,” J. Opt. **12,** 104011 (2010).

[71] N. Kukhtarev, V. Markov, S. Odulov, M. Soskin, and V. Vinetskii, “Holographic storage in electro-optic crystals. I. Steady state,” Ferroelectrics **22,** 949 (1979).

[72] D. N. Christodoulides and M. I. Carvalho, “Bright, dark, and gray spatial soliton states in photorefractive media,” J. Opt. Soc. Am. B **12,** 1628 (1995).

[73] A. A. Zozulya and D. Z. Anderson, “Propagation of an optical beam in a photorefractive medium in the presence of a photogalvanic nonlinearity or an externally applied electric field,” Phys. Rev. A **51,** 1520 (1995).

[74] M. R. Belic, D. Vujic, A. Stepken, and F. Kaiser, "Isotropic versus anisotropic modeling of photorefractive solitons," Phys. Rev. E **65,** 066610 (2002).

[75] A. Stepken, F. Kaiser, and M. R. Belic, "Anisotropic interaction of three-dimensional spatial screening solitons," J. Opt. Soc. Am. B **17,** 68 (2000).

[76] A. Yariv and P. Yeh, *Photonics* (Oxford University Press, New York, 2007).

[77] A. V. Mamaev, M. Saffman, and A. A. Zozulya, "Decay of high order optical vortices in anisotropic nonlinear optical media," Phys. Rev. Lett. **78,** 2108 (1997).

[78] X. Gan, P. Zhang, S. Liu, Y. Zheng, J. Zhao, and Z. Chen, "Stabilization and breakup of optical vortices in presence of hybrid nonlinearity," Opt. Express **17,** 23130 (2009).

[79] A. V. Mamaev, M. Saffman, and A. A. Zozulya, "Time-dependent evolution of an optical vortex in photorefractive media," Phys. Rev. A **56,** R1713 (1997).

[80] R. Passier, F. Devaux, and M. Chauvet, "Impact of tensorial nature of the electro-optic effect on vortex beam propagation in photorefractive media," Opt. Express **16,** 7134 (2008).

[81] G. Indebetouw, "Optical vortices and their propagation," J. Mod. Opt. **40,** 73 (1993).

[82] F. S. Roux, "Dynamical behavior of optical vortices," J. Opt. Soc. Am. B **12,** 1215 (1995).

[83] D. Rozas, C. T. Law, and G. A. Swartzlander, "Propagation dynamics of optical vortices," J. Opt. Soc. Am. B **14,** 3054 (1997).

[84] G. H. Kim, H. J. Lee, J. U. Kim, and H. Suk, “Propagation dynamics of optical vortices with anisotropic phase profiles,” J. Opt. Soc. Am. B **20,** 351 (2003).

[85] F. S. Roux, “Canonical vortex dipole dynamics,” J. Opt. Soc. Am. B **21,** 655 (2004).

[86] M. Chen and F. S. Roux, “Accelerating the annihilation of an optical vortex dipole in a Gaussian beam,” J. Opt. Soc. Am. B **25,** 1279 (2008).

[87] A. V. Mamaev, M. Saffman, and A. A. Zozulya, “Vortex evolution and bound pair formation in anisotropic nonlinear optical media,” Phys. Rev. Lett. **77,** 4544 (1996).

[88] A. V. Volyar and T. A. Fadeeva, “Generation of singular beams in uniaxial crystals,” Opt. Spectrosc. **94,** 235 (2003).

[89] A. Volyar, V. Shvedov, T. Fadeyeva, A. S. Desyatnikov, D. N. Neshev, W. Krolikowski, and Y. S. Kivshar, “Generation of single-charge optical vortices with an uniaxial crystal,” Opt. Express **4,** 3724 (2006).

[90] A. V. Mamaev and M. Saffman, “Propagation of dark stripe beams in nonlinear media: snake instability and creation of optical vortices,” Phys. Rev. Lett. **76,** 2262 (1996).

[91] A. V. Mamaev, M. Saffman, D. Z. Anderson, and A. A. Zozulya, “Propagation of light beams in anisotropic nonlinear media: from symmetry breaking to spatial turbulence,” Phys. Rev. A **54,** 870 (1996).

[92] P. Vaity and R. P. Singh, “Generation of quadrupoles through instability of dark rings in photorefractive media,” J. Opt. Soc. Am. B (to be published).

[93] Y. Kivshar and X. Yang, “Ring dark solitons,” Phys. Rev. E **50,** R40 (1994).

[94] S. Baluschev, A. Dreischuh, I. Velchev, S. Dinev, and O. Marazov, "Generation and evolution of two-dimensional dark spatial solitons," Phys. Rev. E **52,** 5517 (1995).

[95] D. Neshev, A. Dreischuh, V. Kamenov, I. Stefanov, S. Dinev, W. Flieber, and L. Windholz, "Generation and intrinsic dynamics of ring dark solitary waves," Appl. Phys. B **64,** 429 (1997).

[96] G. Theocharis, D. J. Frantzeskakis, P.G. Kevrekidis, B. A. Malomed, and Y. S. Kivshar, "Ring dark solitons and vortex necklaces in Bose-Einstein condensates," Phys. Rev. Lett. **52,** 2262 (2003).

[97] A.M. Kamchatnov and S.V. Korneev, "Dynamics of ring dark solitons in Bose-Einstein condensates and nonlinear optics," Phys. Lett. A **374,** 4625 (2010).

[98] Z. Chen, M. Segev, D. W. Wilson, R. E. Muller, and P. D. Maker, "Self-Trapping of an Optical Vortex by Use of the Bulk Photovoltaic Effect," Phys. Rev. Lett. **78,** 2948 (1997).

[99] M. R. Dennis, "Rows of optical vortices from elliptically perturbing a high-order beam," Opt. Lett. **31,** 1325 (2006).

[100] A. Kumar, P. Vaity, and R. P. Singh, "Crafting the core asymmetry to lift the degeneracy of optical vortices," Opt. Express **19,** 6182 (2011).

[101] E.Galvez, N. Smiley, and N. Fernandes, "Composite Optical Vortices Formed by Collinear Laguerre-Gauss Beams," in Proc. SPIE **6131,** 19 (2006).

[102] S. Franke-Arnold, J. Leach, M. Padgett, V. Lembessis, D. Ellinas, A. Wright, J. Girkin, P. Ohberg, and A. Arnold, "Optical ferris wheel for ultracold atoms," Opt. Express **15,** 8619 (2007).

[103] A.Bekshaev, M. Soskin, and Vasnetsov, "Centrifugal transformation of the transverse structure of freely propagating paraxial light beams," Opt. Lett. **31,** 694 (2006).

[104] A.Bekshaev and M. Soskin, "Rotational transformations and transverse energy flow in paraxial light beams: linear azimuthons," Opt. Lett. **31,** 2199 (2006).

[105] S. Baumann, D. Kalb, L. MacMillan and E. Galvez, "Propagation dynamics of optical vortices due to Gouy phase," Opt. Express **17,** 9818 (2009).

[106] P. Vaity and R. P. Singh, " Self-healing property of optical ring lattice," Opt. Lett. **36,** 2994 (2011).

[107] D. Deng and Q. Guo, "Dynamics of collinear LaguerreGaussian beams in nonlocal nonlinear media," Appl. Phys. B **100,** 897 (2010).

[108] Y. J. He, B. A. Malomed, D. Mihalache, H. Hulubei, and H. Z. Wang, "Spinning bearing-shaped solitons in strongly nonlocal nonlinear media," Phys. Lett. A **77,** 043826 (2008).

[109] V. M. Lashkin, A. S. Desyatnikov, E. A. Ostrovskaya, and Y. S. Kivshar, "Azimuthal vortex clusters in Bose-Einstein condensates," Phys. Rev. A **85,** 013620 (2012).

[110] I. Kaminer, M. Segev, and D. N. Christodoulides, "Self-Accelerating Self-Trapped Optical Beams," Phys. Rev. Lett. **106,** 213903 (2011).

[111] S. Jia, J. Lee, and J. W. Fleischer, "Diffusion-Trapped Airy Beams in Photorefractive Media," Phys. Rev. Lett. **104,** 253904 (2010).

[112] Y. Hu, S. Huang, P. Zhang, C. Lou, J. Xu, and Z. Chen, "Persistence and breakdown of Airy beams driven by an initial nonlinearity," Opt. Lett. **35,** 3952 (2010).

[113] S. Huang, P. Zhang, X. Wang, and Z. Chen, "Observation of soliton interaction and planetlike orbiting in Bessel-like photonic lattices," Opt. Lett. **35,** 2284 (2010).

[114] X. Wang, Z. Chen, and P. G. Kevrekidis, "Observation of Discrete Solitons and Soliton Rotation in Optically Induced Periodic Ring Lattices," Phys. Rev. Lett. **96,** 083904 (2006).

[115] R. Fischer, D. N. Neshev, S. Lopez-Aguayo, A. S. Desyatnikov, A. A. Sukhorukov, W. Krolikowski, and Y. S. Kivshar, "Observation of light localization in modulated Bessel optical lattices," Opt. Express **14,** 2825 (2006).

[116] B. Bradie, *A Friendly Introduction to Numerical Analysis* (Pearson Education, Delhi, 2003).

Publications attached with the thesis

1. **Pravin Vaity** and R. P. Singh, *Topological charge dependent propagation of optical vortices under quadratic phase transformation*, Opt. Lett. 37 1301-1303 (2012).

2. **Pravin Vaity** and R. P. Singh, *Generation of quadrupoles through instability of dark rings in photorefractive media*, J. Opt. Soc. Am. B (to be published).